2012

Regression Function Characterization of Synchronous Machine Magnetization and Its Impact on Machine Stability Analysis

Saeedeh Hamidifar
University of Windsor

Regression Function Characterization of Synchronous Machine Magnetization and Its Impact on Machine Stability Analysis

by

Saeedeh Hamidifar

A Dissertation
Submitted to the Faculty of Graduate Studies through
the Department of Electrical and Computer Engineering
in Partial Fulfillment of the Requirements for the
Degree of Doctor of Philosophy at the
University of Windsor

Windsor, Ontario, Canada

2012

Regression Function Characterization of Synchronous Machine Magnetization and Its
Impact on Machine Stability Analysis

by

Saeedeh Hamidifar

APPROVED BY:

_____
Tomy Sebastian, External Examiner
Nexteer Automotive

_____
Arunita Jaekel
Department of Computer Science, University of Windsor

_____
Jonathan Wu
Department of Electrical and Computer Engineering, University of Windsor

_____
Govinda Raju
Department of Electrical and Computer Engineering, University of Windsor

_____
Narayan C. Kar
Department of Electrical and Computer Engineering, University of Windsor

_____
Chair of Defense

June 2012

Declaration of Previous Publication

This thesis includes four original papers that have been previously published/ submitted for publication in peer reviewed journals/conferences, as follows:

Thesis Chapter	Publication Title	Publication Type	Publication Status
Chapters 3,6	A novel approach to saturation characteristics modeling and its impact on synchronous machine transient stability analysis	Transaction	Published
Chapter 3	A trigonometric technique for characterizing magnetic saturation in electrical machines	Conference	Published
Chapter 4	A novel method to represent the saturation characteristics of PMSM using Levenberg-Marquardt algorithm	Conference	Published
Chapters 4,5	A state space synchronous machine model with multifunctional characterization of saturation using levenberg-marquardt optimization algorithm	Transaction	Submitted/Under Revision

I certify that I have obtained a written permission from the copyright owner(s) to include the above published materials in my thesis and have included copies of such copyright clearances to my appendix. I certify that the above materials describe work completed during my registration as graduate student at the University of Windsor. I declare that, to the best of my knowledge, my thesis does not infringe upon anyone's copyright

nor violate any proprietary rights and that any ideas, techniques, quotations, or any other material from the work of other people included in my thesis, published or otherwise, are fully acknowledged in accordance with the standard referencing practices. Furthermore, to the extent that I have included copyrighted material that surpasses the bounds of fair dealing within the meaning of the Canada Copyright Act, I certify that I have obtained a written permission from the copyright owner to include such materials in my thesis.

Abstract

Magnetization in the ferromagnetic core significantly affects the performance of electrical machines. In the performance analysis of electrical machines, an accurate representation of the magnetization characteristics in the machine model is important. As a part of this research work, two new mathematical models are proposed to represent the magnetization characteristics of electrical machines based on the measured magnetization characteristics data points. These models can be applied to various kinds and sizes of electrical machines. The calculated results demonstrate the effectiveness of the proposed models. The comparison analyses on the proposed models and three different existing models which have been used in the literature by the researchers validate the fact that these models can be used as proper alternative for the other models.

Inasmuch as the omission of magnetization in the machine model has a negative impact on the analysis results, integrating the proposed magnetization models into the synchronous machine mode, can better describe the machine behavior. To aim this goal, as a part of this research, the proposed magnetization models are incorporated to the transient

and steady state synchronous machine models. The trigonometric model developed in this work, has been applied to a conventional synchronous machine model and extensive stability performance analysis has been carried out. This further reveals the usefulness of the proposed trigonometric magnetization model and the importance of the inclusion of magnetization in stability analysis. The other magnetization model developed in this research is incorporated into a state space synchronous machine model that is used in steady state performance analysis of the machine.

With Love and Gratitude

To My Lovely Mother and Father

For Blessing Every Moment of My Life with Their Unconditional Support and Love

and

For Their Tremendous Patience, Trust, and Faith in Me

Acknowledgements

I would like to express my sincere gratitude to my supervisor, Dr. Narayan Kar; For his invaluable support, inspiring guidance, and encouragements throughout the course of this thesis work. I would like to thank him for believing in me and my work and giving me the opportunity to work as a member of his research team.

I would like to express my gratitude to my committee members, Dr. Arunita Jaekel, Dr. Govinda Raju, Dr. Jonathan Wu, and Dr. Tomy Sebastian from Nexteer Automotive for reviewing my thesis and their constructive comments and valuable suggestions to improve this work.

I would also like to thank Ms. Andria Ballo, the Graduate Secretary of Electrical and Computer Engineering Department at the University of Windsor, for her smiles and love; and for making my life very easy with her supports during the busiest time of my life.

I am thankful to all my friends and colleagues in the Centre for Hybrid Automotive Research & Green Energy (CHARGE) for their encouragements and supports. Working in their friendly company was a wonderful experience.

Deep from my heart, I am grateful to my mother, my father, and my siblings for their tender love, gentle guidance, and sacrifice. They are my greatest blessing in life.

Table of Contents

List of Tables

List of Figures

Nomenclatures

l_{aa}, l_{bb}, l_{cc},	: Self-inductance of stator windings
l_{ab}, l_{bc}, l_{ca},	: Mutual-inductance between stator windings
l_{afd}, l_{akd}, l_{akq},	: Mutual-inductance between stator and rotor windings
L_{ffd}, l_{kkd}, l_{kkq},	: Self-inductance of rotor windings
Ψ	: Flux linkage
I_m	: Magnetizing current
b_j, α_j, β_j	: DFT and trigonometric series amplitudes
ω_j, υ_i	: DFT and trigonometric series frequencies
k, k'	: DFT and trigonometric orders
a_j	: LM function coefficients
ε	: Error criterion
χ^2	: Chi-square error
σ^2	: Variance
λ	: Damping factor in LM algorithm
V_t	: Steady state terminal voltage
e_d, e_q	: d- and q-axis components of the stator voltage
X_{md}, X_{mq},	: d- and q-axis magnetizing reactances
I_d, I_q	: d- and q-axis components of the stator current

γ : Saturation coefficient matrix

Ψ_d, Ψ_q : d- and q-axis components of the flux linkage

$\Psi_{fd}, \Psi_{kd}, \Psi_{kq}$: Field and d- and q-axis damper winding flux linkages

I_{fd}, I_{kd}, I_{kq} : Field and d- and q-axis damper winding currents

R_{fd}, R_{kd}, R_{kq} : Field and d- and q-axis damper winding resistances

X_{fd}, X_{kd}, X_{kq} : Field and d- and q-axis damper winding reactances

R_a : Stator resistance

X_l : Stator leakage reactance

ω_B, ω_r : Rated and rotor speeds in electrical radian/second

δ : Load angle

K_D : Damping torque coefficient

H : Inertia constant

T_m : Mechanical torque input

τ_e, τ_L : Air-gap and load torques

H : Inertia constant

e_{fd} : Field voltage referred to the stator

V_{t0}, V_{t1} : Voltage during and after the fault

$\delta_{p\text{-}p}$: Peak-to-peak load angle

$\tau_{p\text{-}p}$: Peak-to-peak air-gap torque

$S_\aleph$: Sensitivity with respect to $\aleph$

N : The number of samples

T : Sampling intervals

W : Window function in STFT

P_m : Mechanical input power

P_e : Electrical input power

Chapter 1

Introduction

1.1. Research Background

1.1.1.   Magnetization Modeling

Analysis of the non-linear saturation properties of ferromagnetic materials in electrical machines necessitates mathematical representation of the flux linkage-current relationship [1]- [5]. Various mathematical models have been presented by many researchers that describe the flux linkage and current relationship in electrical machines. The inclusion of magnetization in the electrical machine analysis is important since it affects the magnetic flux in the direct and quadrature axes. The leakage flux paths are also influenced by the magnetization effect. To ensure an accurate and reliable model for electrical
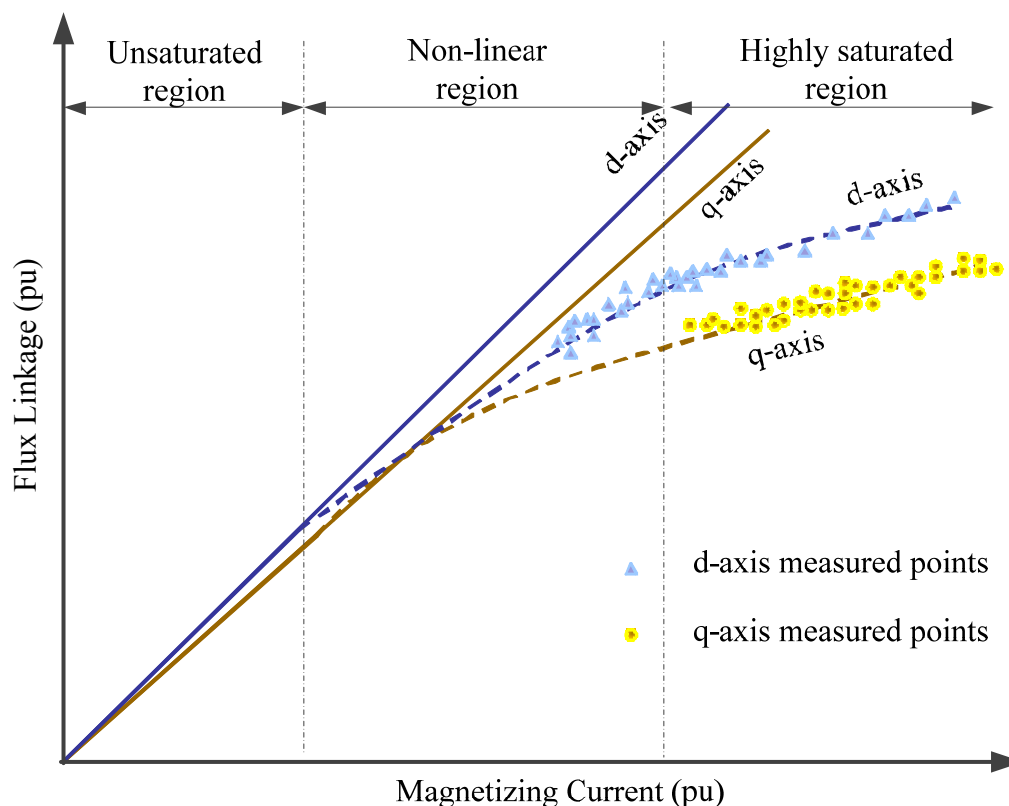
Fig. 1.1. Typical magnetization characteristics of electrical machines.

machines, it is necessary to use a precise and accurate mathematical representation of the magnetizing saturation. The magnetic flux in the direct and quadrature axes of synchronous machines is influenced by magnetization phenomenon. Thus, it will be useful to have a synchronous machine model integrated with an accurate magnetization model in algebraic configuration that makes it valuable in understanding the system behavior [6]-[24]. Typical magnetization characteristics of an electrical machine is presented in Fig. 1.1. At low magnetizing current values, the flux linkage is proportionately related to the current. This region is called the unsaturated region. For high values of the magnetizing

current, the flux linkage in the machine reaches its maximum level, which is known as the highly saturated region. The transition between unsaturated and highly saturated regions takes place in the non-linear region. As illustrated in Fig. 1.1, the flux linkage is not proportionally related to the magnetizing current in this region [5].

The magnetization model in an electrical machine is a mathematical realization of the machine magnetization behavior. However, in most of the applications, there is a collection of experimentally obtained magnetization data points. This information, without some knowledge of how the current and flux linkage are related, is not useful. Therefore, employing an algorithm which can create a functional relationship and produce meaningful information will be useful in machine modeling. The various techniques used are intended to address inclusion of magnetization phenomenon into the electrical machine model [6]- [24].

Researchers have employed numerous methods to incorporate the magnetization phenomenon into the machine model. A transient saturated model for squirrel cage induction machines is proposed in [9] based on an assumption that the air-gap flux saturation harmonics are produced by the fundamental component of the air-gap flux. In this model, the magnetization is included directly by using the fundamental and third harmonic factors. This model can explicitly be used for induction machines. One particular method employs variable effective air-gap length [10] to represent magnetization in the machine model. As a very popular method, the magnetization is expressed by regression of the magnetic flux linkage data points into an nth order polynomial function using the least

square criterion in [11, 12]. Although this model is very easy to implement, the level of accuracy is affected by the order of the polynomial. Moreover this method is not adequately accurate when the number of data points is small. To acquire a more accurate curve in the case of a greater number of data points, a higher degree of the polynomial is required that results in a more complicated model. On the other hand, increasing the degree of the polynomial will not result in a more accurate regression function and also for some degrees it might even produce oscillation in the resultant curve. The study presented in [13], [14] includes a set of experimentally measured magnetization characteristics data points interpolated into rational-fraction functions. This approach to represent magnetization is accurate which gives it merit to be considered as a good regression method. In contrast with the polynomial method, the rational-fraction method generates smoother and less oscillatory functions. Although the rational method is known as a non-linear interpolation method, it can model a high number of observed magnetization data points with low degree in both the numerator and denominator. Therefore, in comparison with the polynomial functions, this method has fewer coefficients. Nevertheless, the main drawback is that the small number of data points results in some errors in the magnetization representation.

In [15], a mathematical relationship between magnetism and current is established using a semi-empirical method. This method can be used for any type of electrical machine. Nevertheless, since both excessive high and low values of the flux linkage are ignored, this method is not very accurate. In [16], the main flux magnetization characteris-

tic was modeled for induction machines based on the magnetizing current space vector and generalized flux space vector. A classic hyperbolic function is used in [17] to interpolate the Ψ-I characteristics of a ferromagnetic core. Although this method can be used for all kinds of electrical machines, the regression accuracy is not high. Authors in [18], [19] suggest the magnetic saturation characteristics be divided into three parts in which the unsaturated and highly saturated regions are expressed as linear functions, while the saturated part is approximated by an arctangent function. In [5] the same methodology is employed in spite of the fact that the saturated region is modeled by a hyperbolic function. Another method proposed by researchers is to express the magnetic flux linkage as a function of the excitation ampere-turns to represent saturation in the machine model. However, investigators in these papers made assumptions that may result in substantial inaccuracies in the determination of the machine performance. Moreover, it is not clear whether these magnetization models can be applied to all types of electrical machines [20]. In [21]- [23], the sinusoidal series for modeling data points is presented. In these papers, the discrete Fourier transform (DFT) approach is used to represent the B-H curve in transformers based on a discrete set of data points. In the developed model in [24], two additional sine and cosine terms at half the fundamental frequency are incorporated into the conventional DFT model to interpolate the data samples to a sinusoidal function. Although these models can be used as a general expression of magnetization in any type of electrical machine, the accuracy of the model is highly affected by the number of the cosine terms in the function.

By far, the most frequently used methods of regression employed by researchers to represent magnetization in electrical machine models are polynomial, rational-fraction and DFT. In the next chapter, the algorithms used to develop the aforementioned methods are explained in detail. In the subsequent chapters, these models are re-developed and used to validate the models proposed in this research. It will be shown that these proposed models can be considered as valid alternatives for the existing models to represent magnetization in electrical machines.

1.1.2.   *Synchronous Machine Modeling*

In performance analysis of electrical machines, it is essential to have a closed-form mathematical expression that provides a precise description of the system. For a complex system such as an electrical machine with significant non-linear magnetization properties of ferromagnetic materials, flux linkage-current relationship must be considered in the analyses to have more precise and realistic results. Therefore, development of a robust model based on the available data for magnetization means to increase the accuracy and reliability of the model [25]. In [18], a synchronous machine model with n number of d-axis damper circuits and m number of q- axis damper circuits is developed with the proposed magnetization model. In [26], magnetization and hysteresis models are incorporated into a state space synchronous machine model. A very detailed synchronous machine model is developed in [27] based on the operating point magnetization specification of a synchronous machine.

As a part of this research work, based on the proposed magnetization models two synchronous machine models are developed to be used in steady state and transient performance analysis of synchronous machines.

1.2. Thesis Objectives

The work presented in this thesis conforms to the following objectives:

1. New methods to represent all regions of magnetization characteristics in synchronous machines are developed. These models are capable for application to all kinds of electrical machines such as synchronous, permanent magnet synchronous and induction machines. The accuracy of these models is evaluated to ensure the level of reliability.

2. Since having a comprehensive machine model is very crucial to simulating and analyzing the machine behavior, this research is also focused on developing transient and steady state synchronous machine models incorporated with the magnetization models to make the machine model more realistic and accurate. Synchronous machine performance is investigated by conducting different analyses.

1.3. Thesis Organization

This thesis consists of six chapters and two appendices

Chapter 2 provides detailed information about the synchronous machine mathematical modeling as well as synchronous machine transient stability performance analysis theory. Moreover, in this chapter, three models to represent magnetization in electrical machines that have been used in the literature are introduced and explained in detail. These models are redeveloped in this research and the results of magnetization characteristics calculated by these models have been compared with those of the proposed models.

Chapters 3 and 4 present two new magnetization models using trigonometric and Levenberg-Marquardt algorithms, respectively. These chapters consist of the algorithm development and numerical analyses to validate the accuracy and reliability of the proposed models.

Chapter 5 consists of a comprehensive steady state synchronous machine model including the magnetization model proposed in Chapter 3.

Chapter 6 studies the magnetization effect on transient performance analysis of synchronous machines. The magnetization model developed in chapter 3 is used as the magnetization model in the investigations.

Chapter 7 includes the conclusion of this thesis and provides recommendations for future work.

Appendices A and B contain some auxiliary information used in this thesis.

Chapter 2

Literature Review on the Steady-State and Transient Analysis of Synchronous Machines

In this chapter synchronous machine modeling and transient stability analysis are presented. Additionally, three regression methods used to represent magnetization in electric machines in the literature are explained in detail.

2.1. Dynamic Synchronous Machine Model

The objective of this section is to introduce the detailed synchronous generator model which has been used in this research work. In this model for simplicity purposes, it is assumed that magnetization and hysteresis effects are negligible. A cross-section view of a three phase non-salient, two-pole synchronous machine used in the performance analyses
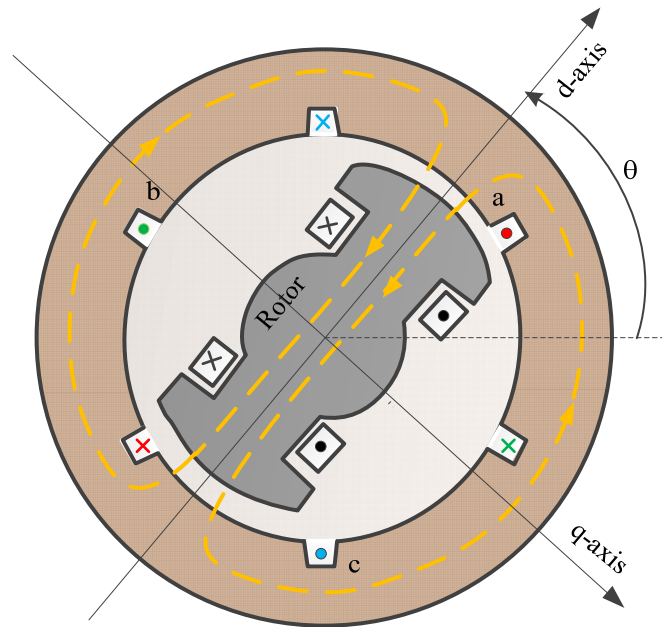
Fig. 2.1. Cross-section view of a two-pole, salient pole synchronous machine

of synchronous machine in this research work is illustrated in Fig. 2.1. As shown in this diagram, a three phase synchronous machine model consists of three phase stator windings symmetrically distributed around the air-gap.

The rotor field in synchronous machines is produced by applying a DC current to the rotor field windings. This results in a sinusoidal distribution of flux in the air-gap of the synchronous machine. If the rotor is rotated by a prime mover such as a DC motor, a rotating field is produced in the air-gap which is also known as the excitation field. The induced voltages in the armature windings have the same magnitudes but they are 120 electrical degrees apart.

To obtain the synchronous generator mathematical model, the rotor reference frame is identified [1]. Inasmuch as all the rotor windings are distributed symmetrically with

respect to the orthogonal axes. By definition, the direct axis is centered magnetically in the center of the north pole and the quadrature axis lags it by 90 degrees.

The synchronous machine model order is defined by the total number of rotor windings on its two orthogonal axes. Fig. 2.2 shows the stator and rotor circuits of a 2×2 synchronous machine model used in this research. As shown in this figure, a 2×2 synchronous machine model consists of one damper circuit and the field winding along the direct axis, and two damper circuits along the quadrature axis. Field and damper windings are also placed along the rotor. As illustrated in this figure, the damper circuits can be modeled by short-circuited windings along the direct and quadrature axes. The angle θ is the rotor position with respect to the stator.

To have a steady torque, the rotating fields of the stator and rotor must have equal speed which is called synchronous speed. This speed for a p-pole machine is calculated as
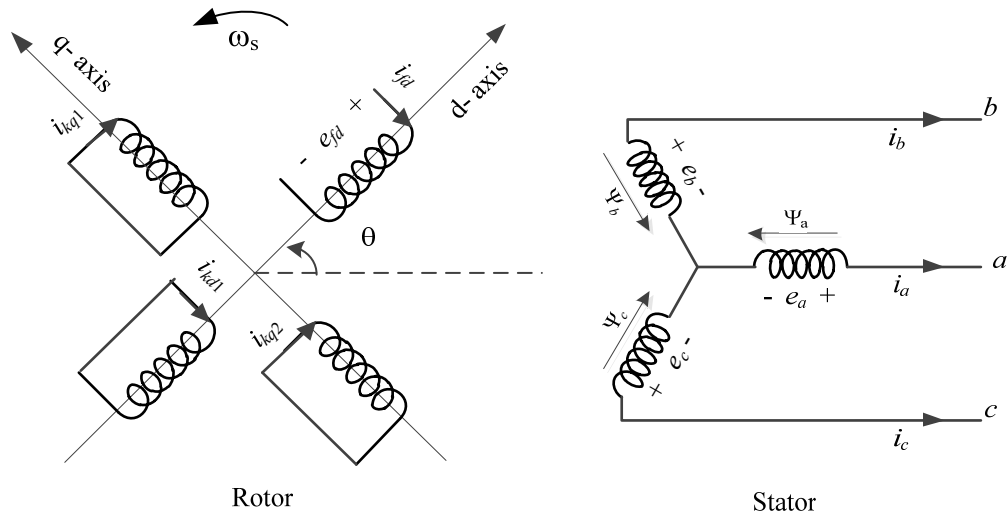
Fig. 2.2. Circuit diagram for the rotor and stator of a 2×2 synchronous generator model.

$$n_s = \frac{120f}{p} = \frac{60\omega_s}{\pi p} \tag{2.1}$$

where f is the frequency in Hz, $\omega_s = 2\pi f$ is the angular frequency in rad/s, and n_s is the synchronous speed in rpm.

2.1.1. Stator and Rotor Mathematical Modeling

Assuming that the stator windings are distributed sinusoidally, the *mmf* wave of each phase is sinusoidal with 120 electrical degrees apart in space with respect to each adjacent phase. Therefore, we have

$$\left. \begin{aligned} mmf_a &= ki_a \cos \gamma \\[2mm] mmf_b &= ki_b \cos\left(\gamma - \frac{2\pi}{3} \right) \\[2mm] mmf_c &= ki_c \cos\left(\gamma + \frac{2\pi}{3} \right) \end{aligned} \right\} \tag{2.2}$$

in which γ is the angle along the periphery of the stator and the center of phase a. The phase current can be defined by

$$\left. \begin{aligned} i_a &= I_m \cos(\omega_s t) \\[2mm] i_b &= I_m \cos\left(\omega_s t - \frac{2\pi}{3} \right) \\[2mm] i_c &= I_m \cos\left(\omega_s t + \frac{2\pi}{3} \right) \end{aligned} \right\}. \tag{2.3}$$

The total amount of *mmf* is calculated by

$$mmf_{total} = mmf_a + mmf_b + mmf_c = 3kI_m \cos(\gamma - \omega_s t) \tag{2.4}$$

Therefore, the total *mmf* is a sinusoidal waveform. (2.4) indicates that *mmf* in synchronous machines rotates at the constant angular velocity of ω_s. Therefore, for a balanced operating condition in synchronous machine, stator field and rotor must rotate at the same speed.

Considering Fig. 2.2, the voltage equations for the three phases can be written as

$$\left. \begin{aligned} e_a &= \frac{d\Psi_a}{dt} - R_a i_a \\[2em] e_b &= \frac{d\Psi_b}{dt} - R_a i_b \\[2em] e_c &= \frac{d\Psi_c}{dt} - R_a i_c \end{aligned} \right\}. \tag{2.5}$$

The flux linkages in the three phases are expressed by

$$\begin{bmatrix} \Psi_a \\ \Psi_b \\ \Psi_c \end{bmatrix} = \begin{bmatrix} -l_{aa} & -l_{ab} & -l_{ac} & l_{afd} & l_{akd1} & l_{akq1} & l_{akq2} \\ -l_{ab} & -l_{bb} & -l_{bc} & l_{bfd} & l_{bkd1} & l_{bkq1} & l_{bkq2} \\ -l_{ac} & -l_{bc} & -l_{cc} & l_{cfd} & l_{ckd1} & l_{ckq1} & l_{ckq2} \end{bmatrix} \times \begin{bmatrix} i_a \\ i_b \\ i_c \\ i_{fd} \\ i_{kd1} \\ i_{kq1} \\ i_{kq2} \end{bmatrix}. \tag{2.6}$$

The rotor circuit voltage equations are

$$\left. \begin{aligned} e_{fd} &= \frac{d\Psi_{fd}}{dt} + R_{fd}i_{fd} \\[2ex] 0 &= \frac{d\Psi_{kd1}}{dt} + R_{kd1}i_{kd1} \\[2ex] 0 &= \frac{d\Psi_{kq1}}{dt} + R_{kq1}i_{kq1} \\[2ex] 0 &= \frac{d\Psi_{kq2}}{dt} + R_{kq2}i_{kq2} \end{aligned} \right\}. \tag{2.7}$$

Since the rotor has a cylindrical structure, the self-inductance of the rotor circuits as well as their mutual inductances does not depend on the rotor position θ. Only the mutual inductances between the rotor and the stator are affected by the rotor position. Therefore, we have,

$$\begin{bmatrix} \Psi_{fd} \\ \Psi_{kd1} \\ \Psi_{kq1} \\ \Psi_{kq2} \end{bmatrix} = \begin{bmatrix} -l_{afd} & -l_{bfd} & -l_{cfd} & l_{fd} & l_{fdkd1} & 0 & 0 \\ -l_{akd1} & -l_{bkd1} & -l_{ckd1} & l_{fdkd1} & l_{kd1} & 0 & 0 \\ -l_{akq1} & -l_{bkq1} & -l_{ckq1} & 0 & 0 & l_{kq1} & l_{kq1kq2} \\ -l_{akq2} & -l_{bkq2} & -l_{ckq2} & 0 & 0 & l_{kq2kq1} & l_{kq2} \end{bmatrix} \times \begin{bmatrix} i_a \\ i_b \\ i_c \\ i_{fd} \\ i_{fkd1} \\ i_{kq1} \\ i_{kq2} \end{bmatrix}. \tag{2.8}$$

The stator mutual and self-inductances in (2.8) can be defined by (2.9) and (2.10), respectively.

$$l_{aa} = L_{aa0} + L_{aa2} \cos 2\theta$$

$$l_{bb} = L_{aa0} + L_{aa2} \cos 2\left(\theta - \frac{2\pi}{3}\right)$$

$$l_{cc} = L_{aa0} + L_{aa2} \cos 2\left(\theta + \frac{2\pi}{3}\right)$$

(2.9)

and

$$l_{ab} = l_{ba} = -L_{ab0} - L_{ab2} \cos\left(2\theta + \frac{\pi}{3}\right)$$

$$l_{bc} = l_{cb} = -L_{ab0} - L_{ab2} \cos(2\theta - \pi)$$

$$l_{ca} = l_{ac} = -L_{ab0} - L_{ab2} \cos\left(2\theta - \frac{\pi}{3}\right)$$

(2.10)

where

$$L_{aa0} = L_{al} + N_a^2\left(\frac{P_d + P_q}{2}\right)$$

$$L_{aa2} = N_a^2\left(\frac{P_d - P_q}{2}\right) = L_{ab2}$$

$$L_{ab0} = L_{abl} + N_a^2\left(\frac{P_d + P_q}{4}\right)$$

(2.11)

P_d and P_q are the permeance coefficients of the d- and q-axis, respectively and N_a is the effective winding turns in phase a. L_{al} and L_{abl} are the self and inductance flux leakages

that are not crossing the air-gap. Similarly, the stator-rotor mutual inductances can be defined by (2.12):

$$
\left.
\begin{aligned}
l_{afd} &= L_{afd} \cos\theta \\[2ex]
l_{akd1} &= L_{akd1} \cos\theta \\[2ex]
l_{akq1} &= -L_{akq1} \sin\theta \\[2ex]
l_{akq2} &= -L_{akq2} \sin\theta
\end{aligned}
\right\}.
\tag{2.12}
$$

Equation (2.8) completely describes the mathematical equation of a synchronous machine. However, it contains the stator currents and the d- and q-axes currents which result in a very complex calculation.

2.1.2.   *Park's Transformation Model*

One of the most widely used methods to convert the stator quantity values such as voltage, current, or flux into their corresponding rotor quantity values is Park's transformation [28], This transformation can be defined by the following matrix equation

$$
\begin{bmatrix} \Lambda_d \\ \Lambda_q \\ \Lambda_0 \end{bmatrix} =
\begin{bmatrix}
\cos\theta & \sin\theta & 1 \\
\cos\left(\theta - \dfrac{2\pi}{3}\right) & \sin\left(\theta - \dfrac{2\pi}{3}\right) & 1 \\
\cos\left(\theta + \dfrac{2\pi}{3}\right) & \sin\left(\theta + \dfrac{2\pi}{3}\right) & 1
\end{bmatrix}
\times
\begin{bmatrix} \Lambda_a \\ \Lambda_b \\ \Lambda_c \end{bmatrix}
\tag{2.13}
$$

in which Λ can be replaced by voltage, current, or flux. It should be noted that under the balanced condition we have

$$\Lambda_a + \Lambda_b + \Lambda_c = 0 \tag{2.14}$$

Therefore, $\Lambda_0 = 0$. The inverse transformation can be defined as:

$$
\begin{bmatrix} \Lambda_a \\ \Lambda_b \\ \Lambda_c \end{bmatrix} =
\begin{bmatrix}
\cos\theta & -\sin\theta & 1 \\
\cos\left(\theta - \dfrac{2\pi}{3}\right) & -\sin\left(\theta - \dfrac{2\pi}{3}\right) & 1 \\
\cos\left(\theta + \dfrac{2\pi}{3}\right) & -\sin\left(\theta + \dfrac{2\pi}{3}\right) & 1
\end{bmatrix} \times
\begin{bmatrix} \Lambda_d \\ \Lambda_q \\ \Lambda_0 \end{bmatrix} \tag{2.15}
$$

2.1.3. Rotor Reference Frame Equations

Using the transformation equation in (2.13) to convert the flux linkages and currents in (2.6) and (2.8), one can obtain

$$
\begin{bmatrix} \Psi_d \\ \Psi_q \\ \Psi_0 \end{bmatrix} =
\begin{bmatrix}
-L_d & L_{afd} & L_{akd1} & 0 & 0 & 0 & 0 \\
0 & 0 & 0 & -L_q & L_{akq1} & L_{akq2} & 0 \\
0 & 0 & 0 & 0 & 0 & 0 & -L_0
\end{bmatrix} \times
\begin{bmatrix} i_d \\ i_{fd} \\ i_{kd1} \\ i_q \\ i_{kq1} \\ i_{kq2} \\ i_0 \end{bmatrix} \tag{2.16}
$$

where the direct and quadrature inductances can be defined in (2.17)

$$L_d = L_{aa0} + L_{ab0} + \frac{3}{2}L_{aa2}$$

$$L_q = L_{aa0} + L_{ab0} - \frac{3}{2}L_{aa2} \Bigg\}$$ (2.17)

$$L_0 = L_{aa0} - 2L_{ab0}$$

and

$$
\begin{bmatrix} \Psi_{fd} \\ \Psi_{kd1} \\ \Psi_{kq1} \\ \Psi_{kq2} \end{bmatrix} = \begin{bmatrix} -\frac{3}{2}L_{afd} & L_{fd} & L_{kd1fd} & 0 & 0 & 0 \\ -\frac{3}{2}L_{akd1} & L_{kd1fd} & L_{kd1} & 0 & 0 & 0 \\ 0 & 0 & 0 & -\frac{3}{2}L_{akq1} & L_{kq1} & L_{kq1kq2} \\ 0 & 0 & 0 & -\frac{3}{2}L_{akq2} & L_{kq1kq2} & L_{kq2} \end{bmatrix} \times \begin{bmatrix} i_d \\ i_{fd} \\ i_{kd1} \\ i_q \\ i_{kq1} \\ i_{kq2} \end{bmatrix}.
$$ (2.18)

Therefore, stator voltage equations in (2.5) can be converted to d-q components as follows [1]

$$e_d = \frac{d\Psi_d}{dt} - \omega_r \Psi_q - R_a i_d$$

$$e_q = \frac{d\Psi_q}{dt} + \omega_r \Psi_d - R_a i_q \Bigg\}$$ (2.19)

$$e_0 = \frac{d\Psi_0}{dt} - R_a i_0$$

where ω_r is the angular velocity of the rotor. For the steady state operating situation we have

$$@ f = 60\,\text{Hz} \rightarrow \omega_r = \omega_s = 2\pi \times 60 = 377\,\text{rad/s} \tag{2.20}$$

2.1.4. Power and Torque Equations:

The three-phase output power can be calculated in the rotor reference frame as

$$P_o = \frac{3}{2}\left(e_d i_d + e_q i_q\right) \tag{2.21}$$

Substituting the voltage component from (2.19) in (2.21), (2.22) can be written as

$$P_o = \frac{3}{2}\left[\underbrace{\left(i_d \frac{d\Psi_d}{dt} + i_q \frac{d\Psi_q}{dt} + 2i_0 \frac{d\Psi_0}{dt} \right)}_{\text{rate of change in armature magnetic energy}} + \omega_r \underbrace{\left(\Psi_d i_q - \Psi_q i_d\right)}_{\text{air-gap power}} - \underbrace{\left(i_d^2 + i_q^2 + 2i_0^2 \right) R_a}_{\text{armature resistance loss}} \right]. \tag{2.22}$$

Consequently, the air-gap torque can be expressed by

$$T_e = \frac{\text{air - gap power}}{\omega_{\text{mech}}} = \frac{3\omega_r}{2\omega_{\text{mech}}}\left(\Psi_d i_q - \Psi_q i_d\right). \tag{2.23}$$

2.1.5.   Per-unit Calculations

In lights of the fact that using per-unit system results in simplified computational analyses, all the performance analyses are conducted in per-unit system in this research. By definition,

$$\text{Per unit value} = \frac{\text{Actual value}}{\text{Base value}}. \tag{2.24}$$

In this work, the machine ratings are chosen as the base quantities in the per unit calculations. Tables 2.1- 2.3 summarize the per-unit equations used in this research. It should be noted that hereafter all the quantities used in this thesis are in per unit unless the unit is specified.

2.1.6. *The Synchronous Machine d- and q-axis Equivalent Circuits*

Based on the equations developed in the previous section, Figs. 2.3-a and -b provide the synchronous machine direct and quadrature axes equivalent circuits, respectively.

Table 2.1. Base Quantities Used in the Per-unit System

e_B: Peak value of rated line to neutral voltage
i_B: Peak value of rated line current, (A)
f_B: Rated frequency, (HZ)
ω_B : $2\pi f_B$, elec. (rad/second)

Table 2.2. Stator Per-unit Equations

$\omega_{mB} = \omega_B(\dfrac{2}{p})$, mech.(rad/second)	$\Psi_{sB} = \dfrac{e_B}{\omega_B}$, (weber-turns)
$Z_{sB} = \dfrac{e_{sB}}{i_{sB}}$, ($\Omega$)	3-phase $VA_B = \dfrac{3}{2} e_{sB} . i_{sB}$, (V A)
$L_{sB} = \dfrac{Z_{sB}}{\omega_B}$, (H)	$T_{sB} = \dfrac{3\text{-phase } VA_B}{\omega_{mB}}$ (N-m)
$i_{fdbase} = \dfrac{L_{md}}{L_{afd}} i_{sB}$ (A)	$i_{kdB} = \dfrac{L_{md}}{L_{akd}} i_{sB}$ (A)
$i_{fkqB} = \dfrac{L_{md}}{L_{akq}} i_{sB}$ (A)	$Z_{fdB} = \dfrac{L_{md}}{L_{afd}} i_{sB}$ (A)

Table 2.3. Rotor Per-unit Equations

$e_d = \dfrac{1}{\omega_B}\left(-\omega_B R_a i_d + \dfrac{d\Psi_d}{dt} - \omega_B \omega_r \Psi_q\right)$	$e_q = \dfrac{1}{\omega_B}\left(-\omega_B R_a i_q + \dfrac{d\Psi_q}{dt} + \omega_B \omega_r \Psi_d\right)$
$e_{fd} = \dfrac{1}{\omega_B}\left(\omega_B R_{fd} i_{fd} + \dfrac{d\Psi_{fd}}{dt}\right)$	$0 = \dfrac{1}{\omega_B}\left(\omega_B R_{kd1} i_{kd1} + \dfrac{d\Psi_{kd1}}{dt}\right)$
$0 = \dfrac{1}{\omega_B}\left(\omega_B R_{kq1} i_{kq1} + \dfrac{d\Psi_{kq1}}{dt}\right)$	$0 = \dfrac{1}{\omega_B}\left(\omega_B R_{kq2} i_{kq2} + \dfrac{d\Psi_{kq2}}{dt}\right)$
$\Psi_d = -\left(X_{md} + X_l\right)i_d + X_{md} i_{fd} + X_{md} i_{kd1}$	$\Psi_q = -\left(X_{mq} + X_l\right)i_q + X_{md} i_{kq1} + X_{md} i_{kq2}$
$\Psi_{fd} = -X_{md} i_d + X_{fd} i_{fd} + X_{kd1} i_{kd1}$	$\Psi_{kd1} = -X_{md} i_d + X_{md} i_{fd} + X_{kd1} i_{kd1}$
$\Psi_{kq1} = -X_{mq} i_q + X_{kq1} i_{kq1} + X_{mq} i_{kq2}$	$\Psi_{kq2} = -X_{mq} i_q + X_{mq} i_{kq1} + X_{kq2} i_{kq2}$

(a)

(b)
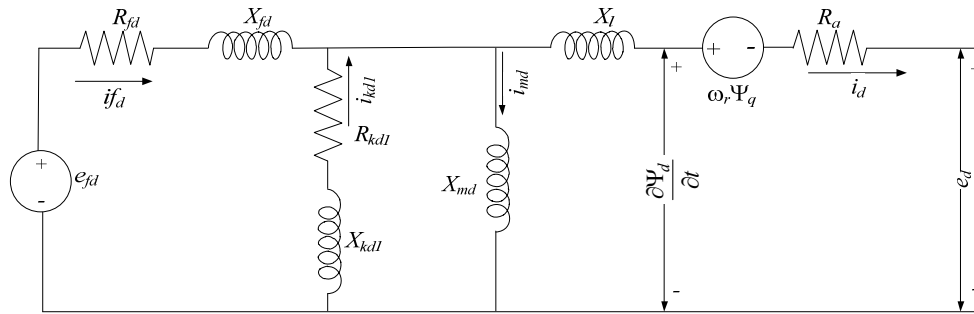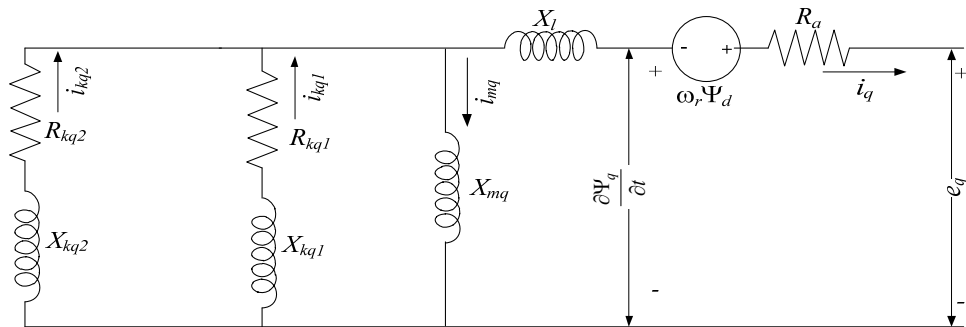
Fig. 2.3. 2×2 Synchronous generator model. (a) d-axisequivalent circuit. (b) q-axis equivalent circuit.

2.2. The State Space Synchronous Machine Model

In this section, a comprehensive saturated model for synchronous machines is presented. To describe the dynamic behavior of synchronous machines in time domain, the analysis of this section employs the state space modeling concept. Therefore, based on the dynamic equations of synchronous machines and their particular state variables, the state space model can be utilized to determine the future state of the machine provided that the present state and the excitation signals are known [29]. Firstly, consider a general non-linear system with multiple states and inputs as

$$\dot{x} = f\left(x_1,\ x_2,...x_n,u_1,u_2...,u_m\right) \tag{2.25}$$

where x_i is the ith vector of the state variables, u_j is the jth system driving variable, and f is a set of non-linear functions. Suppose the equilibrium points of x_{0i} and u_{0j} are defined such that $f(x_{01},\ ...,\ x_{0n},\ ...,\ u_{01},\ ...,\ u_{0m})=0$. If x_i and u_j are considered to be a perturbed state of the above system, (28) can be written as

$$\left. \begin{array}{llll} x_1 = x_{01} + \widetilde{x}_1 & x_2 = x_{02} + \widetilde{x}_2 & \cdots & x_n = x_{0n} + \widetilde{x}_n \\ u_1 = u_{01} + \widetilde{u}_1 & u_2 = u_{02} + \widetilde{u}_2 & \cdots & u_m = u_{0m} + \widetilde{u}_m \end{array} \right\}. \tag{2.26}$$

Note that at the equilibrium points, the function f is zero. The linearization of the system about the equilibrium point can be obtained using Taylor series expansion and by ignoring the second and higher order terms as

$$\dot{x} = f(x_1, \ldots x_n, u_1, \ldots, u_m) \cong \sum_{i=1}^{n} \left. \frac{\partial f}{\partial x_i} \right|_{\left(\substack{x_i = x_{0i} \\ u_i = u_{0i}} \right)} \tilde{x}_i + \sum_{i=1}^{n} \left. \frac{\partial f}{\partial u_i} \right|_{\left(\substack{x_i = x_{0i} \\ u_i = u_{0i}} \right)} \tilde{u}_i.$$ (2.27)

Therefore, for small perturbation of a non-linear system around the equilibrium point the linear state space model of the system can be written

$$\left. \begin{array}{l} \dot{\mathbf{X}} = \mathbf{AX} + \mathbf{BU} \\ \mathbf{Y} = \mathbf{CX} + \mathbf{DU} \end{array} \right\}$$ (2.28)

in which **A**, **B**, **C**, and **D** are called the system, input, output, and feed-forward coefficient matrices, respectively. Considering $\mathbf{X_0}$ as the initial condition of the system, applying the Laplace transformation to the state space equations in (2.28), we have

$$s\mathbf{X}(s) - \mathbf{X}_0 = \mathbf{AX}(s) + \mathbf{BU}(s).$$ (2.29)

Therefore,

$$(s\mathbf{I} - \mathbf{A})\mathbf{X}(s) = \mathbf{X}_0 + \mathbf{BU}(s).$$ (2.30)

It yields,

$$\mathbf{X}(s) = (s\mathbf{I} - \mathbf{A})^{-1} \mathbf{X}_0 + (s\mathbf{I} - \mathbf{A})^{-1} \mathbf{BU}(s).$$ (2.31)

It can be proven that

$$(s\mathbf{I} - \mathbf{A})^{-1} = L(e^{\mathbf{A}t}).$$ (2.32)

Therefore, state space equations in time-domain can be described as

$$\left.\begin{aligned} \mathbf{X}(t) &= e^{\mathbf{A}(t-t_0)}\mathbf{X}_0 + \int_{t_0}^{t} e^{\mathbf{A}(t-\tau)}\mathbf{B}\mathbf{U}(\tau)d\tau \\[2em] \mathbf{Y}(t) &= \mathbf{C}\mathbf{X}(t) + \mathbf{D}\mathbf{U}(t) \end{aligned}\right\} \tag{2.33}$$

2.3. Fault Analysis

In a power system, an abrupt disturbance that causes a deviation from normal operation conditions of the power equipment is generally called a fault. Based on the nature of the fault, they are classified into two groups. The first type of failures is short-circuiting faults. They may occur as a result of an insulation default in the apparatus due to degradation of electrical components over time or as a consequence of a sudden overvoltage situation. The other type of faults is categorized under open circuit faults as a result of an interruption in current flow [30].

In case of short-circuit fault occurrence in the transmission system, the fault must be cleared in the least amount of time possible to prevent the system from losing the synchronism and becoming unstable [31]. Therefore, part of this research is focused on performance analysis of a synchronous generator when it is subjected to a short-circuit interruption.

2.3.1. Classification of Short-circuit Faults

Weather conditions are one of the common factors causing short-circuit faults in power systems. Lightning, heavy rain and snow, floods, and fires near the electrical

equipment are some of the weather-related conditions that can cause a short-circuit failure.

Equipment failure due to aging, degradation, or poor installation of the machines, cables, transformers, etc. can be another cause of short-circuit failure. Short-circuit faults can also happen as a result of human error. For instance, this fault may happen during the re-energizing process of the system to be in service after maintenance due to some inadvertent mistakes[30], [31].

2.3.2.   *Effects of Short-circuit Faults on Power System Equipment*

The short-circuit effects on the power system equipment can be classified as either electrical or mechanical effects. Depending on duration of the short-circuit fault, the current passing through the conductors of the power system equipment may cause some thermal effects such as heating dissipations. On the other hand, electromagnetic forces and mechanical stresses caused by short-circuit interruption are considered to be mechanical effects. Mechanical effects of short-circuit failures may result in serious problems. Therefore, it is essential that the transformers windings are designed to tolerate electromagnetic forces. Also, if the cores in a three-phase unarmored cable are not bounded properly, the electromagnetic force due to the short-circuit fault, can cause the cores to repel from each other which may result in bursting and installation damages [30].

2.4. Transient Stability Analysis

In the previous section, short-circuit faults as a common source of failures in power systems was presented. In this section, transient stability analysis is briefly introduced. More information for further reading is available in [1], [29].

By definition, transient stability is the ability of a system to sustain synchronism after it is subjected to sever transient disturbances. Through a part of this research, the magnetization effect on the synchronous generator transient stability in the case of a short-circuit fault is investigated.

It should be noted that after the fault occurs, the circuit breakers at both ends of the faulted circuit will be activated to isolate the circuit and clear the fault. The fault clearing time depends on the speed of time at which the circuit breakers can perform.

Firstly, let us consider fault location F_1 to be at the high voltage transmission (HT) bus as indicated in Fig. 2.4-a. For simplicity it is assumed that the stator and transformer resistors are small and can be neglected. Therefore, in this situation, no active power is transmitted to the infinite bus during the fault and the short-circuit current flows through the pure reactance.

If the fault occurs at location F_2 as shown in Fig. 2.4-b, some active power will be transmitted to the infinite bus during the fault. Figs 2.4-d and 2.4-e demonstrate the active power P graph with respect to the load angle δ for stable and unstable situations, respectively, based on the fault duration.

Suppose that the system is subjected to the fault at $t=t_0$ and the fault is cleared at $t=t_1$. First, let us examine the stable situation shown in Fig. 2.4-d. As can be seen in this figure, before the fault the system operates at the pre-fault state of operation. At $t=t_0$, one of the circuits is subjected to the fault. Therefore, the operating point suddenly drops from point a to b. As a result of inertia, load angle cannot suddenly change. Since $P_e < P_m$, the rotor starts accelerating until point c, at which the fault is cleared by activation of the circuit breakers and isolating the faulted circuit from the network. Therefore, the operating point abruptly changes to point d. At this time, since $P_m < P_e$, the rotor starts decelerating. However, the load angle continues increasing because during the fault the rotor speed is increased to more than synchronous speed (ω_0, δ_0). Therefore, the load angle increases until the kinetic energy gained by the machine during the acceleration (area A_1) is expended. When the operating point reaches to d ($t=t_2$)at which we have $A_1=A_2$ the rotor speed is the synchronous speed and load angle is maximum. Since $P_m < P_e$ remains true the rotor speed and the load angle decrease. If there is no source of damping in the network, the operating point oscillates between points e and d.

With the longer fault duration illustrated in Fig. 2.4-e, the area A_1 representing to the energy gained during the fault is greater than area A_2. Therefore, after the fault is cleared at point e, the kinetic energy is not completely expended in the system. As a result, the speed and the load angle both increase. The speed never reaches the synchronous speed, and the system will become unstable.

Based on the above discussion, one can conclude that the transient stability in synchronous generators in short-circuit interruptions is affected by the following factors:

- Load of the generator

- Location of the fault

- Fault clearing time

- Post-fault transmission circuit resistance

- Generator reactance: The greater this reactance is, the greater the peak power; this results in having less initial load angle.

- Generator inertia: For the generators with greater amount of inertia, the kinetic energy gained during the fault is smaller

- Infinite bus voltage magnitude
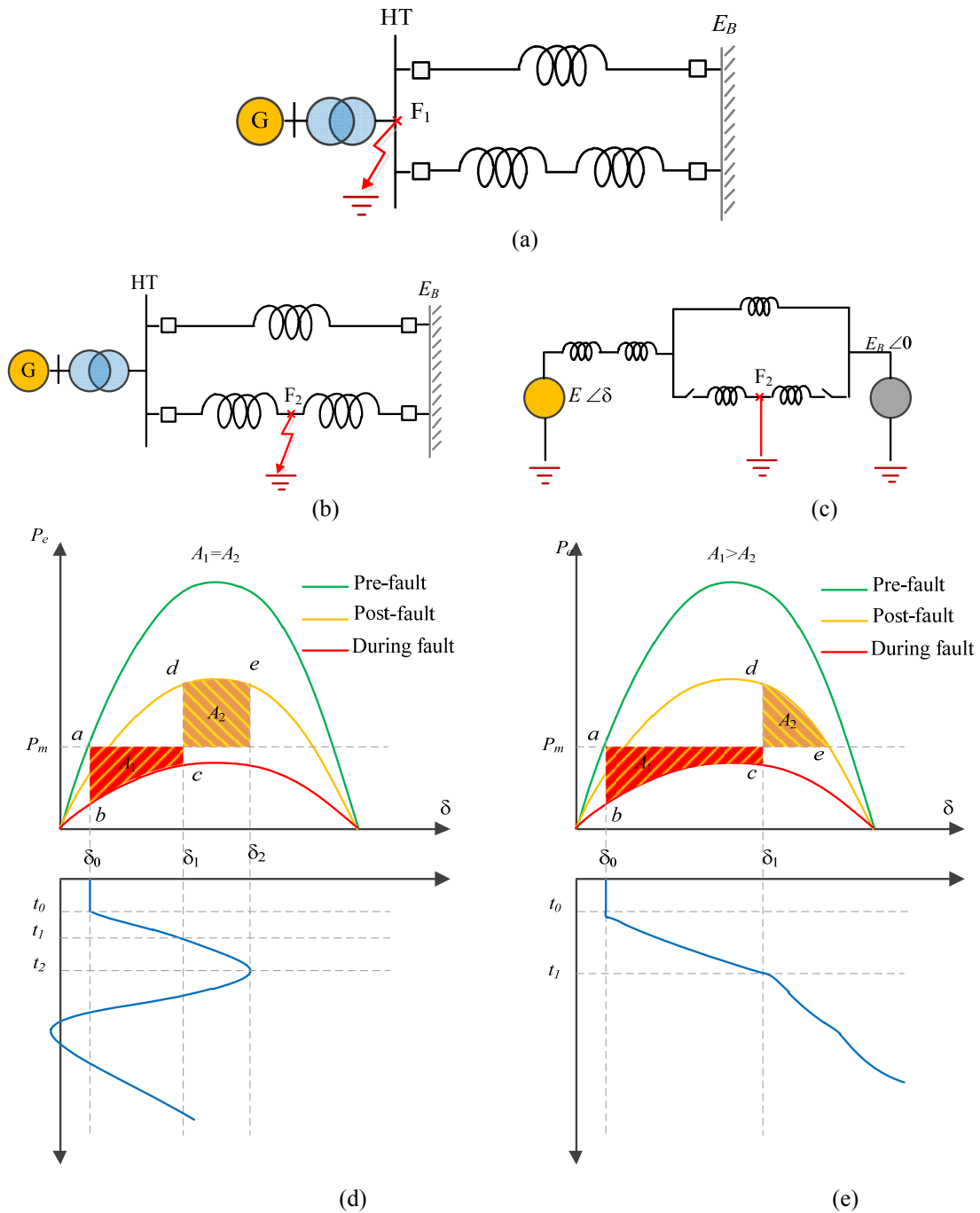
Fig. 2.4. Transient stability concept in power systems. (a) Short-circuit fault in a single distribution line at the (HT) bus. (b) Short-circuit fault in a single distribution line at a distance away from the HT bus. (c) Post-fault Equivalent circuit. (d) System response to the fault - Stable mode. (e)System response to the fault - Unstable mode.

2.5. The Previous Models Used to Represent Magnetization

In this section, three methods to represent magnetization in electrical machines used by the researchers are explained. These models are developed in this research work to be used in comparison investigations to validate the proposed models.

2.5.1. *Polynomial Regression Algorithm*

Polynomial regression is one of the most commonly used methods in representation of magnetization characteristics in electrical machines. Fig. 2.5 illustrates a representation
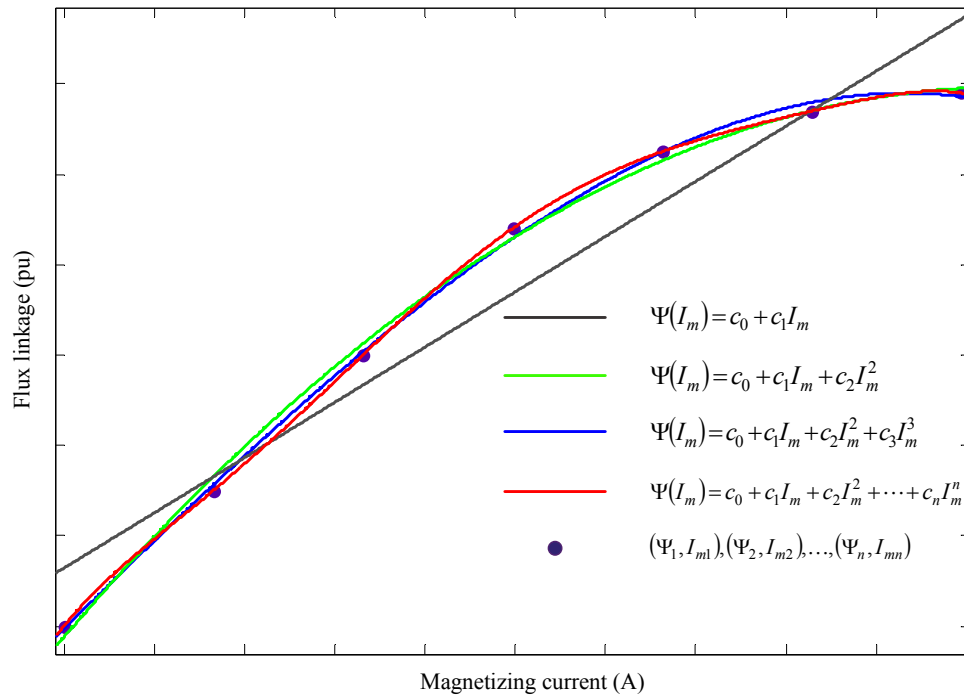
Fig. 2.5. A set of flux linkage data points and their corresponding magnetizing currents represented by different degrees of polynomials.

of a set of flux linkage data points and their corresponding magnetizing currents by different degrees of polynomials. In general, n number of data points can be interpolated by a set of polynomials from a straight line ($k=2$) to a polynomial of degree $k=n$-1.

Suppose that for the available set of magnetization data points the function is expressed in the form of a polynomial of degree k as

$$\Psi(I_m) = c_0 + c_1 I_m + c_2 I_m^2 + \cdots + c_k I_m^k = c_0 + \sum_{i=1}^{k} c_i I_m^i. \tag{2.34}$$

To assure that the curve is the best-fit curve of the data points, the least square method is employed. In this technique, the error function is defined as sum of the squared deviations from the data points.

$$\varepsilon = \sum_{j=1}^{n} \left[\Psi(I_{mj}) - \Psi_j \right]^2. \tag{2.35}$$

Substituting the calculated flux linkage from (2.34), (2.36) can be written as

$$\varepsilon = \sum_{j=1}^{n} \left[c_0 + \sum_{i=1}^{k} c_i I_{mj}^i - \Psi_j \right]^2. \tag{2.36}$$

According to the least square error method [32], [33], the regression algorithm will be successful if the error is minimized by

$$\frac{\partial \varepsilon}{\partial c_0} = \frac{\partial \varepsilon}{\partial c_1} = \frac{\partial \varepsilon}{\partial c_2} = \cdots = \frac{\partial \varepsilon}{\partial c_k} = 0. \tag{2.37}$$

Considering (2.36) and (2.37), the following equations can be obtained

$$\left.\begin{array}{l} \dfrac{\partial \varepsilon}{\partial c_0} = 2\sum_{j=1}^{n}\left[c_0 + \sum_{i=l}^{k} c_i I_{mj}^{i} - \Psi_j\right] = 0 \\[4mm] \dfrac{\partial \varepsilon}{\partial c_1} = 2\sum_{j=1}^{n}\left[c_0 + \sum_{i=l}^{k} c_i I_{mj}^{i} - \Psi_j\right]\cdot I_m = 0 \\[4mm] \dfrac{\partial \varepsilon}{\partial c_2} = 2\sum_{j=1}^{n}\left[c_0 + \sum_{i=l}^{k} c_i I_{mj}^{i} - \Psi_j\right]\cdot I_m^2 = 0 \\[2mm] \vdots \\[2mm] \dfrac{\partial \varepsilon}{\partial c_k} = 2\sum_{j=1}^{n}\left[c_0 + \sum_{i=l}^{k} c_i I_{mj}^{i} - \Psi_j\right]\cdot I_m^k = 0 \end{array}\right\}. \tag{2.38}$$

Consequently,

$$\left.\begin{array}{l} nc_0 + c_1 \sum_{j=1}^{n} I_m + c_2 \sum_{j=1}^{n} I_m^2 + \cdots + c_k \sum_{j=1}^{n} I_m^k = \sum_{j=1}^{n} \Psi_j \\[4mm] c_0 \sum_{j=1}^{n} I_m + c_1 \sum_{j=1}^{n} I_m^2 + c_2 \sum_{j=1}^{n} I_m^3 + \cdots + c_k \sum_{j=1}^{n} I_m^{k+1} = \sum_{j=1}^{n} \left(\Psi_j I_m\right) \\[4mm] c_0 \sum_{j=1}^{n} I_m^2 + c_1 \sum_{j=1}^{n} I_m^3 + c_2 \sum_{j=1}^{n} I_m^4 + \cdots + c_k \sum_{j=1}^{n} I_m^{k+2} = \sum_{j=1}^{n} \left(\Psi_j I_m^2\right) \\[4mm] c_0 \sum_{j=1}^{n} I_m^k + c_1 \sum_{j=1}^{n} I_m^{k+1} + c_2 \sum_{j=1}^{n} I_m^{k+2} + \cdots + c_k \sum_{j=1}^{n} I_m^{k+k} = \sum_{j=1}^{n} \left(\Psi_j I_m^k\right) \end{array}\right\}. \tag{2.39}$$

The equations in (2.39) can be re-written in matrix format as in (2.40)

$$
\underbrace{\begin{bmatrix}
n & \sum\limits_{j=1}^{n} I_m & \sum\limits_{j=1}^{n} I_m^2 & \cdots & \sum\limits_{j=1}^{n} I_m^k \\[2em]
\sum\limits_{j=1}^{n} I_m & \sum\limits_{j=1}^{n} I_m^2 & \sum\limits_{j=1}^{n} I_m^3 & \cdots & \sum\limits_{j=1}^{n} I_m^{k+1} \\[2em]
\sum\limits_{j=1}^{n} I_m^2 & \sum\limits_{j=1}^{n} I_m^3 & \sum\limits_{j=1}^{n} I_m^4 & \cdots & \sum\limits_{j=1}^{n} I_m^{k+2} \\[2em]
\vdots & \vdots & \vdots & & \vdots \\[2em]
\sum\limits_{j=1}^{n} I_m^k & \sum\limits_{j=1}^{n} I_m^{k+1} & \sum\limits_{j=1}^{n} I_m^{k+2} & \cdots & \sum\limits_{j=1}^{n} I_m^{k+k}
\end{bmatrix}}_{\mathbf{A}}
\underbrace{\begin{bmatrix} c_0 \\[2em] c_1 \\[2em] c_2 \\[2em] \vdots \\[2em] c_k \end{bmatrix}}_{\mathbf{C}}
=
\underbrace{\begin{bmatrix}
\sum\limits_{j=1}^{n} \Psi_j \\[2em]
\sum\limits_{j=1}^{n} \left(\Psi_j I_m \right) \\[2em]
\sum\limits_{j=1}^{n} \left(\Psi_j I_m^2 \right) \\[2em]
\vdots \\[2em]
\sum\limits_{j=1}^{n} \left(\Psi_j I_m^k \right)
\end{bmatrix}}_{\mathbf{B}}
\cdot
\tag{2.40}
$$

Therefore the coefficients c_0, c_1, ..., c_k in (2.34) can be calculated using the matrix equation (2.41)

$$
\mathbf{C} = \mathbf{A}^{-1} \times \mathbf{B}
\tag{2.41}
$$

2.5.2.   Rational Regression Algorithm

This section represents the rational-fraction approximation method to represent magnetization in electrical machines. In the rational-fraction method, the magnetization is represented by a ratio of two polynomials. Therefore, at the *n* measurement of flux linkages, the magnetization characteristics can be described as a rational function of the general form of

$$
\Psi(i) = \frac{p_0 + p_1 i + \cdots + p_n i^n}{q_0 + q_1 i + \cdots + q_m i^m}
\tag{2.42}
$$

where the coefficients p_0, p_1, …, p_n and q_0, q_1, …, q_n must be determined to produce a suitable function passing through all the available data points [32], [33].

The rational functions are classified by the degree of the numerator and denominator polynomials. In this research quadratic rational functions are employed to represent the magnetization characteristics. A quadratic rational-fraction function can be defined by (2.43)

$$\Psi(i) = \frac{p_0 + p_1 i}{1 + q_1 i + q_2 i^2}. \tag{2.43}$$

Given a set of flux linkage data points and their corresponding magnetizing currents, the coefficients of the rational-fraction function in (2.43) can be computed using non-linear least square (NLS) estimation [34].

NLS is similar to the least squares method explained in the previous section. The only difference is that NLS is used in regression applications in which the regression function consists of non-linear parameters. In such curve fitting procedures, the model is initially approximated by a linear function and through the next iterations the error will be minimized and the desired fit will be calculated [35].

Therefore, the iteration starts with an initial guess for the coefficients in (2.43). Considering some information about the general pattern of magnetization characteristics may lead to have the initial guess closer to the ultimate results which results in more efficient iterative procedure. Realistic magnetization characteristics in electrical machines can be represented by a curve that starts at (0,0), increases with a positive deviation and ends at

(I_{max} Ψ_{max}). Therefore, the regression curve in (2.43) needs to be maximized at $i=I_{max}$. By calculating the first derivative of (2.43), one can obtain

$$\Psi'(i) = \frac{p_1}{1 + q_1 i + q_2 i^2} - \frac{(p_0 + p_1 i)(2iq_2 + q_1)}{(1 + q_1 i + q_2 i^2)^2}. \tag{2.44}$$

Solving (2.44) for i when $\Psi'(i) = 0$, yields

$$i_{max} = \frac{-p_0 q_2 \pm \sqrt{p_1^2 q_2 - p_0 p_1 q_1 q_2 + p_0^2 q_2^2}}{p_1 q_2}. \tag{2.45}$$

Inasmuch as general magnetization characteristics in electrical machine patterns necessitates (2.44) to be maximized at i_{max} where the second derivative is positive, the other root in (2.45) which produces a negative second derivative should be neglected. Substituting $i_{max}=I_{mn}$, (2.46) can be written as

$$\Psi_n = \frac{p_0 + p_1 I_{mn}}{1 + q_1 I_{mn} + q_2 I_{mn}^2}. \tag{2.46}$$

Next step is to make the regression function passing through ($I_{m0} = 0$, $\Psi_0 = 0$). Therefore, $p_0 = 0$ and (2.43) is reduced to

$$\Psi(i) = \frac{p_1 i}{1 + q_1 i + q_2 i^2}. \tag{2.47}$$

Consequently, the derivative function in (2.44) can be modified as

$$\Psi'(i) = \frac{p_1}{1 + q_1 i + q_2 i^2} - \frac{(p_1 i)(2iq_2 + q_1)}{(1 + q_1 i + q_2 i^2)^2} \tag{2.48}$$

and (2.45) is simplified as (2.49)

$$i_{max} = \pm \frac{1}{\sqrt{q_2}}. \tag{2.49}$$

Substituting i_{max} for the positive deviation in (2.47) yields,

$$\Psi_m = \frac{p_1}{2\sqrt{q_2} + q_1}. \tag{2.50}$$

This relationship between the coefficients is useful to produce a proper initial guess.

2.5.3.   DFT Regression Algorithm

As a trigonometric method to represent magnetization in electrical machines, researchers have used the discrete Fourier transformation (DFT). In this section the algorithm is explained in detail.

As illustrated in Fig. 2.6, for a mirrored magnetization characteristics curve (Ψ-I_m) expressed by a set of n measured data points Ψ_m and I_{mn}, the discrete Fourier transformation can be estimated for a finite number of data points as [21]- [23]:

$$\Psi(I_m) = a_0 + \sum_{j=1}^{k'} a_j \cos(\omega_j I_m) \tag{2.51}$$

in which the coefficients can be calculated by (2.52) and (2.53),
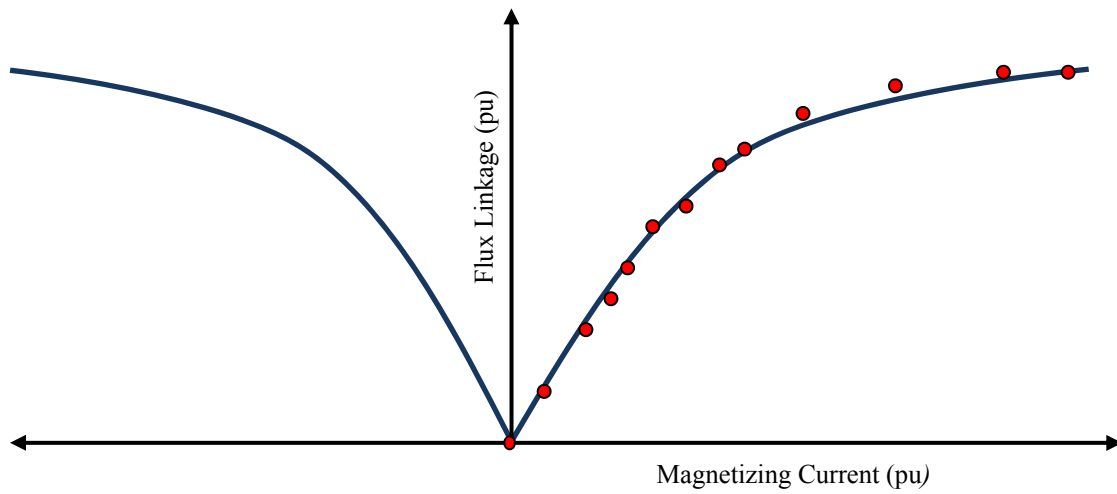
Fig. 2.6. Mirrored magnetization characteristics calculated by the DFT method.

$$\int\limits_{I_{k-1}}^{I_k}\Psi d_i \cong S = \frac{\left(I_k - I_{k-1}\right)\left(\Psi_{k-1} + \Psi_k\right)}{2}$$
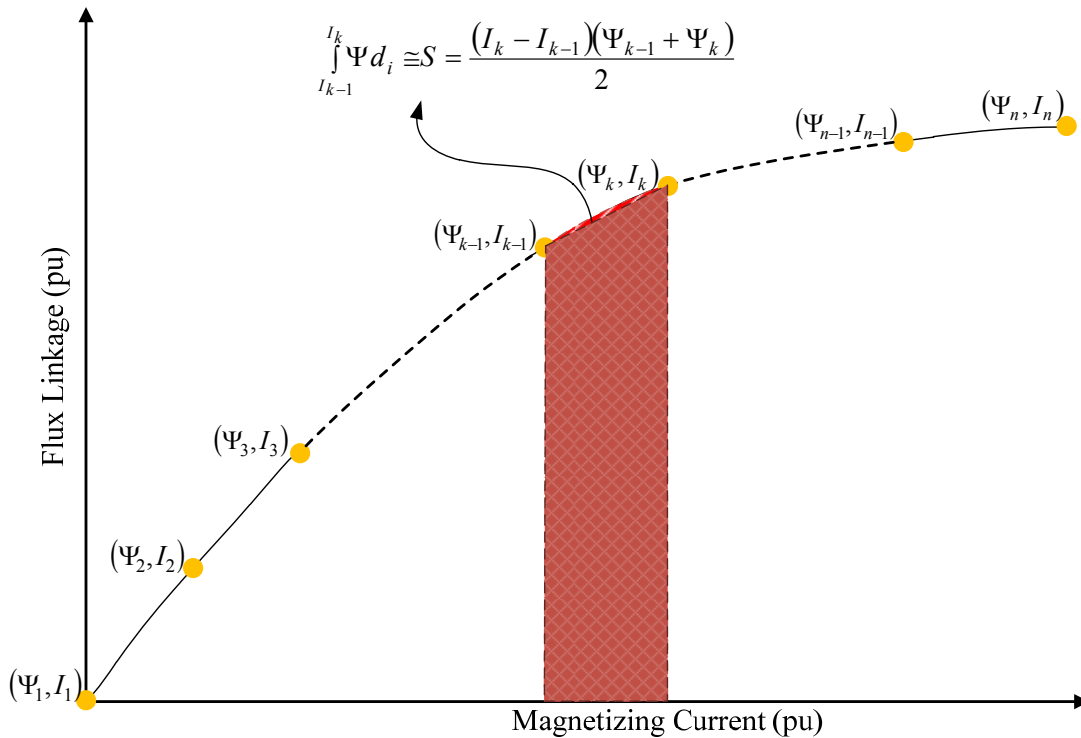
Fig. 2.7. Approximated integral calculation in the DFT method

$$a_0 = \frac{1}{I_{max}} \int_0^{I_{max}} \Psi(i) d_i \tag{2.52}$$

$$a_j = \frac{2}{I_{max}} \int_0^{I_{max}} \Psi(i) \cos(\omega_j i) di \tag{2.53}$$

To calculate the integrals in (2.52) and (2.53) the approximation demonstrated in Fig. 2.7 is employed. As seen in this figure the flux linkage-current relationship between each pair of data points can be approximated as a straight line joining them. Therefore, for the flux function between (Ψ_{k-1} and I_{k-1}) and (Ψ_k and I_k), we have

$$\Psi_k(i) = \frac{\Psi_k - \Psi_{k-1}}{I_k - I_{k-1}} \times i + \left(\Psi_{k-1} - \frac{\Psi_k - \Psi_{k-1}}{I_k - I_{k-1}} \times I_{k-1} \right) \tag{2.54}$$

Considering

$$\rho_k = \frac{\Psi_k - \Psi_{k-1}}{I_k - I_{k-1}} \tag{2.55}$$

(2.52) and (2.53) can be calculated as in (2.56) and (2.57), respectively.

$$a_0 = \frac{1}{I_{max}} \sum_{k=2}^{n} \int_{I_{k-1}}^{I_k} [\rho_k \times i + (\Psi_{k-1} - \rho_k \times I_{k-1})] d_i \tag{2.56}$$

and

$$a_j = \frac{2}{I_{max}} \sum_{k=2}^{n} \int_{I_{k-1}}^{I_k} [\rho_k \times i + (\Psi_{k-1} - \rho_k \times I_{k-1})] \times \cos(\omega_j i) d_i \tag{2.57}$$

Consequently, we have

$$a_0 = \frac{1}{I_{max}} \sum_{k=2}^{n} \left[\Psi_k (I_k - I_{k-1}) - \frac{1}{2} \rho_k (I_k - I_{k-1})^2 \right]$$

(2.58)

and

$$a_j = \frac{\rho_k}{\omega_j I_{max}} \sum_{k=2}^{n} \left\{ \frac{1}{\omega_j} \left[(I_k - I_{k-1}) \sin(\omega_j I_{k-1}) \right] + \frac{1}{\omega_j^2} \left[\cos(\omega_j I_k) - \cos(\omega_j I_{k-1}) \right] + \right.$$
$$\left. \frac{\Psi_k}{\omega_j} \left[\sin(\omega_j I_k) - \sin(\omega_j I_{k-1}) \right] \right\}$$

(2.59)

where ω_j, and I_{max} are defined as in (2.61)

$$\left. \begin{aligned} I_{max} &= I_{mn} \\ \omega_j &= \frac{j\pi}{I_{max}} \end{aligned} \right\}.$$

(2.60)

The accuracy of fit in this model depends on the number of cosine terms in (2.51). Then, one can define the DFT fitting order, k', as it is simply the number of sinusoidal terms found in the final interpolated curve. For instance, a flux linkage function of the DFT fitting order of four is a function consisting of four cosine terms. This order affects the accuracy of the resultant curve by using this method. In order to obtain more accurate results, the DFT order should be increased.

2.6. Conclusion

The detailed method on synchronous machine modeling is presented in this chapter. Short-circuit faults as major failures in the power systems are studied. The causes and the effects of these faults on power systems are discussed. A brief review on the transient steady analysis of synchronous machines is presented.

This chapter has also discussed implementation of three regression algorithms that have been used in the literature to represent the magnetization characteristics of electrical machines. In this research work, these models have been redeveloped. The results of magnetization characteristics calculated by these models have been compared with those of that calculated by the proposed models. This is discussed in detail in the next chapters.

Chapter 3

Representation of Magnetization Phenomenon in Electrical Machines Using Trigonometric Regression Algorithm

In this chapter a new method to represent all regions of the magnetization characteristics, namely the unsaturated, non-linear and highly saturated regions, with a trigonometric series, as in Fig. 3.1, is developed. The experimentally measured magnetization characteristics data points are used to develop the series in Fig. 3.1. The measured data points for the flux linkages and their corresponding magnetizing currents for different kinds and sizes of electrical machines are fed to the proposed model to generate a series of sinusoidal curves that fit these data points, which represent the magnetization characteristics of the machine. The results are demonstrated in Section 3.2. In addition, the accuracy of the
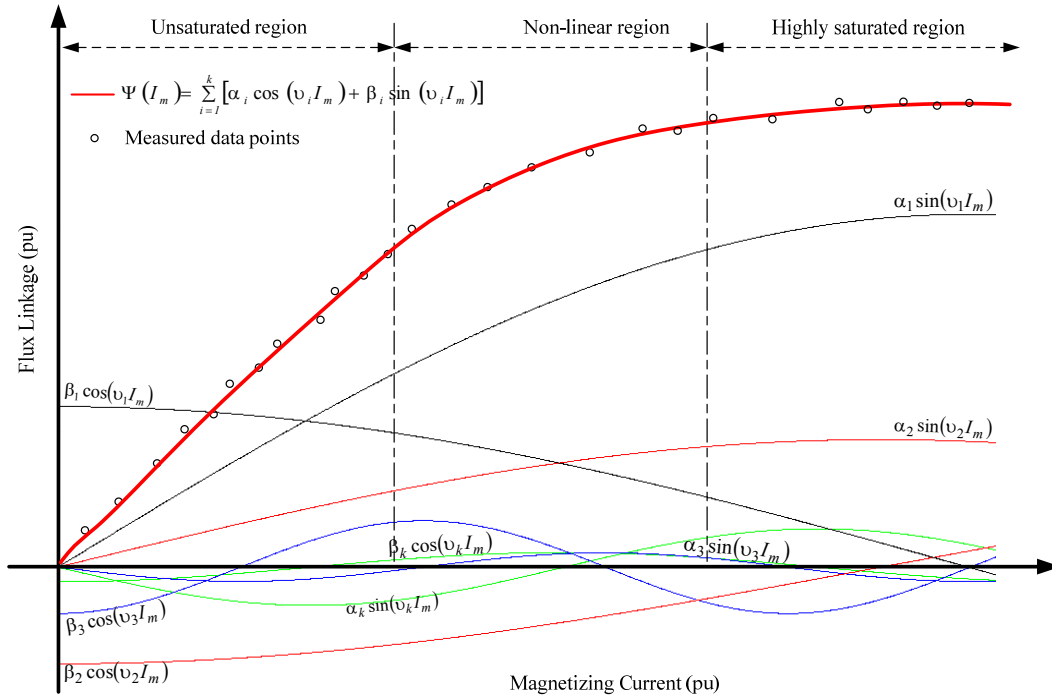
Fig. 3.1. Trigonometric representation of measured data points of the magnetization characteristics of a typical electrical machine.

proposed trigonometric model has been evaluated through error calculation using the Chi-square methods.

3.1. Trigonometric Regression Algorithm

Suppose a set of n data points of magnetizing currents of a typical electrical machine is expressed as I_{m1}, I_{m2}, …, I_{mn}, and the corresponding measured n data points of the flux linkages are expressed as $\Psi(I_{m1})$, $\Psi(I_{m2})$, …, $\Psi(I_{mn})$. The objective of this algorithm is to obtain a trigonometric curve as in (3.1), which predicts the value of the flux linkage for any value of magnetizing current. This can be performed through the determination of the

frequency, amplitude, and phase angle of each sinusoidal term. The developed trigono-
metric function can be expressed as:

$$\Psi(I_m) = \sum_{i=1}^{k} \left[\alpha_i \cos(\upsilon_i I_m) + \beta_i \sin(\upsilon_i I_m) \right] \tag{3.1}$$

where k ($2k < n$) is called the order of the trigonometric series, $(\alpha_i)_{i \in [1:k]}$ and $(\beta_i)_{i \in [1:k]}$ are

the amplitudes and $(\upsilon_i)_{i \in [1:k]}$ is the frequency of each trigonometric term.

The trigonometric regression algorithm is developed in two parts. First, the ampli-
tudes are determined based on minimizing the least square error (LSE) function by con-
straining its gradient to zero. In the second part, the frequencies of the sinusoidal terms
will be calculated. At this stage, the Prony method is applied to the exponential represen-
tation of the curve. To determine the coefficients of this curve, the LSE is minimized and
then the frequencies are calculated. This technique ensures that the data points will be
fitted to the trigonometric curve more accurately [32].

3.1.1.   Amplitude Calculation

Assuming that the frequencies of the sinusoids are known, one can find the ampli-
tudes using the least-square-error method. In the frequency calculation algorithm, which
will be presented in the next section, the LSE method will also be used to minimize the
error in order to obtain a goodness-of-fit. According to the LSE method, the error func-
tion can be written as:

$$\varepsilon(\alpha,\beta)= \sum_{I_m=I_{m1}}^{I_m=I_{mn}} \left[\Psi(I_m)-\Psi(I_{mn})\right]^2 \tag{3.2}$$

By substituting the calculated flux linkage $\Psi(I_m)$ in (3.1) into (3.2), the following error equation can be obtained:

$$\varepsilon(\alpha,\beta)= \sum_{I_m=I_{m1}}^{I_{mn}} \left[\sum_{i=1}^{k}\left[\alpha_i \cos(\upsilon_i I_m)+\beta_i \sin(\upsilon_i I_m)\right]-\Psi(I_{mn})\right]^2. \tag{3.3}$$

In order to obtain a curve that fits the measured data points most accurately, the error function should be minimized over I_{m1}, I_{m2}, …, I_{mn}. In other words, the gradient of the error function at the points α_1, α_2, …, α_k and β_1, β_2, …, β_k should be equal to zero . Therefore

$$\left. \begin{array}{l} \forall \alpha_{i\in[1:k]} \ \dfrac{\partial\varepsilon(\alpha,\beta)}{\partial\alpha_i}=0 \\[3mm] \forall \beta_{i\in[1:k]} \ \dfrac{\partial\varepsilon(\alpha,\beta)}{\partial\beta_i}=0 \end{array} \right\}. \tag{3.4}$$

Using (3.3) and (3.4), the derivatives of the error function with respect to α_i and β_i can be written as:

$$\frac{\partial\varepsilon}{\partial\alpha_i} = 2 \sum_{I_{mi}=I_{m1}}^{I_{mn}} \cos(\upsilon_i I_m) \times \left\{ \sum_{j=1}^{k}\left[\alpha_j \cos(\upsilon_j I_m)\right]+ \sum_{j=1}^{k}\left[\beta_j \sin(\upsilon_j I_m)\right]-\Psi(I_{mi})\right\}=0. \tag{3.5}$$

and

$$\frac{\partial\varepsilon}{\partial\beta_i} = 2 \sum_{I_{mi}=I_{m1}}^{I_{mn}} \sin(\upsilon_i I_m) \times \left\{ \sum_{j=1}^{k}\left[\alpha_j \cos(\upsilon_j I_m)\right]+ \sum_{j=1}^{k}\left[\beta_j \sin(\upsilon_j I_m)\right]-\Psi(I_{mi})\right\}=0. \tag{3.6}$$

To simplify the procedure at this step, change of variables can be considered as in (3.7) and (3.8).

$$
\left.\begin{array}{l}
\text{CoPhy}(\mu) = \displaystyle\sum_{I_m=I_{m1}}^{I_{mn}} \cos(\mu I_m)\Psi(I_m) \\[4mm]
\text{SiPhy}(\mu) = \displaystyle\sum_{I_m=I_{m1}}^{I_{mn}} \sin(\mu I_m)\Psi(I_m)
\end{array}\right\}
\tag{3.7}
$$

and

$$
\left.\begin{array}{l}
\text{CoCo}(\mu,\rho) = \displaystyle\sum_{I_m=I_{m1}}^{I_{mn}} \cos(\mu I_m)\cos(\rho I_m) \\[4mm]
\text{CoSi}(\mu,\rho) = \displaystyle\sum_{I_m=I_{m1}}^{I_{mn}} \cos(\mu I_m)\sin(\rho I_m) \\[4mm]
\text{SiCo}(\mu,\rho) = \displaystyle\sum_{I_m=I_{m1}}^{I_{mn}} \sin(\mu I_m)\cos(\rho I_m) \\[4mm]
\text{SiSi}(\mu,\rho) = \displaystyle\sum_{I_m=I_{m1}}^{I_{mn}} \sin(\mu I_m)\sin(\rho I_m)
\end{array}\right\}.
\tag{3.8}
$$

Consequently, the following equations can be obtained using (3.5)-(3.8):

$$
\sum_{j=1}^{k}\left[\alpha_j\,\text{CoCo}(\upsilon_i,\upsilon_j) + \beta_j\,\text{CoSi}(\upsilon_i,\upsilon_j)\right] = \text{CoPhy}(\upsilon_i)
\tag{3.9}
$$

and

$$
\sum_{j=1}^{k}\left[\alpha_j\,\text{SiCo}(\upsilon_i,\upsilon_j) + \beta_j\,\text{SiSi}(\upsilon_i,\upsilon_j)\right] = \text{SiPhy}(\upsilon_i).
\tag{3.10}
$$

Equations (3.9) and (3.10) can be expressed in a matrix form as in (3.11).

$$M_{(2k\times 2k)} \times \begin{bmatrix} \alpha_1 \\ \vdots \\ \alpha_k \\ \beta_1 \\ \vdots \\ \beta_k \end{bmatrix} = \begin{bmatrix} \text{CoPhy}(\upsilon_1) \\ \vdots \\ \text{CoPhy}(\upsilon_k) \\ \text{SiPhy}(\upsilon_1) \\ \vdots \\ \text{SiPhy}(\upsilon_k) \end{bmatrix} \qquad (3.11)$$

in which, the matric **M** is defined as (3.12).

$$\mathbf{M} = \begin{bmatrix} \text{CoCo}(\upsilon_1,\upsilon_1) & \cdots & \text{CoCo}(\upsilon_1,\upsilon_k) & \text{CoSi}(\upsilon_1,\upsilon_1) & \cdots & \text{CoSi}(\upsilon_1,\upsilon_k) \\ \vdots & \ddots & \vdots & \vdots & \ddots & \vdots \\ \text{CoCo}(\upsilon_k,\upsilon_1) & \cdots & \text{CoCo}(\upsilon_k,\upsilon_k) & \text{CoSi}(\upsilon_k,\upsilon_1) & \cdots & \text{CoSi}(\upsilon_k,\upsilon_k) \\ \text{SiCo}(\upsilon_1,\upsilon_1) & \cdots & \text{SiCo}(\upsilon_1,\upsilon_k) & \text{SiSi}(\upsilon_1,\upsilon_1) & \ddots & \text{SiSi}(\upsilon_1,\upsilon_k) \\ \vdots & \ddots & \vdots & \vdots & \vdots & \vdots \\ \text{SiCo}(\upsilon_k,\upsilon_1) & \cdots & \text{SiCo}(\upsilon_k,\upsilon_k) & \text{SiSi}(\upsilon_k,\upsilon_1) & \cdots & \text{SiSi}(\upsilon_k,\upsilon_k) \end{bmatrix}. (3.12)$$

Consequently, by solving this matrix equation, the amplitudes can be obtained.

$$
\begin{bmatrix} \alpha_1 \\ \vdots \\ \alpha_k \\ \beta_1 \\ \vdots \\ \beta_k \end{bmatrix} = \mathbf{M}^{-1} \times \begin{bmatrix} \mathrm{CoPhy}\left(\upsilon_1\right) \\ \vdots \\ \mathrm{CoPhy}\left(\upsilon_k\right) \\ \mathrm{SiPhy}\left(\upsilon_1\right) \\ \vdots \\ \mathrm{SiPhy}\left(\upsilon_k\right) \end{bmatrix}.
\tag{3.13}
$$

3.1.2.   Frequency Calculation

In this section of the curve fitting algorithm, the Prony method is used to find the frequency of the components [32], [36], [37]. To use this method, first we need to obtain the exponential format of (3.1) which is given in (3.14)

$$
\Psi\left(I_m\right) = \sum_{i=1}^{2k} \left[\delta_i e^{\left(j\upsilon_i I_m\right)} \right].
\tag{3.14}
$$

where δ_i is a complex number and $j^2=-1$. It can be shown that if for each $i \in [0{:}2k]$, δ_p can be found satisfying $\delta_i = \overline{\delta_p}$, (3.14) can be transformed into (3.1).

If $x_i = e^{\left(j\upsilon_i I_m\right)}$ can be considered as the roots of the Prony polynomial $f_P(x)$, it can be expressed

$$
f_P\left(x\right) = \prod_{i=1}^{2k} \left(x - x_i\right) .
\tag{3.15}
$$

(3.15) can be rewritten as:

$$f_P(x) = \sum_{p=0}^{2k} a_p x^{2k-p}, \quad x_i = e^{\left(j \upsilon_i I_m\right)}. \tag{3.16}$$

Substituting the roots in the Prony polynomial, one can have

$$f_P(x_i) = 0 \quad \text{and} \quad f_P\left(\frac{1}{x_i}\right) = 0. \tag{3.17}$$

Consequently, $g_P(x)$ is obtained with the same roots as $f_p(x)$ defined by

$$g_P(x) = \sum_{p=0}^{2k} a_p x^p = 0, \quad x_i = e^{\left(j \upsilon_i I_m\right)}. \tag{3.18}$$

Therefore,

$$g_P(x) = \gamma f_P(x) \Rightarrow a_p = \gamma a_{2k-p} \quad, \quad p \in [0:2k]. \tag{3.19}$$

Considering that $x_i = e^{\left(j \upsilon_i I_m\right)}$ contains two roots in the range of $[0:2k]$, the $f_P(x)$ can be rewritten as

$$f_P(x) = \prod_{i=1}^{k} \left[x^2 - 2\cos(\upsilon_i I_m)x + 1 \right] \tag{3.20}$$

Considering (3.16) and (3.19), from (3.20) one can conclude

$$a_{2k} = a_0 = 1 \text{ and } \gamma = 1 \Rightarrow a_p = a_{2k-p}. \tag{3.21}$$

This conclusion is useful to determine the coefficients $(a_p)_{p \in [0:2k]}$ in (3.16). To achieve this, it is assumed that there are n measured values of flux linkages, such as Ψ_1, Ψ_2, …, Ψ_n. Using (3.14), (3.18), and (3.21), we can obtain (3.22).

$$
\left.
\begin{aligned}
&\left(\Psi_2 + \Psi_{2k}\right)a_1 + \left(\Psi_3 + \Psi_{2k-1}\right)a_2 + \cdots + \left(\Psi_k + \Psi_{k+2}\right)a_{k-1} + \Psi_{k+1}a_k = -\Psi_1 - \Psi_{2k+1} \\
&\left(\Psi_3 + \Psi_{2k+1}\right)a_1 + \left(\Psi_4 + \Psi_{2k}\right)a_2 + \cdots + \left(\Psi_{k+1} + \Psi_{k+3}\right)a_{k-1} + \Psi_{k+2}a_k = -\Psi_2 - \Psi_{2k+2} \\
& \\
&\left(\Psi_{n-2k+1} + \Psi_{n-1}\right)a_1 + \left(\Psi_{n-2k+2} + \Psi_{n-2}\right)a_2 + \cdots + \left(\Psi_{n-k-1} + \Psi_{n-k+1}\right)a_{k-1} + \Psi_{n-k}a_k = -\Psi_{n-2k} - \Psi_n
\end{aligned}
\right\}.
$$

$$(3.22)$$

From (3.22), k number of equations is obtained. However, to find all $2k$ number of coefficients one needs to have $2k$ equations. The next step of the interpolation algorithm is to use the LSE method to get the other k number of equations to calculate a's. The error function can be calculated as follows:

$$
\varepsilon(a_1, \dots a_k) = \sum_{i=1}^{n-2k} \left[a_k \Psi_{i+k} + \sum_{j=0}^{k-1} a_j \left(\Psi_{i+j} + \Psi_{i+2k-j} \right) \right]^2
\tag{3.23}
$$

To minimize the error, the derivative of the error function with respect to the all coefficients of a should be zero. Consequently, for $l \in [1:k\text{-}1]$, (3.24) can be obtained

$$
\frac{\partial \varepsilon}{\partial a_l} = 2 \sum_{i=1}^{n-2k} \left\{ \left(\Psi_{i+l} + \Psi_{i+2k-l} \right) \times \left[a_k \Psi_{i+k} + \sum_{j=0}^{k-1} a_j \left(\Psi_{i+j} + \Psi_{i+2k-j} \right) \right] \right\} = 0
\tag{3.24}
$$

and for $l=k$, we have

$$\frac{\partial \varepsilon}{\partial a_k} = 2 \sum_{i=1}^{n-2k} \left\{ (\Psi_{i+k}) \times \left[a_k \Psi_{i+k} + \sum_{j=0}^{k-1} a_j (\Psi_{i+j} + \Psi_{i+2k-j}) \right] \right\} = 0 \qquad (3.25)$$

Therefore for $l \in [1:k\text{-}1]$, (3.24) can be rewritten as

$$\sum_{i=1}^{n-2k} \left\{ (\Psi_{i+l} + \Psi_{i+2k-l}) \times \left[a_k \Psi_{i+k} + \sum_{j=1}^{k-1} a_j (\Psi_{i+j} + \Psi_{i+2k-j}) \right] \right\} =$$

$$- \sum_{i=1}^{n-2k} \left[(\Psi_{i+l} + \Psi_{i+2k-l}) \times (\Psi_i + \Psi_{i+2k}) \right] \quad (3.26)$$

Similarly for the case of $l=k$, from (3.25), we have

$$\sum_{i=1}^{n-2k} \left\{ (\Psi_{i+k}) \times \left[a_k \Psi_{i+k} + \sum_{j=1}^{k-1} a_j (\Psi_{i+j} + \Psi_{i+2k-j}) \right] \right\} =$$

$$- \sum_{i=1}^{n-2k} \left[(\Psi_{i+k}) \times (\Psi_{i+j} + \Psi_{i+2k-j}) \right] \qquad (3.27)$$

Further, a matrix equation can be extracted using (3.26) and (3.27), which will result in the coefficients a_i as in (3.28)

$$\begin{bmatrix} a_1 \\ \vdots \\ a_{k-1} \\ a_k \end{bmatrix} = \mathbf{M}^{-1} \times \begin{bmatrix} - \sum_{i=1}^{n-2k} \left[(\Psi_{i+1} + \Psi_{i+2k-1}) \times (\Psi_i + \Psi_{i+2k}) \right] \\ \vdots \\ - \sum_{i=1}^{n-2k} \left[(\Psi_{i+k-1} + \Psi_{i+k+1}) \times (\Psi_i + \Psi_{i+2k}) \right] \\ - \sum_{i=1}^{n-2k} \left[(\Psi_{i+k}) \times (\Psi_{i+j} + \Psi_{i+2k-j}) \right] \end{bmatrix}. \qquad (3.28)$$

In which matrix $\mathbf{M}$ can be defined by (3.29)

$$\mathbf{M}(m,n) = \begin{cases} \sum_{i=1}^{n-2k} \left[\left(\Psi_{i+m} + \Psi_{i+2k-m} \right)\left(\Psi_{i+n} + \Psi_{i+2k-n} \right) \right] & \text{for } m,n \leq k-1 \\ \\ \sum_{i=1}^{n-2k} \Psi_{i+k} \times \left(\Psi_{i+m} + \Psi_{i+2k-m} \right) & \text{for } m \leq k-1 \,\&\, n = k \\ \\ \sum_{i=1}^{n-2k} \Psi_{i+k} \times \left(\Psi_{i+n} + \Psi_{i+2k-n} \right) & \text{for } n \leq k-1 \,\&\, m = k \end{cases} \qquad (3.29)$$

After determining the coefficients, the next step is to find the frequencies in (3.16). It can be shown that

$$f_P(x) = x^k \left[\sum_{p=0}^{m-1} a_p \left(x^{k-p} + \frac{1}{x^{k-p}} \right) + a_k \right]. \qquad (3.30)$$

Let us consider,

$$x^{k-p} + \frac{1}{x^{k-p}} = 2\cos(k-p)\theta \ . \qquad (3.31)$$

Instead of solving (3.31), (3.32) can be solved.

$$\sum_{i=0}^{k-1} \left\{ 2a_i \cos\left[(k-i)\theta \right] \right\} + a_k = 0. \qquad (3.32)$$

Since coefficients a_i are specified in the previous stage, (3.33) is a cosine equation with an unknown angle θ. To solve this equation, it can be rewritten using Chebyshev polynomials defined by the following recurrence relation.

$$
\left.
\begin{aligned}
&T_0(x) = 1 \\[4pt]
&T_1(x) = x \\[4pt]
&T_2(x) = 2x^2 - 1 \\[4pt]
&T_3(x) = 4x^3 - 3x \\
&\vdots \\
&T_{n+1}(x) = 2xT_n(x) - T_{n-1}(x)
\end{aligned}
\right\}.
\tag{3.33}
$$

Replacing x with $\cos\theta$ in (3.34) and considering (3.33), (3.34) is obtained

$$
\Psi(I_m) = \sum_{i=0}^{k-1} 2a_i T_{k-i} \cos\theta + a_k .
\tag{3.34}
$$

After replacing the coefficient and recursive equivalents, one can get a mono-variable polynomial of order k for $X = \cos\theta$. Solving this equation allows us to find $p \in [1{:}k]$ roots for X. As a result, frequencies can be obtained by using

$$
\upsilon_p = \cos^{-1}\left[X_p\right].
\tag{3.35}
$$

3.2. Numerical Analysis Employing the DFT and Trigonometric Algorithms in the Cases of Synchronous and Doubly-fed Induction Machines

A new trigonometric model to fit the measured magnetization characteristics data points of electrical machines has been presented in the previous section. In this section, numerical investigations are carried out to validate the performance of the developed

model. This magnetization model has been applied to three machines of different sizes and ratings. The 555 MVA Lambton and 588 MVA Nanticoke synchronous machines [38]- [40], both from Ontario Hydro System in Canada, and a laboratory 3-phase, 2.78 kVA doubly-fed induction machine [40] have been used in the investigations to validate the performance of the proposed magnetization model. Machine ratings and specifications are presented in Appendix A. To compare the accuracy of the proposed trigonometric algorithm, the DFT method of interpolation described in Chapter 2, has also been applied to all three machines. For all cases under investigation, the error tests are carried out at the highest order of the trigonometric model and their equivalent DFT model to compare the goodness-of-fit.

3.2.1.   *Measured and Calculated Main and Leakage Flux Magnetization Characteristics of the DFIG*

Wound-rotor induction generators have numerous advantages in the area of wind power generation in comparison to other types of generators. A notable scheme is the use of a cascade converter between the slip-ring terminals and the utility grid to control the rotor power. This configuration is known as the doubly-fed induction generator (DFIG). Fig. 3.2 shows the DFIG used in the experimental investigations of this chapter. The 2.78 kVA DFIG is coupled to a prime-mover (DC motor). The rated stator and rotor currents of the DFIG are 9 A and 4.5 A, respectively. The voltage, current, and real and reactive power of the DFIG were measured using the Lab-Volt measuring devices integrated with

Fig. 3.2. The doubly-fed induction generator (DFIG) under the investigations.

the experimental system. Tests were performed on the DFIG to obtain the main flux magnetization characteristics, as well as the stator and rotor leakage flux magnetization characteristics.

In order to acquire the main flux magnetization characteristics of the DFIG, as shown in Fig. 3.2, the no-load generator test at synchronous speed is carried out. In the no-load generator test, the machine is supplied by a three-phase controllable amplitude power source at the rated frequency and driven at the synchronous speed. The amplitude of the voltage source is adjusted while the terminal current and the active power are continuously measured. It should be noted that the magnetizing current is equivalent to the stator current, in view of the fact that the rotor current is zero, as the machine is driven at syn-

chronous speed. The main flux magnetization characteristics can be obtained by plotting the terminal voltage as a function of the stator current, as shown in Fig. 3.3. This figure also shows the results of the calculated main flux magnetization characteristics for three orders (k=3, 4, and 5) of trigonometric series. It can be seen that the calculated results are in good agreement with the measured ones. The trigonometric series function in the 5th order consists of five sine and five cosine terms which are equivalent to the DFT function of order 10. Based on the number of data points, the degree of the fitted curve is defined. As seen in Fig. 3.3, the accuracy of the fitted magnetization characteristics increases with higher orders of the trigonometric series. Figs. 3.4 and 3.5 present the measured and fitted curves for the rotor and stator leakage flux magnetization characteristics of the DFIG respectively. The terminal voltage–armature current curve with the machine unloaded and unexcited, and the open-circuit characteristics are determined twice; one on the stator and another on the rotor. Evidently, the most accurate curve is obtained for the 5th order trigonometric series. The DFT curve fitted for an order of 10 has been shown in these figures as well. The coefficient of the trigonometric series along with the frequency values for the fifth order for all magnetization characteristics of the DFIG are presented in Table 3.1.
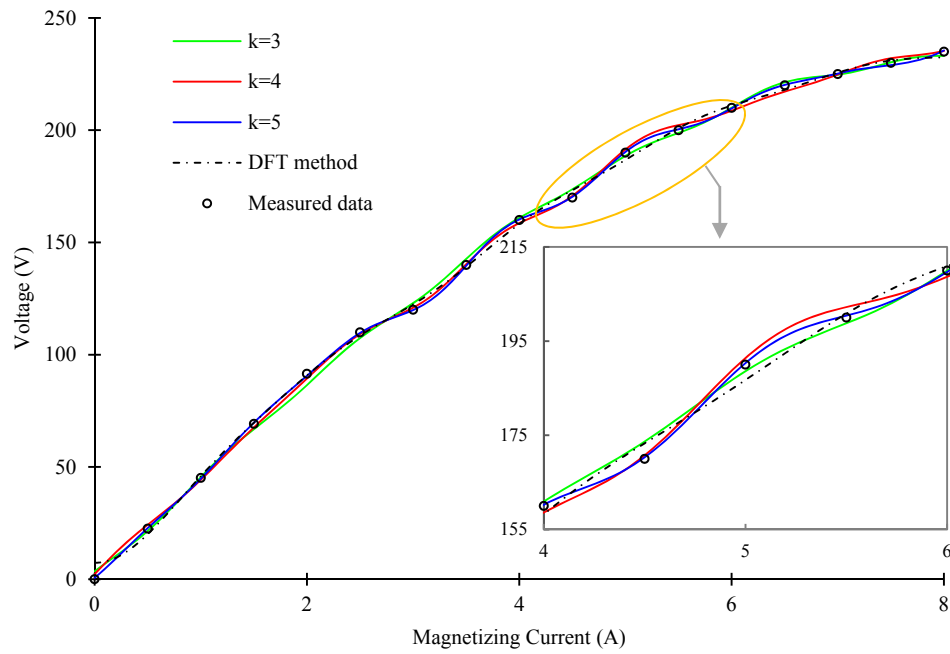
Fig. 3.3. Calculated and measured main flux magnetization characteristics of the DFIG for three orders of trigonometric series and for DFT curve fitting method of order 10.
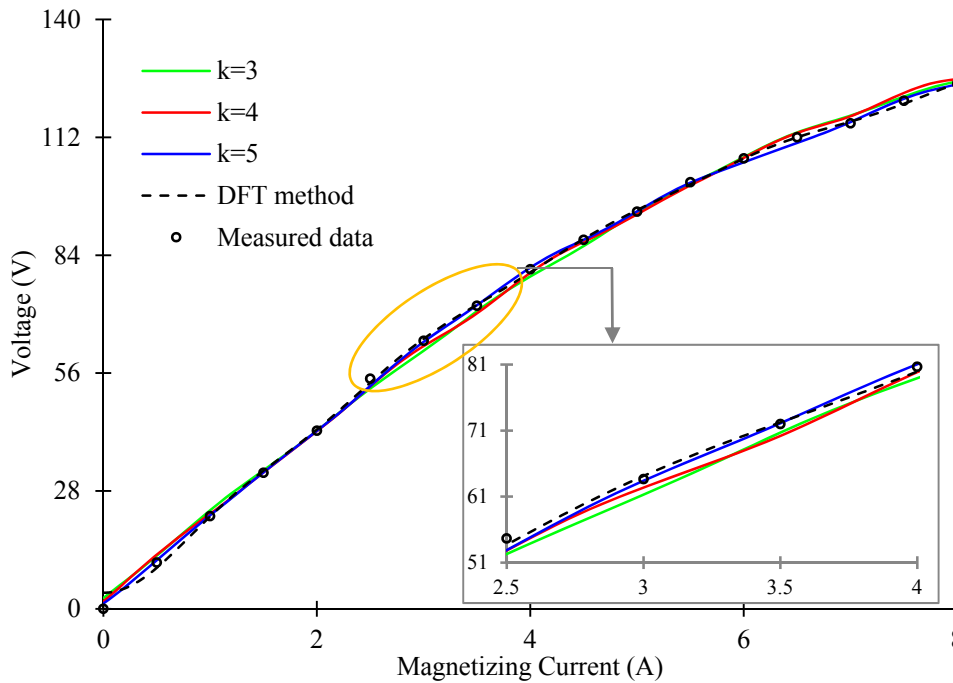
Fig. 3.4. Calculated and measured rotor leakage flux magnetization characteristics of the DFIG for three orders of trigonometric series and for DFT curve fitting method of order 10.
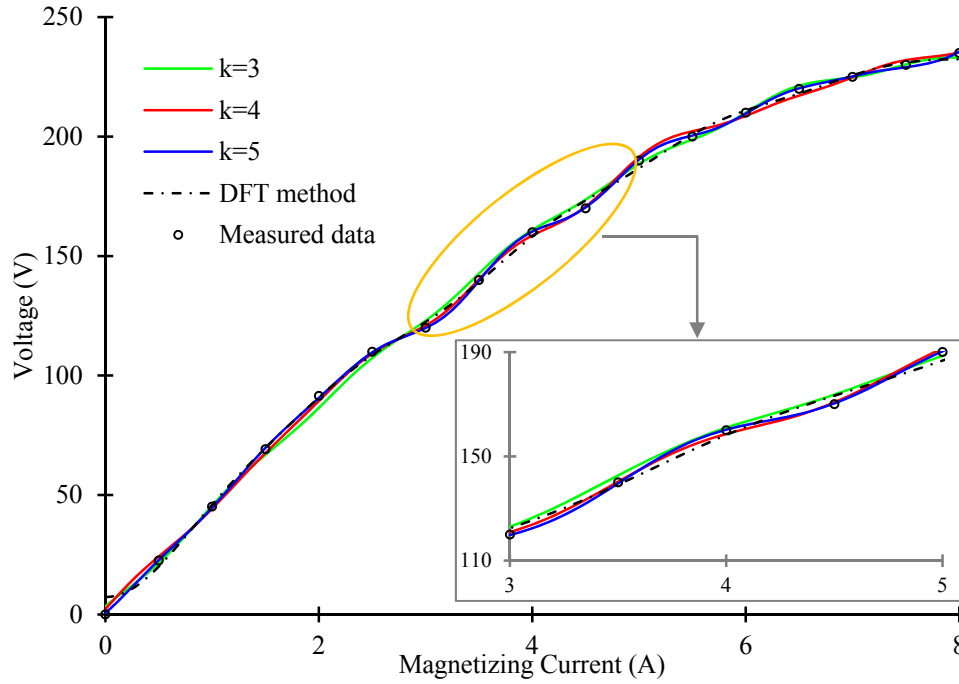
Fig. 3.5. Calculated and measured stator leakage flux magnetization characteristics of the DFIG for three orders of trigonometric series and for DFT curve fitting method of order 10.

3.2.2. *Calculated d- and q-axis Magnetization Characteristics of the Nanticoke and Lambton Synchronous Machines*

To demonstrate the effectiveness of the developed trigonometric magnetization model, it has also been applied to two large synchronous generators [41]. The d-axis magnetization characteristics of synchronous machines can be easily determined by conducting the conventional open-circuit test, whereas there are no simple methods to determine the q-axis magnetization characteristics. In [42], [43], several methods have been proposed to calculate the q-axis magnetization characteristics from the measured d-axis characteristics. It has been demonstrated in [41] that steady-state, on-load measurements at the ter-

minals of synchronous generators can be used to determine both d- and q-axis magnetization characteristics.

The proposed algorithm has been applied to fit both d- and q-axis magnetization characteristics of the Nanticoke and Lambton synchronous machines. Figs. 3.6 and 3.7 illustrate the calculated results for two orders of trigonometric functions in the case of both d- and q-axis magnetization characteristics. Although the limited number of data points has created a limited trigonometric series of order 1 and 2, the calculated characteristics fit the measured magnetization characteristics data points very well. To compare the results for the most accurate trigonometric curve, the d- and q-axis magnetization characteristics for the Nanticoke and Lambton machines are represented by its equivalent DFT interpolation model with the order of 4. These graphs for the Nanticoke and Lambton synchronous machines are shown in Figs. 3.6 and 3.7, respectively. The amplitudes and the frequencies of the trigonometric terms of the fitted curves for the second-order series have been presented in Table 3.1.
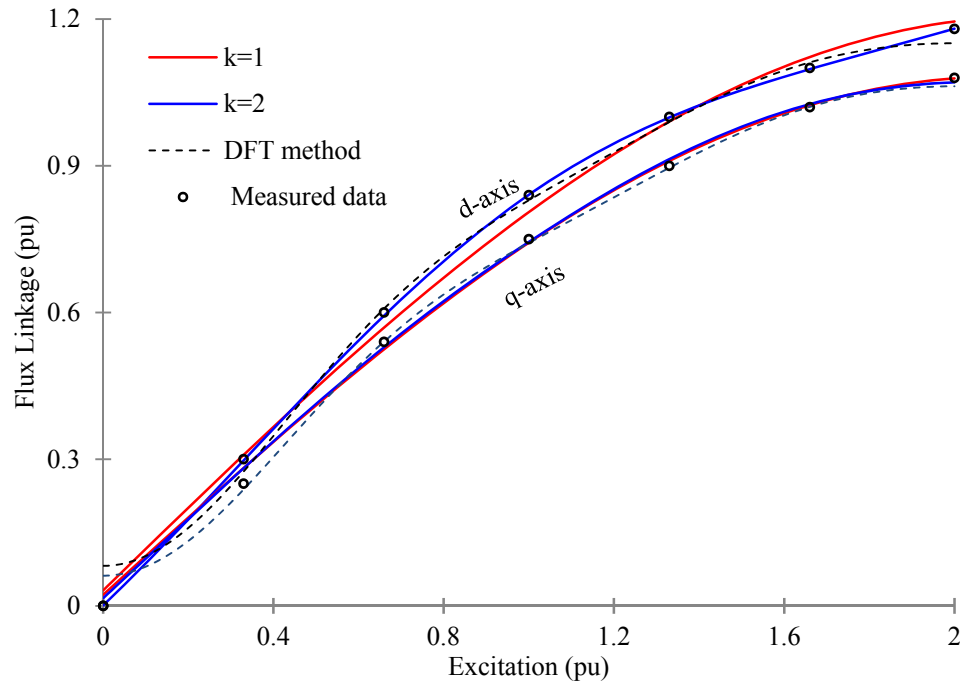
Fig. 3.6. d- and q-axis magnetization characteristics of the Nanticocke synchronous machine presented by the proposed model for two orders of trigonometric series and the 4th order of DFT model.
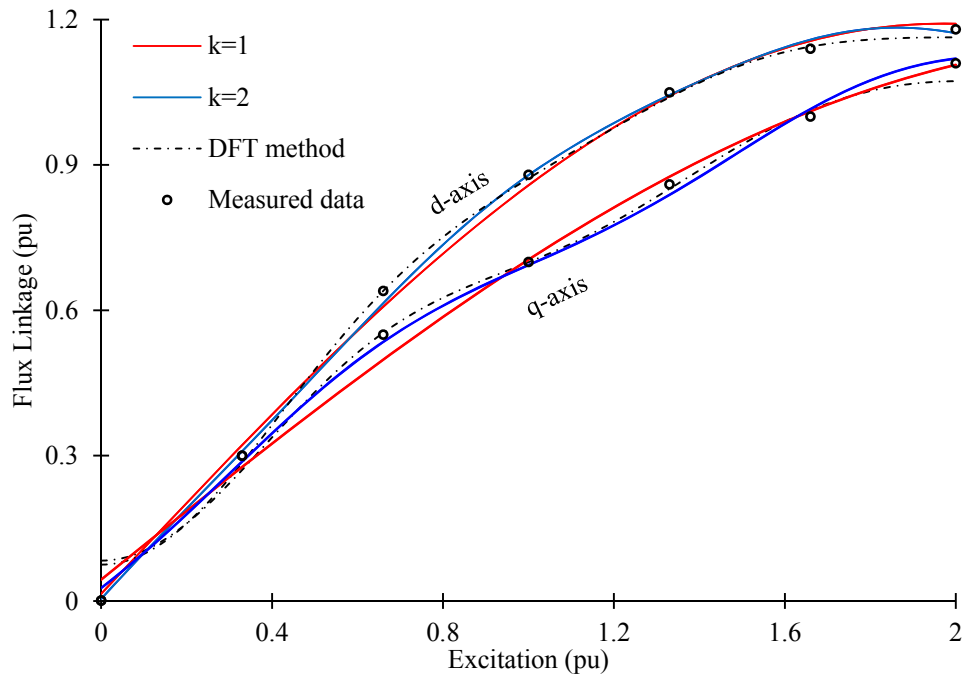
Fig. 3.7. d- and q-axis magnetization characteristics of the Lambton synchronous machine presented by the proposed model for two orders of trigonometric series and the 4th order of DFT model.

Table 3.1. Frequencies and Amplitudes of the Calculated Magnetization Characteristics

for the Machines under the Investigations

Machine	Frequency	Amplitudes	
DFIG Main flux (*k*=5)	υ_1=2.65911	α_1=-0.16815	β_1=1.66295
	υ_2=2.09038	α_2= -2.17409	β_2= -0.28981
	υ_3=1.26317	α_3= -1.54375	β_3= -1.79594
	υ_4=1.00365	α_4= -0.98576	β_4= -3.12139
	υ_5=0.0874	α_5= 5.47566	β_5= 239.12971
DFIG Stator leakage flux (*k*=5)	υ_1= 2.67513	α_1= -0.24535	β_1= 0.02963
	υ_2= 2.03247	α_2= -0.10778	β_2= -0.28206
	υ_3= 1.43226	α_3= -0.34183	β_3= -0.10537
	υ_4= 0.51761	α_4= -1.31250	β_4= -1.23969
	υ_5= 0.07721	α_5= 3.28831	β_5= 131.63648
DFIG Rotor leakage flux (*k*=5)	υ_1= 2.75333	α_1= 0.06088	β_1= -0.27814
	υ_2= 2.05865	α_2= 0.03472	β_2= -0.55034
	υ_3=1.43698	α_3= 0.26290	β_3= - 0.10446
	υ_4=0.66569	α_4= 0.12613	β_4= -0.61001
	υ_5=0.08271	α_5= 1.03526	β_5= 122.3211
Nanticoke d-axis (*k*=2)	υ_1= 1.00274	α_1= -0.05186	β_1= 0.01649
	υ_2= 0.20430	α_2= 0.05298	β_2= 1.29305
Nanticoke q-axis (*k*=2)	υ_1= 2.0743	α_1= -0.00230	β_1= -0.00088
	υ_2= 0.25045	α_2= 0.01827	β_2= 1.07412
Lambton d-axis (*k*=2)	υ_1= 2.21596	α_1= 0.00918	β_1= -0.00322
	υ_2= 0.28025	α_2= -0.00482	β_2= 1.17387
Lambton q-axis (*k*=2)	υ_1= 1.68770	α_1= -0.03299	β_1= -0.00209
	υ_2= 0.20301	α_2= 0.05971	β_2= -1.14265

3.3. Chi-Square Tests to Measure the Accuracy of the Proposed Magnetization Model

Reduced Chi-square[32] technique has been applied to measure the accuracy of the proposed model. The value of the Chi-square error can be calculated using the following equation:

$$\chi^2 = \sum_{i=1}^{n} \frac{\left[\Psi(I_{mi}) - \Psi_i\right]^2}{\Psi_i} \tag{3.36}$$

where $\Psi(I_{mi})$ are the calculated values by the proposed model at different excitation currents, $I_{m1}, I_{m2}, \ldots, I_{mn}$, whereas $\Psi_1, \Psi_2, \ldots, \Psi_n$ are the actual measured data points at those excitation currents.

The goodness of fit for the magnetization characteristics has also been examined by the statistic chi-square method, which has been applied to both the DFT and the proposed trigonometric interpolation models. This method can be expressed by

$$\chi^2 = \sum_{i=1}^{n} \frac{\left[\Psi(I_{mi}) - \Psi_i\right]^2}{\sigma^2} \tag{3.37}$$

where σ^2 is the known variance of the measured data points.

The calculated Chi-square error tests for different machines on trigonometric curve fitting model of three orders, as well as the corresponding results for DFT interpolation model, are presented in Table 3.2. The results demonstrate the effectiveness of the proposed method in fitting the magnetization characteristics data points of electric machines

of different types and sizes. Evidently, the proposed trigonometric curve fitting for all the

cases is more accurate than the DFT regression method.

Table 3.2. Comparison of Chi-Square Error Test for Different Trigonometric Orders and Their Correspond-
ing DFT Orders for the Machines Used in the Investigations.

| Machine | Magnetization Characteristics | Trigonometric Method | | | DFT Method | | |
		Trigonometric Order	Chi-Square Error	Chi-Square Distribution	DFT Order	Chi-Square Error	Chi-Square Distribution
Doubly-fed Induction Generator (DFIG)	Main flux	3	0.72222	0.01181	6	1.08227	0.02215
		4	0.35989	0.00536	8	0.94831	0.01849
		5	0.02823	0.00048	10	0.81219	0.01426
	Stator leakage flux	3	0.37504	0.01655	6	1.11219	0.02662
		4	0.30797	0.01263	8	1.04831	0.01624
		5	0.08422	0.00438	10	0.68227	0.01023
	Rotor leakage flux	3	0.66905	0.01665	6	1.30318	0.02678
		4	0.56622	0.01270	8	0.95893	0.01634
		5	0.12520	0.00441	10	0.49096	0.01029
Nanticoke Synchronous Machine	d-axis	1	0.00401	0.01115	2	0.03308	0.08857
		2	0.00010	0.00016	4	0.01353	0.02363
	q-axis	1	0.00471	0.11341	2	0.03169	0.2139
		2	0.00457	0.11211	4	0.01098	0.14620
Lambton Synchronous Machine	d-axis	1	0.00421	0.00728	2	0.07077	0.09546
		2	0.00151	0.00324	4	0.05121	0.03337
	q-axis	1	3.8×10^{-7}	0.01540	2	0.07478	0.28684
		2	1.1×10^{-5}	0.00530	4	0.02478	0.19960

3.4. Conclusion

A trigonometric algorithm has been developed in this chapter to represent the magnetization characteristics of electrical machines. The suitability of using this model in estimating the magnetization characteristics of electrical machines out of some measured data points from experimental tests has been investigated. The results of applying this model to different types of electrical machines such as induction or synchronous machines in various ranges of size, from mid-size to large size machines, evaluate the model as a precise and reliable one, which can be used in any kind of machine models.

The work developed in this chapter has already been presented in IEEE International Conference on Electrical Machines (ICEM), 2010 [44]. The more comprehensive paper based on the presented work has been published in IEEE Transactions on Energy Conversion [45].

Chapter 4

Multifunctional Characterization of Magnetization Phenomenon Using Levenberg-Marquardt Optimization Algorithm

In the previous chapter, a new method to represent the magnetization in electrical machines in the form of sine and cosine terms was presented. Through the several investigations the accuracy and reliability of this method was examined.

In this chapter, the main objective is to develop another regression algorithm based on the Levenberg-Marquardt (LM) method that can be used to represent the flux linkage and magnetizing current relationship with several configurations in a specific domain of applicability. This concept is demonstrated in Fig. 4.1.
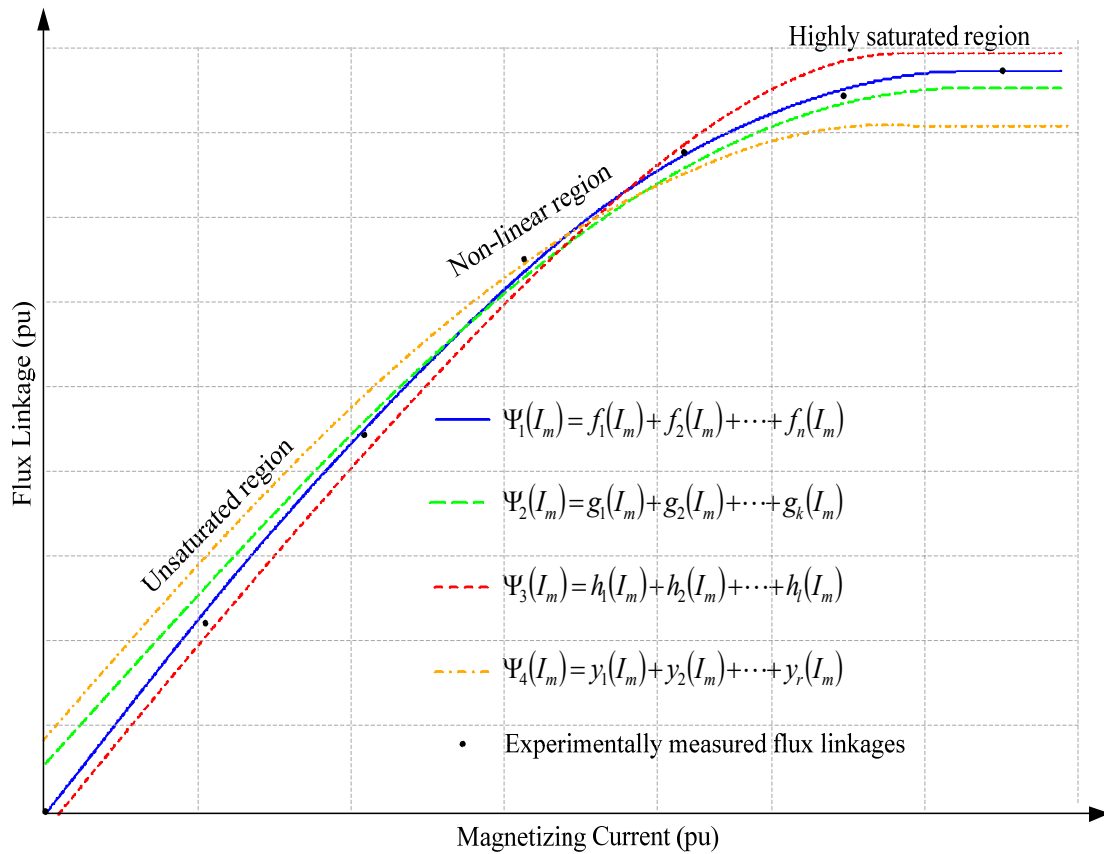
Fig. 4.1. Different configurations to represent magnetization characteristics of a typical electrical machine.

The main distinguishable merit of this method is that this algorithm produces several real functional definitions for magnetization phenomenon with an acceptable level of accuracy. This model has also been verified by comparing the results on different magnetization phenomenon configurations provided by the proposed method in this chapter and some existing methods mentioned in Chapters 2 and the trigonometric method described in Chapter 3. The calculated results presented in Section 4.2 of this chapter show that this model can be used as an alternative for aforementioned methods.

4.1. Levenberg-Marquardt Algorithm

In this study, a non-linear optimization method, namely, the Levenberg-Marquardt (LM) algorithm [46]- [49], is used to represent the machine magnetization characteristics for a set of given experimental data points. The advantage of applying this technique is that the magnetization characteristics of the synchronous machine can be represented by a series of non-linear multi-variable functions. It should be noted that the coefficients might also have different dimensions.

Suppose that a set of experimentally obtained magnetization data points is expressed as (4.1)

$$\hat{\mathbf{X}} = \begin{bmatrix} \hat{\mathbf{\Psi}} & \hat{\mathbf{I}} \end{bmatrix} \tag{4.1}$$

where $\hat{\mathbf{I}}$ is the measured magnetizing current data point matrix and $\hat{\mathbf{\Psi}}$ is its corresponding measured flux data point matrix such as in (4.2)

$$\hat{\mathbf{\Psi}} = \begin{bmatrix} \hat{\Psi}_1 \\ \hat{\Psi}_2 \\ \vdots \\ \hat{\Psi}_n \end{bmatrix} \quad \text{and} \quad \hat{\mathbf{I}} = \begin{bmatrix} \hat{I}_{m1} \\ \hat{I}_{m2} \\ \vdots \\ \hat{I}_{mn} \end{bmatrix}. \tag{4.2}$$

To fit the function $\Psi(I_m)$, to the data points in (4.2), the LM algorithm starts by using the chi-square error criteria to minimize the sum of the weighted squares of the errors between the measured data $\hat{\Psi}(\hat{I}_{mi})$, and $\Psi(\hat{I}_{mi})$.

$$\chi^2 = \sum_{i=1}^{n} \left[\frac{\hat{\Psi}\left(\hat{I}_{mi}\right) - \Psi\left(\hat{I}_{mi}\right)}{\sigma_i} \right]^2 . \tag{4.3}$$

Suppose $\hat{\Psi}$ consists of non-linear functions and coefficients as $a_1, a_2, \ldots, a_m$, then the general procedure is to determine these coefficients to satisfy (4.4).

$$\frac{\partial \chi^2}{\partial a_1} = \frac{\partial \chi^2}{\partial a_2} = \cdots = \frac{\partial \chi^2}{\partial a_m} = 0. \tag{4.4}$$

Since $\hat{\Psi}$ is a non-linear function, the equations in (4.4) are also non-linear. In this technique, an iterative procedure is used to evaluate (4.4). Similar to any iterative algorithm, an initial guess is required to start the procedure. Through the iterations, the optimum response can be found. The initial guess can be defined by

$$\mathbf{A}_0 = \begin{bmatrix} a_{01} & a_{02} \cdots a_{0m} \end{bmatrix}. \tag{4.5}$$

Next, the chi-square function is minimized. Using Taylor's theorem, the expansion can be written as (4.6).

$$\chi^2\left(a_{1j}\right) = \chi^2\left(a_{0j}\right) + \left(a_{0j} - a_{1j}\right)\frac{\partial \chi^2\left(a_{0j}\right)}{\partial a_{0j}} + \frac{\left(a_{0j} - a_{1j}\right)^2}{2!} \frac{\partial^2 \chi^2\left(a_{0j}\right)}{\partial a_{0j}^2} + \cdots . \tag{4.6}$$

Equation (4.6) can also be written in matrix form

$$\chi^2\left(\mathbf{A}_1\right) = \chi^2\left(\mathbf{A}_0\right) + \Delta a_j \frac{\partial \chi^2\left(\mathbf{A}_0\right)}{\partial a_{1j}} + \frac{\left(\Delta a_{1j}\right)^2}{2!} \frac{\partial^2 \chi^2\left(\mathbf{A}_0\right)}{\partial a_{1j}^2} + \cdots \tag{4.7}$$

where

$$\Delta a_j = \left(a_{0j} - a_{1j}\right) \tag{4.8}$$

$$\chi^2(\mathbf{A}_1) = \begin{bmatrix} \chi^2(a_{11}) \\ \chi^2(a_{12}) \\ \vdots \\ \chi^2(a_{1j}) \\ \vdots \\ \chi^2(a_{1m}) \end{bmatrix} \tag{4.9}$$

$$\chi^2(\mathbf{A}_0) = \begin{bmatrix} \chi^2(a_{01}) \\ \chi^2(a_{02}) \\ \vdots \\ \chi^2(a_{0j}) \\ \vdots \\ \chi^2(a_{0m}) \end{bmatrix} \tag{4.10}$$

$$\Delta a_j \frac{\partial \chi^2(\mathbf{A}_0)}{\partial a_{1j}} = \begin{bmatrix} \Delta a_j \dfrac{\partial \chi^2(a_{01})}{\partial a_{1j}} \\ \Delta a_j \dfrac{\partial \chi^2(a_{02})}{\partial a_{1j}} \\ \vdots \\ \Delta a_j \dfrac{\partial \chi^2(a_{0m})}{\partial a_{1j}} \end{bmatrix} \tag{4.11}$$

and

$$\left(\Delta a_j\right)^2 \frac{\partial^2 \chi^2(\mathbf{A_0})}{\partial a_{1j}^2} = \begin{bmatrix} \left(\Delta a_j\right)^2 \dfrac{\partial^2 \chi^2(a_{01})}{\partial a_{1j}^2} \\ \left(\Delta a_j\right)^2 \dfrac{\partial^2 \chi^2(a_{02})}{\partial a_{1j}^2} \\ \vdots \\ \left(\Delta a_j\right)^2 \dfrac{\partial^2 \chi^2(a_{0m})}{\partial a_{1j}^2} \end{bmatrix}. \tag{4.12}$$

Now let $\nabla\chi^2$ and $\nabla^2\chi^2$ denote the gradient vector of χ^2 and the Hessian matrix of χ^2, respectively, as in (4.13)

$$\left. \begin{aligned} \left(\nabla\chi^2\right)_k &= \frac{\partial \chi^2}{\partial a_k} \\ \left(\nabla^2\chi\right)_{ij} &= \frac{\partial^2 \chi^2}{\partial a_i \partial a_j} \end{aligned} \right\}. \tag{4.13}$$

Therefore, the Taylor series expansion in (4.7) can be reformulated as

$$\chi^2(\mathbf{A_1}) = \chi^2(\mathbf{A_0}) + \nabla\chi^2\Delta\mathbf{A} + \frac{1}{2!}\Delta\mathbf{A}\nabla^2\chi^2\Delta\mathbf{A} \tag{4.14}$$

in which $\Delta\mathbf{A} = \mathbf{A_0} - \mathbf{A_1}$. If the new value of $\mathbf{A_1}$ minimizes χ^2, then, the derivative of the chi-square value in (4.14) will be zero, and (4.15) can be obtained as

$$\nabla\chi^2 + \Delta\mathbf{A}\nabla^2\chi^2 = 0. \tag{4.15}$$

Therefore,

$$\mathbf{A}_1 = \mathbf{A}_0 - \left(\nabla^2\chi^2\right)^{-1}\nabla\chi^2. \tag{4.16}$$

From (4.16), one can conclude that once the gradient and Hessian matrices are calculated, the new matrix, $\mathbf{A_1}$, can then be determined. Note that for simplicity in (4.14), the expansion is expressed only up to its second-degree of Taylor series expansion. Due to this approximation, the new values obtained for $\mathbf{A_1}$ cannot be the minimized values. Consequently, the iterative procedure must be followed again by using the elements in $\mathbf{A_1}$ as the new guesses for the next iteration in the procedure.

The next step is to find the values for the gradient and Hessian matrices. Considering (4.3), one can write

$$\left(\nabla\chi^2\right)_k = -2\sum_{i=1}^{n}\left[\frac{\hat{\Psi}\left(\hat{I}_{mi}\right)-\Psi\left(\hat{I}_{mi}\right)}{\sigma_i^2}\frac{\partial\Psi\left(\hat{I}_{mi}\right)}{\partial a_k}\right] \tag{4.17}$$

and

$$\left(\nabla^2\chi^2\right)_{kj} = -2\sum_{i=1}^{n}\left[\frac{\hat{\Psi}\left(\hat{I}_{mi}\right)-\Psi\left(\hat{I}_{mi}\right)}{\sigma_i^2}\frac{\partial^2\Psi\left(\hat{I}_{mi}\right)}{\partial a_k\partial a_j}\right] + 2\sum_{i=1}^{n}\left[\frac{1}{\sigma_i^2}\frac{\partial\Psi\left(\hat{I}_{mi}\right)}{\partial a_k}\frac{\partial\Psi\left(\hat{I}_{mi}\right)}{\partial a_j}\right]. \tag{4.18}$$

Since the first term in (4.18) is difficult to calculate, another estimation is made to simplify the calculations. This approximation does not affect the accuracy of the procedure because through the algorithm we try to make $\nabla\chi^2 = 0$.

Therefore, considering $\sigma_i = 1$, (4.19) can be obtained

$$\left(\nabla^2\chi^2\right)_{kj} \approx 2\sum_{i=1}^{n}\left[\frac{\partial\Psi\left(\hat{I}_{mi}\right)}{\partial a_k}\frac{\partial\Psi\left(\hat{I}_{mi}\right)}{\partial a_j}\right]. \tag{4.19}$$

On account of the fact that the initial guess at the first step of the algorithm might be chosen far from the optimal location, the process might not be convergent. Therefore, similar to other iteration algorithms, it is essential to develop a technique to control the algorithm to be convergent at the optimum values. To control the direction of searching for the initial guess and the length of the steps in the proposed algorithm, a positive damping factor λ is introduced as in (4.20).

$$\left.\begin{aligned}\left(\nabla^2\chi^2\right)_{jj} &= \left(\nabla^2\chi^2\right)_{jj}\times\left(1+\lambda\right)\\ \left(\nabla^2\chi^2\right)_{ij} &= \left(\nabla^2\chi^2\right)_{ji}\ ,\ (i\neq j)\end{aligned}\right\}. \tag{4.20}$$

(4.20) can be reformulated in a matrix format as in (4.21)

$$\left(\nabla^2\chi^2\right)_{\text{new}} = \left(\nabla^2\chi^2\right)_{\text{old}} + \lambda\mathbf{I}. \tag{4.21}$$

The search direction control procedure comprises two categories based on the value λ. For small values of λ we have

$$\left(\nabla^2\chi^2\right)_{\text{new}} \cong \left(\nabla^2\chi^2\right)_{\text{old}}. \tag{4.22}$$

Therefore, the algorithm follows the Gauss-Newton algorithm descent direction condition [47]. By definition, a vector $\mathbf{d}\in R$ is a descent direction for the function $\chi^2(x)$ at x, if it satisfies

$$\left(\nabla\chi^2\right)^{\mathbf{T}}\mathbf{d} < 0. \tag{4.23}$$

Considering $\mathbf{d}=\Delta\mathbf{A}$ in (4.15), we have

$$\mathbf{d} = -\left(\nabla^2\chi^2\right)^{-1}\nabla\chi^2. \tag{4.24}$$

Substituting (4.24) in (4.23) yields

$$-\left(\nabla\chi^2\right)^{T}\left(\nabla^2\chi^2\right)^{-1}\left(\nabla\chi^2\right) < 0. \tag{4.25}$$

Since $\nabla\chi^2$ is a positive definite matrix, the condition in (4.25) is valid and the search is going to be close to the convergence boundaries. Accordingly, to make the search direction move faster toward the convergence area, at the next step of the iteration, λ must be adjusted to a smaller value.

Furthermore, for large values of λ, (4.21) can be written as

$$\left(\nabla^2\chi^2\right)_{\text{new}} \cong \lambda\mathbf{I}. \tag{4.26}$$

The search direction can be defined by

$$\mathbf{d} = -\left\{\left(\nabla^2\chi^2\right)_{\text{old}} + \lambda\mathbf{I}\right\}^{-1}\left(\nabla\chi^2\right) = -\left(\nabla^2\chi^2\right)_{\text{new}}^{-1}\left(\nabla\chi^2\right) = -\left(\frac{1}{\lambda}\right)\mathbf{I}^{-1}\left(\nabla\chi^2\right) \tag{4.27}$$

Therefore, for large values of λ, the search approximately takes the gradient direction. From (4.27), it can be concluded that by decreasing λ from a large value to small value, the search follows the gradient direction to the Gauss-Newton direction.

In general, the damping factor should be adjusted at every iteration. The search starts with $\lambda=1$. If the initial guess of the algorithm is convergent, then λ will be decreased by a factor of 10 in the next step. Otherwise, λ will be increased by a factor of 10. The algorithm ends when the gradient vector of χ^2 is less than the convergence criterion set at the beginning of the procedure. Fig. 4.2 summarizes the procedure into a flowchart of the algorithm.
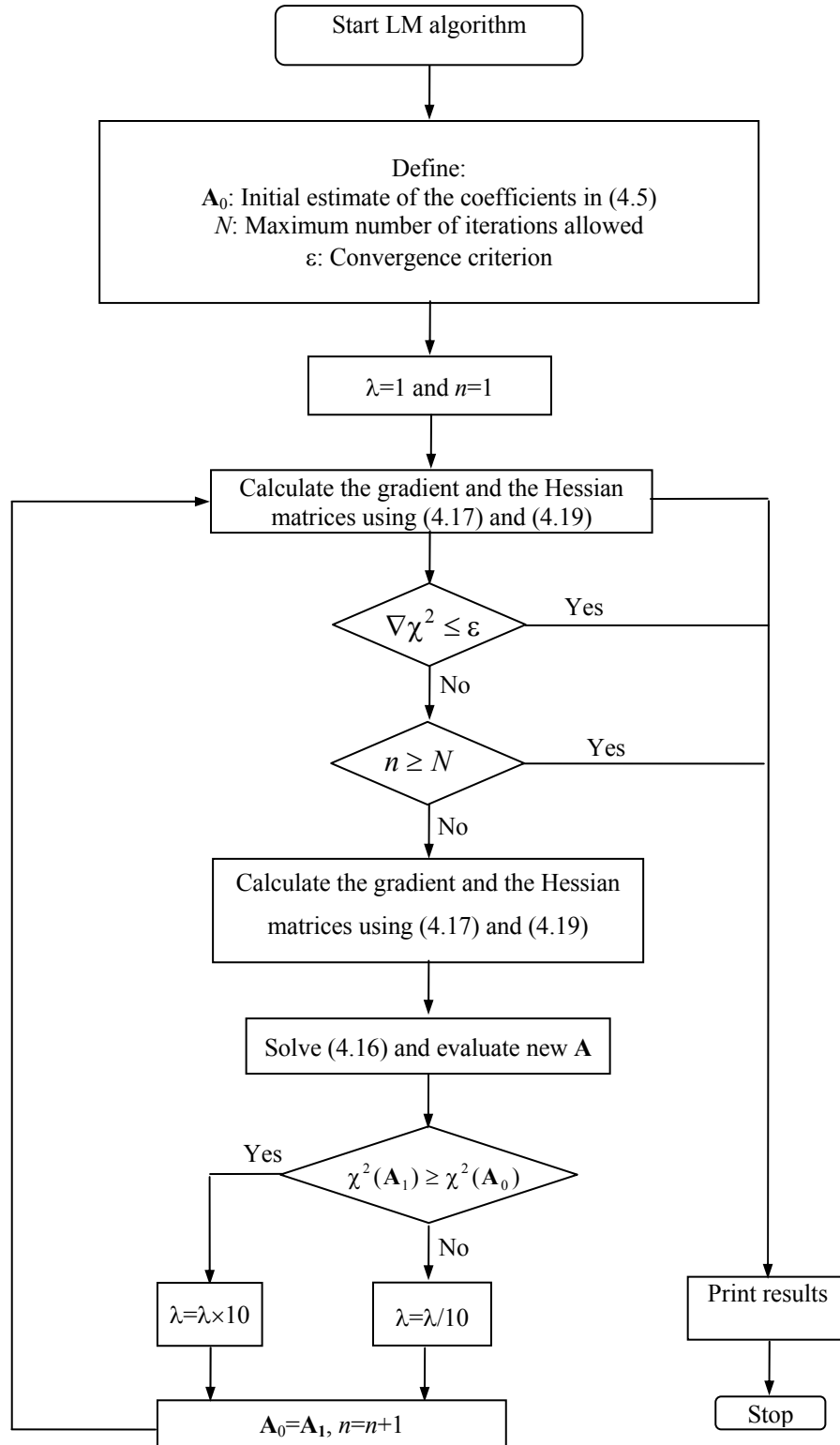
Fig. 4.2. Flowchart of the LM optimization algorithm.

4.2. Numerical Investigations and Comparison

In the previous section the LM algorithm implementation procedure to represent the magnetization characteristics was discussed in detail. One of the major dominating features of the LM algorithm, over other existing methods, is that the magnetization characteristics can be expressed by different functions. Therefore, based on the application, one can choose a desirable format of the optimization function. Moreover, decreasing the error criterion, ε, in the recursive procedure for the LM method, results in more accurate curves which can be fitted to measured data points. The only limitation to be considered is that the desired function must have real domain and range over the interval of magnetizing current. Moreover, this algorithm can be applied to different kinds and sizes of electrical machines. In this section, this method is numerically validated to represent the magnetization characteristics of a synchronous machine and a laboratory permanent magnet synchronous machine (PMSM).

4.2.1. Magnetization Representation of the Synchronous Machine Using the LM Method

In this research, ten sample characteristics functions are employed as different expressions of the magnetization characteristics in the synchronous machines under investigation. The list of functions along with the coefficients generated by the proposed model for the Lambton generator magnetization characteristics are presented in Table 4.1. The

first function in this list is selected to be used for comparison with similar methods such as the DFT and the Trigonometric models.

In this section the magnetization characteristics of the Lambton synchronous generator is represented by the proposed model in this chapter and it is been compared with other existing methods. Fig. 4.3 shows the Lambton magnetization characteristics for both direct and quadrature axes represented with the proposed method and with the first order of the trigonometric model. As can be seen in this figure, in terms of accuracy, both models describe the magnetization characteristics very effectively. Nevertheless, the results demonstrated in Fig. 4.4 show that compared to the proposed model, the DFT model is not as accurate.

To numerically validate the proposed algorithm, in this section, the Chi-square test is carried out on some of the profile functions expressing magnetization characteristics of the synchronous machine under investigation. To compare the goodness of fit, the same method is applied to some of the proposed methods in other literature. The Pearson's Chi-square testing can be expressed by (4.28)

$$\chi^2 = \sum_{i=1}^{n} \frac{(\Psi_M - \Psi_E)^2}{\Psi_E} \tag{4.28}$$

where χ^2 is the Pearson cumulative test statics which asymptotically approaches a chi-square. Ψ_M is the measured flux data set while Ψ_E is the expected data set, and n is the number of data points. In Table 4.2, the calculated errors for the magnetization characteristics according to the existing models and their implementations with the proposed algo-

rithm are presented. The results demonstrate the effectiveness of the proposed method in fitting the magnetization characteristics of synchronous machines.

4.2.2.   Modeling Magnetization of the Permanent Magnet Synchronous Machine Using the LM Method

To demonstrate that the proposed magnetization model can be applied to any kind of electric machine, this section focuses on the numerical investigations of the applied LM model to represent the magnetization characteristics of a 21 hp laboratory PMSM.

The ratings and specifications of this machine are described in Appendix A. To compare the performance of the developed model, the sinusoidal function (similar to the function with profile no. 2 in Table 4.1, is selected for the optimization algorithm and the results are compared to the similar sinusoidal interpolation method which is yield using the DFT technique.

Figs. 4.5 and 4.6 show the numerical results by the DFT and the corresponding sinusoidal function used in the LM algorithm for the PMSM flux along the direct and quadrature axes respectively. As it can be seen in these figures, the results for the proposed optimization model are more accurate than the results for the DFT model.
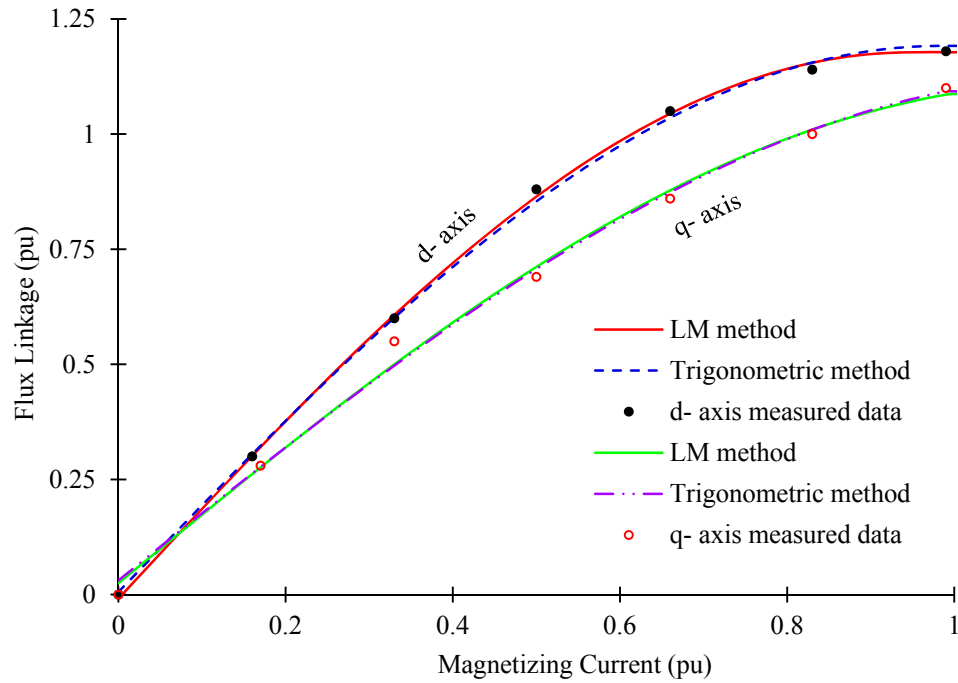
Fig. 4.3. The LM and trigonometric representation of measured data points of the magnetization characteristics of the Lambton generator.
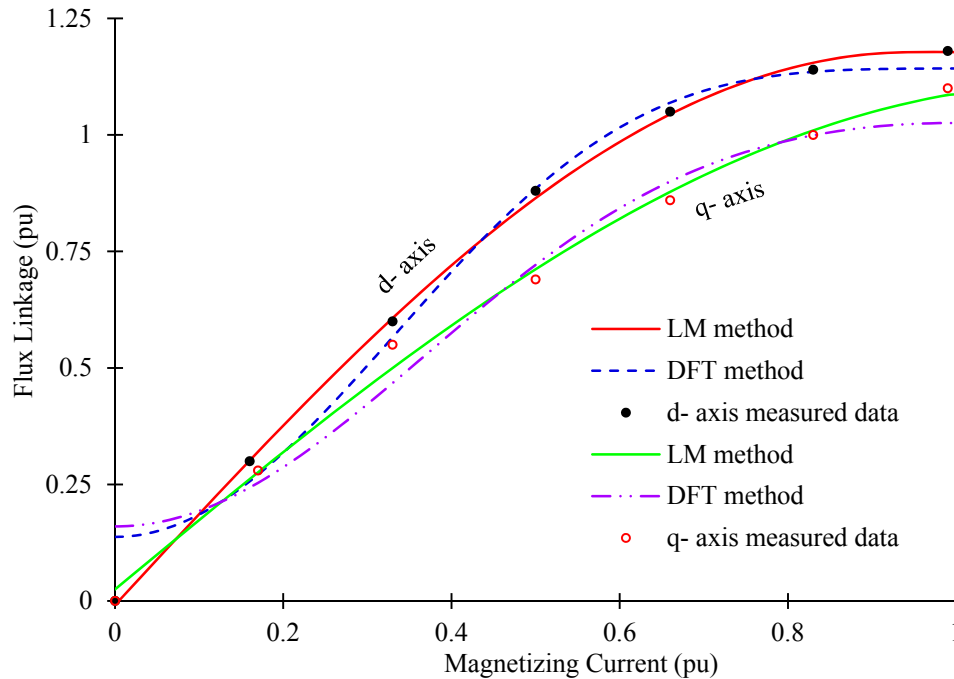
Fig. 4.4. The LM and DFT representation of measured data points of the magnetization characteristics of the Lambton generator.

Table 4.1. Ten Sample Magnetization Characteristics Functions and Their Corresponding Coefficients Generated by the Proposed Method for the Lambton Synchronous Machine

No.	Magnetization Function	Axis	Coefficients					
			a_1	a_2	a_3	a_4	a_5	a_6
1	$a_1 \cos(a_2 I_m) + a_3 \sin(a_2 I_m)$	d	-0.009	1.663	1.178			
		q	0.025	1.345	1.112			
2	$a_1 \cos(a_2 I_m) + a_3 \sin(a_4 I_m)$	d	-0.003	-16.193	-1.177	-1.647		
		q	0.0280	4.288	1.120	1.409		
3	$a_1 \cosh(a_2 I_m) + a_3 \sinh(a_4 I_m)$	d	-0.026	4.042	-155.9	-0.012		
		q	0.101	0	7.462	0.145		
4	$a_1 \cos(e^{(a_2 I_m)} I_m) + a_3 \sin(e^{(a_4 I_m)} I_m)$	d	-0.035	8.215	2.335	-0.600		
		q	0.001	1.197	1.833	-0.441		
5	$a_1 e^{(a_2 I_m^2)}(\cos(a_3 I_m^2)) + a_4 \sin(a_5 I_m)$	d	-0.007	1.4270	2.627	1.161	1.702	
		q	0.007	6.038	1.419	0.768	2.214	
6	$a_1 e^{(a_2 I_m)} \cos(a_3 I_m) + a_4 I_m \sin(a_5 e^{(a_6 I_m)})$	d	-0.007	1.269	0.904	2.054	1.787	0.346
		q	-0.007	1.269	0.904	2.054	1.787	0.346
7	$a_1 e^{(a_2 I_m)} \cos(a_3 I_m) + a_4 \sin(a_5 I_m e^{(a_6 I_m)})$	d	-0.008	1.115	1.092	1.189	1.643	0.015
		q	0.002	1.034	1.237	1.810	1.009	-0.440
8	$a_1 (I_m)^{a_2} \cos(a_3 I_m) + a_4 (I_m)^{a_5} \sin(a_6 I_m)$	d	0.732	4.630	0.837	1.026	0.172	2.405
		q	3.339	4.864	1.219	-0.656	0.088	-3.221
9	$a_1 e^{(a_2 I_m)} \tan(\cos(a_3 I_m)) + a_4 e^{(a_5 I_m)} \sin(a_6 I_m)$	d	0.732	4.630	0.838	1.026	0.172	2.405
		q	3.339	4.864	1.219	-0.655	0.088	-3.221
10	$a_1 \log(a_2(\cos I_m)^2)\cos(a_3 I_m) + a_4 e^{(a_5 I_m)} \sin(a_6 I_m)$	d	1.519	0.997	2.101	0.595	1.180	3.021
		q	3.280	0.999	0.638	2.425	0.887	0.831

Table 4.2. Chi-Square Test Results for Different Magnetization Representation Models of the Lambton Synchronous Generator

Magnetization Representation $\Psi(I_m)$	Realization	Error	
		d-axis	q-axis
$\alpha_1 \cos(\upsilon_1 I_m) + \beta_1 \sin(\upsilon_1 I_m)$	Trigonometric [45]	0.008	0.037
	LM Method	0.010	0.031
$a_0 + a_1 \cos(\dfrac{\pi I_m}{I_{mn}}) + a_2 \cos(\dfrac{2\pi I_m}{I_{mn}})$	DFT [22], [23]	0.145	0.186
	LM Method	0.114	0.161
$a_0 + a_1 I_m + a_2 I_m^2$	Polynomial [12]	0.030	0.014
	LM Method	0.030	0.014
$\dfrac{a_0 + a_1 I_m + a_2 I_m^2}{b_0 + b_1 I_m + b_2 I_m^2}$	Rational-Fraction [13]	0.0014	0.008
	LM Method	0.002	0.005

To evaluate the accuracy of the proposed fitting technique in comparison with that of the DFT model, the chi-squared function is applied to both of the magnetization characteristic models using (4.28). The corresponding error calculation results are presented in Table 4.3. The results clarify the fact that with the same degree of complexity according to the number of sinusoidal terms in the model the proposed optimization method leads to a more accurate fit for magnetization characteristics based on the measured data points.

As it is mentioned before one of the advantages of using the LM optimization algorithm is that this algorithm is independent of the selected function and based on the
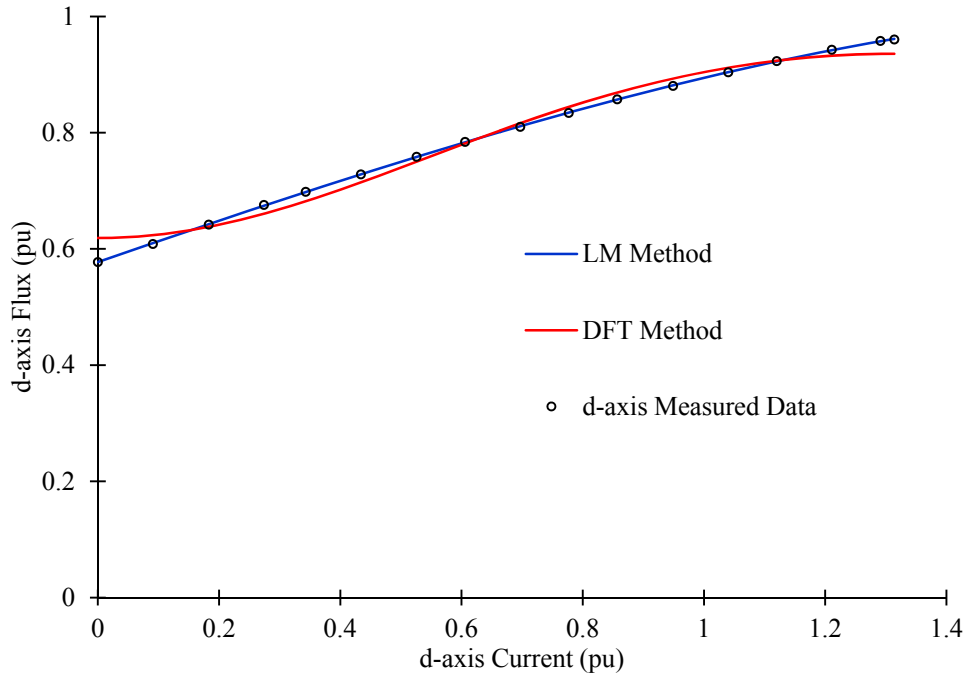
Fig. 4.5. Calculated d- axis magnetization characteristics of the laboratory PMSM employing the LM model and the DFT curve fitting method.
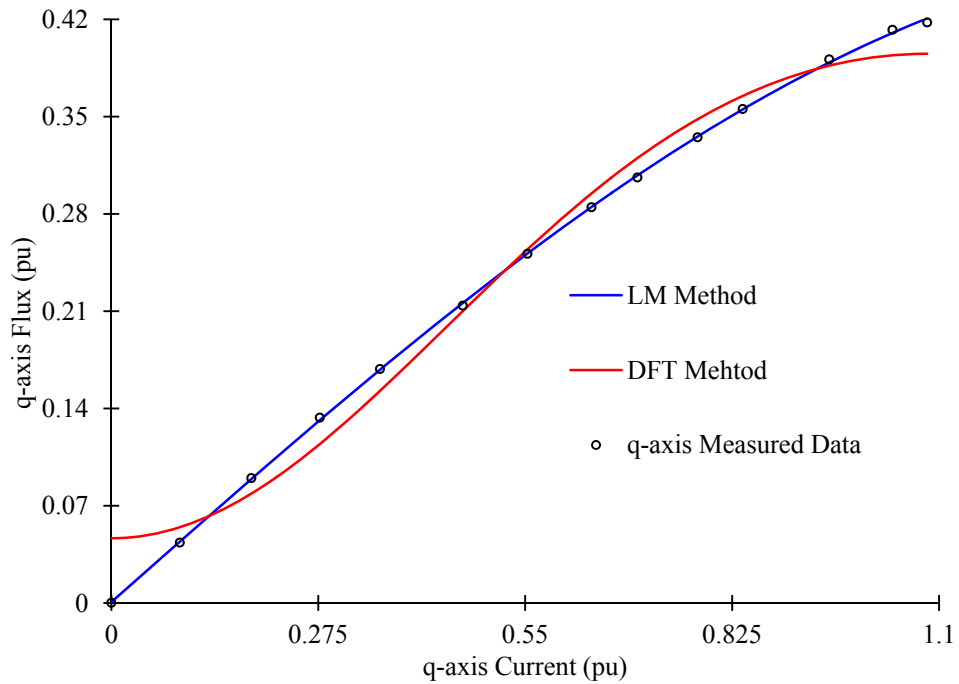
Fig. 4.6. Calculated q- axis magnetization characteristics of the laboratory PMSM employing the LM model and the DFT curve fitting method.

application, different non-linear functions can be selected for the magnetization charac-teristics. Some of the non-linear functions and the numerical regression results according to the q-axis PMSM magnetization characteristics as well as the error calculations are presented in Table 4.4. In addition, the investigations for the functions given in Table 4.4, are presented in Fig. 4.7 which shows the effectiveness of this method to express the magnetization characteristics of the machine based on different non-linear functions.

Table 4.3. Coefficients and the Corresponding Errors Calculated for the PMSM Magnetization Characteris-tics Using the DFT and LM Optimization Algorithms

$a_1 + a_2 \cos(a_3 x) + a_4 \cos(a_5 x)$						
Method	Coefficient					Error
	a_1	a_2	a_3	a_4	a_5	
DFT (q-axis)	0.2351	-0.1743	5.7910	-0.0142	4.2209	0.2500
LMO (q-axis)	0	0.00072	1.49	0.4725	3.2117	0.0017
DFT (d-axis)	0.2713	-0.1585	4.7817	-0.0120	3.1498	0.5095
LMO (d-axis)	0.0576	0.00192	3.7088	0.4362	0.8254	0.0011

Table 4.4. Coefficients and the Corresponding Errors Calculated by Different Non-linear Functions of the q-axis Magnetization Characteristics Applying the LM Optimization Algorithm.

Magnetization Model No.	Function	Error	Coefficient
1	$a_1 e^{(a_2 x^2)} \cos(a_3 x^2) + a_4 \sin(a_5 x)$	0.00043	a_1=0.00061 a_2=4.4993 a_3=1.2138 a_4=0.42579 a_5=1.1297
2	$a_1 e^{(a_2 x)} \cos(a_3 x) + a_4 \sin(a_5 x)$	0.00041	a_1=0.00011 a_2=6.4971 a_3=1.0817 a_4=-0.38878 a_5=-1.2459
3	$a_1 \cos(a_2 x) + a_3 \sin(a_4 x)$	0.0017	a_1=0.00072 a_2=1.49 a_3=0.47251 a_4=3.2117
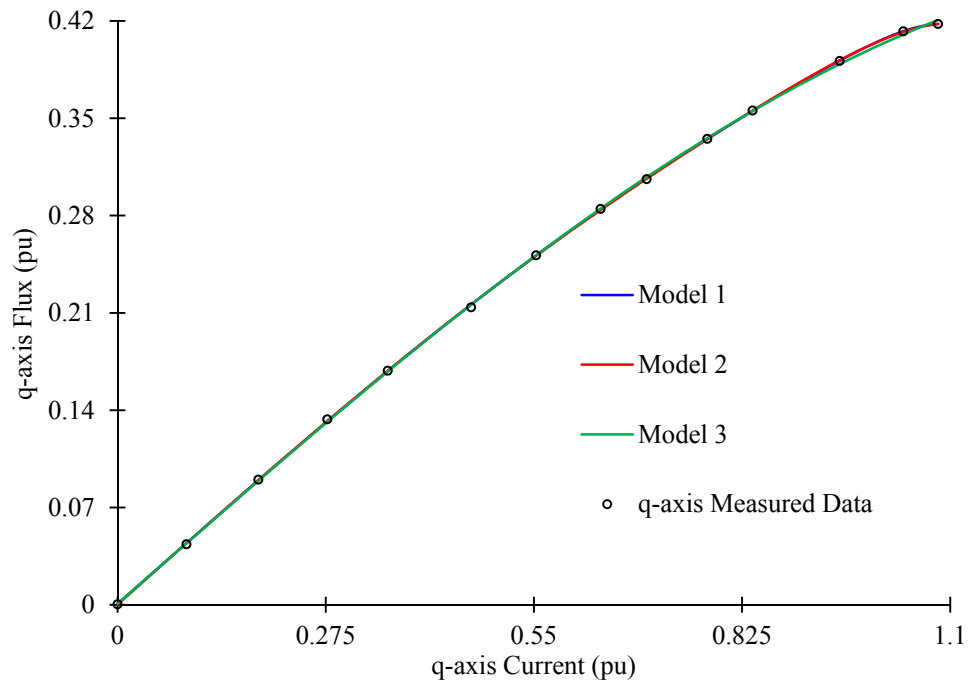
Fig. 4.7. Calculated q-axis magnetization characteristics of the laboratory PMSM employing the LM model for different functions listed in Table 4.4.

4.2.3. Comparison Study on the Different Magnetization Models

To compare the efficiency and applicatory of the magnetization models introduced in this dissertation a comprehensive comparison is carried on based on different criterions. The results are summarized in Table 4.5. As indicated in this table, the trigonometric method is privileged particularly when more accurate model with less computational time is needed. Inasmuch as the designer can choose any configuration using the LM method, this model benefits from the flexibility property in compare to other methods. The numerical error calculation analysis on the different magnetization configurations implemented by LM method show that this method is also very accurate. However, since the LM algorithm is iterative, the model suffers from having the long computational time.

Table 4.5. Comparison Study on the Magnetization Models Introduced in this Dissertation

Curve Fitting Method	Accuracy	Flexibility	Computational Time
Trigonometric	✓✓✓✓✓	✓	-
Levenberg-Marquardt	✓✓✓✓	✓✓✓✓✓	✓
DFT	✓	✓	-
Polynomial	✓✓	✓	-
Rational	✓✓✓✓	✓	✓

4.3. Conclusion

A new method to represent the magnetization characteristics of synchronous machines in different formats is presented. The proposed algorithm is very accurate and flexible, allowing researchers with varying applications to choose their own expression of magnetization phenomenon. Numerical analysis has been carried out to validate the accuracy of the proposed magnetization characterization method for synchronous and PMSM in comparison to some other existing methods.

A part of work developed in this chapter has already been presented in the Vehicle Power and Propulsion Conference (VPPC'11) [50]. The more comprehensive paper based on the presented work has been submitted to IEEE Transactions on Energy Conversion [51].

Chapter 5

A State Space Synchronous Machine Model Using LM Magnetizing Model

In Chapters 3 and 4, two methods to formulize the magnetization in electrical machines were developed. In this chapter a steady state model of synchronous machine employing the magnetization model proposed in chapter 4 is presented. Accordingly, in chapter 6, the magnetization model described in chapter 3 is incorporated into a transient synchronous machine model.

The concept of steady state stability in electrical machines implies that small changes in the terminal inputs, the initial conditions, or the machine parameters do not result in severe changes in the machine output. Similar to all other working systems, synchronous generators are designed to work in a stable situation. Therefore, the study on stability

boundaries of synchronous machines results in performance improvement [1], [29]. Furthermore, inclusion of the proposed LM model proposed in Chapter 4, into the developed state space model for synchronous machines has led to a comprehensive and complete model which can be used for performance analysis of synchronous generators. It has been demonstrated that the LM algorithm provides an accurate synthesis for the steady state analysis of synchronous machines.

5.1. State Space Synchronous Machine Model

To develop the machine model in this study the linearization technique is being employed. In the following sections the modeling procedure is discussed in detail.

5.1.1. Linearization of Magnetization Model

As discussed in Chapter 4, the LM magnetization model can be employed to represent the magnetization phenomenon characteristics in an arbitrary configuration provided that the function fulfills the requirements mentioned in section 4.2. Suppose that the selected magnetization configuration is in the general format of

$$
\left.
\begin{aligned}
X_{md}\left(I_{md}\right) &= \frac{\Psi_{md}(I_{md})}{I_{md}} \rightarrow f\left(X_{md}, I_{md}\right) = 0 \\
X_{mq}\left(I_{mq}\right) &= \frac{\Psi_{mq}(I_{mq})}{I_{mq}} \rightarrow g\left(X_{mq}, I_{mq}\right) = 0
\end{aligned}
\right\}
\tag{5.1}
$$

in which Ψ_{md} and Ψ_{mq} are the direct and quadrature axis flux linkages, respectively. Performing the Taylor series expansion according to the linearization technique explained

at the beginning of this section for the d-axis reactance yields

$$f = f\left(X_{md0}, I_{md0}\right) + \left.\frac{\partial f}{\partial X_{md}}\right|_{(I_{md0})} \times \tilde{X}_{md} - \left.\frac{\partial f}{\partial I_{md}}\right|_{(I_{md0})} \times \tilde{I}_{md} = 0. \tag{5.2}$$

It follows that $f\left(X_{md0}, I_{md0}\right)=0$ which implies the linearized description of d-axis reactance as in (5.3)

$$\tilde{X}_{md} = \frac{\tilde{I}_{md}}{I_{md0}} \left[\left.\frac{\partial \Psi}{\partial I_{md}}\right|_{\overline{(I_{md0})}} - X_{md0} \right]. \tag{5.3}$$

Accordingly, linearized q-axis reactance is obtained as (5.4)

$$\tilde{X}_{mq} = \frac{\tilde{I}_{mq}}{I_{mq0}} \left[\left.\frac{\partial \Psi}{\partial I_{mq}}\right|_{\overline{(I_{mq0})}} - X_{mq0} \right]. \tag{5.4}$$

Therefore, the magnetization coefficients of γ_{ds} and γ_{qs} can be defined for direct and quadrature axes respectively.

$$\gamma_{ds} = \frac{\left[\left.\frac{\partial \Psi}{\partial I_{md}}\right|_{\overline{(I_{md0})}} - X_{md0} \right]}{I_{md0}} \tag{5.5}$$

and

$$\gamma_{qs} = \frac{\left[\left.\frac{\partial \Psi}{\partial I_{mq}}\right|_{\overline{(I_{mq0})}} - X_{mq0} \right]}{I_{mq0}}. \tag{5.6}$$

Consequently, (5.3) and (5.4) can be written in matrix format as (5.7)

$$\begin{bmatrix} \widetilde{X}_{md} \\ \widetilde{X}_{mq} \end{bmatrix} = \begin{bmatrix} \gamma_{ds} & 0 \\ 0 & \gamma_{qs} \end{bmatrix} \begin{bmatrix} \widetilde{I}_{md} \\ \widetilde{I}_{mq} \end{bmatrix}. \tag{5.7}$$

Considering

$$\left. \begin{aligned} I_{md} &= I_d + I_{kd1} + I_{fd} \\ I_{mq} &= I_q + I_{kq1} + I_{kq2} \end{aligned} \right\} \tag{5.8}$$

(5.7) can be rewritten as (5.9)

$$\begin{bmatrix} \widetilde{X}_{md} \\ \widetilde{X}_{mq} \end{bmatrix} = \begin{bmatrix} -\gamma_{ds} & \gamma_{ds} & \gamma_{ds} & 0 & 0 & 0 \\ 0 & 0 & 0 & -\gamma_{qs} & \gamma_{qs} & \gamma_{qs} \end{bmatrix} \times \begin{bmatrix} \widetilde{I}_d \\ \widetilde{I}_{kd1} \\ \widetilde{I}_{fd} \\ \widetilde{I}_q \\ \widetilde{I}_{kq1} \\ \widetilde{I}_{kq2} \end{bmatrix} = \gamma \widetilde{\mathbf{I}}. \tag{5.9}$$

5.1.2. *Linearization of Synchronous Generator Model*

Considering the synchronous machine equations, (5.10) can be determined as

$$\mathbf{X} = \mathbf{X_s} \times \mathbf{I} \tag{5.10}$$

in which, **X** and **I** are defined by (5.11).

$$\mathbf{X} = \begin{bmatrix} \Psi_d \\ \Psi_{kd1} \\ \Psi_{fd} \\ \Psi_q \\ \Psi_{kq1} \\ \Psi_{kq2} \end{bmatrix} \quad \text{and} \quad \mathbf{I} = \begin{bmatrix} I_d \\ I_{kd1} \\ I_{fd} \\ I_q \\ I_{kq1} \\ I_{kq2} \end{bmatrix} \tag{5.11}$$

and $\mathbf{X_s}$ can be written as

$$\mathbf{X_s} = \begin{bmatrix} -(X_{mds}+X_l) & X_{mds} & X_{mds} & 0 & 0 & 0 \\ -X_{mds} & (X_{mds}+X_{kd1}) & X_{mds} & 0 & 0 & 0 \\ -X_{mds} & X_{mds} & (X_{mds}+X_{fd}) & 0 & 0 & 0 \\ 0 & 0 & 0 & -(X_{mqs}+X_l) & X_{mqs} & X_{mqs} \\ 0 & 0 & 0 & -X_{mqs} & (X_{mqs}+X_{kq1}) & X_{mqs} \\ 0 & 0 & 0 & -X_{mqs} & X_{mqs} & (X_{mqs}+X_{kq2}) \end{bmatrix}$$

$$(5.12)$$

From (5.10), one can conclude:

$$\widetilde{\mathbf{X}} = \mathbf{X_s}\widetilde{\mathbf{I}} + \mathbf{I_{ini}}\widetilde{\mathbf{X_m}}. \tag{5.13}$$

where,

$$\widetilde{\mathbf{X}} = \begin{bmatrix} \widetilde{\Psi}_d \\ \widetilde{\Psi}_{kd1} \\ \widetilde{\Psi}_{fd} \\ \widetilde{\Psi}_q \\ \widetilde{\Psi}_{kq1} \\ \widetilde{\Psi}_{kq2} \end{bmatrix}, \ \widetilde{\mathbf{I}} = \begin{bmatrix} \widetilde{I}_d \\ \widetilde{I}_{kd1} \\ \widetilde{I}_{fd} \\ \widetilde{I}_q \\ \widetilde{I}_{kq1} \\ \widetilde{I}_{kq2} \end{bmatrix}, \ \widetilde{\mathbf{X_m}} = \begin{bmatrix} \widetilde{X}_{md} \\ \widetilde{X}_{mq} \end{bmatrix}, \ \text{and} \ \mathbf{I_{ini}} = \begin{bmatrix} -I_{md0} & 0 \\ -I_{md0} & 0 \\ -I_{md0} & 0 \\ 0 & -I_{mq0} \\ 0 & -I_{mq0} \\ 0 & -I_{mq0} \end{bmatrix}. \tag{5.14}$$

Considering (5.13) and (5.9), (5.15) can be obtained

$$\widetilde{\mathbf{X}} = \mathbf{X_s}\widetilde{\mathbf{I}} + \mathbf{I_{ini}}\boldsymbol{\gamma}\widetilde{\mathbf{I}}. \tag{5.15}$$

Therefore, (5.16) can be written as

$$\widetilde{\mathbf{X}} = \mathbf{X_{st}}\widetilde{\mathbf{I}} \tag{5.16}$$

in which

$$\mathbf{X_{st}} = \mathbf{X_s} + \mathbf{I_{ini}}\boldsymbol{\gamma}. \tag{5.17}$$

Considering the synchronous machine model electrical equations in Chapter 2 and applying the linearization, it implies

$$\dot{\tilde{\Psi}}_q = -\omega_B V_t \sin\delta_0 \tilde{\delta} + \omega_B R_a \tilde{I}_q - \Psi_{d0}\tilde{\omega}_r - \omega_{r0}\tilde{\Psi}_q. \tag{5.18}$$

$$\dot{\tilde{\Psi}}_d = \omega_B V_t \cos\delta_0 \tilde{\delta} + \omega_B R_a \tilde{I}_d + \Psi_{q0}\tilde{\omega}_r + \omega_{r0}\tilde{\Psi}_q. \tag{5.19}$$

$$\dot{\tilde{\Psi}}_{kd1} = -\omega_B R_{kd1}\tilde{I}_{kd1}. \tag{5.20}$$

$$\dot{\tilde{\Psi}}_{fd} = -\omega_B R_{fd}\tilde{I}_{fd}. \tag{5.21}$$

$$\dot{\tilde{\Psi}}_{kq1} = -\omega_B R_{kq1}\tilde{I}_{kq1}. \tag{5.22}$$

$$\dot{\tilde{\Psi}}_{kq2} = -\omega_B R_{kq2}\tilde{I}_{kq2}. \tag{5.23}$$

Similarly, the linearized synchronous machine mechanical equations can also be represented by:

$$\dot{\tilde{\delta}} = \tilde{\omega}_r. \tag{5.24}$$

$$\dot{\tilde{\omega}}_r = \frac{\omega_B}{2H}\left[\tilde{T}_m + \tilde{\Psi}_q I_{d0} + \Psi_{q0}\tilde{I}_d - \tilde{\Psi}_d I_{q0} - \Psi_{d0}\tilde{I}_q - K_D\tilde{\omega}_r\right]. \tag{5.25}$$

Therefore, one can conclude

$$\dot{\tilde{\mathbf{X}}} = \mathbf{T}\tilde{\mathbf{X}} + \mathbf{J}\tilde{\mathbf{I}} + \mathbf{B}\tilde{\mathbf{T}}_{\mathbf{m}} \tag{5.26}$$

in which

$$\dot{\tilde{\mathbf{X}}} = \begin{bmatrix} \dot{\tilde{\Psi}}_d \\ \dot{\tilde{\Psi}}_{kd1} \\ \dot{\tilde{\Psi}}_{fd} \\ \dot{\tilde{\Psi}}_q \\ \dot{\tilde{\Psi}}_{kq1} \\ \dot{\tilde{\Psi}}_{kq2} \\ \dot{\tilde{\omega}}_r \\ \dot{\tilde{\delta}} \end{bmatrix}, \quad \mathbf{B} = \begin{bmatrix} 0 \\ 0 \\ 0 \\ 0 \\ 0 \\ 0 \\ 0 \\ \dfrac{\omega_B}{2H} \end{bmatrix} \tag{5.27}$$

The matrices **T** and **J** are defined by (5.28) and (5.29), respectively

$$\mathbf{T} = \begin{bmatrix} 0 & 0 & 0 & \omega_{r0} & 0 & 0 & \omega_B V_t \cos\delta_0 & \Psi_{q0} \\ 0 & 0 & 0 & 0 & 0 & 0 & 0 & 0 \\ 0 & 0 & 0 & 0 & 0 & 0 & 0 & 0 \\ -\omega_{r0} & 0 & 0 & 0 & 0 & 0 & -\omega_B V_t \cos\delta_0 & -\Psi_{d0} \\ 0 & 0 & 0 & 0 & 0 & 0 & 0 & 0 \\ 0 & 0 & 0 & 0 & 0 & 0 & 0 & 0 \\ 0 & 0 & 0 & 0 & 0 & 0 & 0 & 1 \\ -\dfrac{\omega_0}{2H} I_{q0} & 0 & 0 & \dfrac{\omega_0}{2H} I_{d0} & 0 & 0 & 0 & -\dfrac{\omega_0}{2H} K_D \end{bmatrix} \tag{5.28}$$

and

$$\mathbf{J} = \begin{bmatrix} \omega_B R_a & 0 & 0 & 0 & 0 & 0 \\ 0 & -\omega_B R_{kd1} & 0 & 0 & 0 & 0 \\ 0 & 0 & -\omega_B R_{fd} & 0 & 0 & 0 \\ 0 & 0 & 0 & \omega_B R_a & 0 & 0 \\ 0 & 0 & 0 & 0 & -\omega_B R_{kq1} & 0 \\ 0 & 0 & 0 & 0 & 0 & -\omega_B R_{kq2} \\ 0 & 0 & 0 & 0 & 0 & 0 \\ \dfrac{\omega_B \Psi_{q0}}{2H} & 0 & 0 & -\dfrac{\omega_B \Psi_{d0}}{2H} & 0 & 0 \end{bmatrix}. \tag{5.29}$$

Using (5.18)-(5.25), (5.30) can be written as

$$\widetilde{\mathbf{I}} = \mathbf{X}_{st}^{-1}\widetilde{\mathbf{X}}. \tag{5.30}$$

Thus, upon substituting the matrices $\mathbf{T}$ and $\mathbf{J}$ and (5.25) in (5.21), the following can be obtained.

$$\dot{\widetilde{\mathbf{X}}} = \left(\mathbf{T} + \mathbf{J}\mathbf{X}_{st}^{-1}\right)\widetilde{\mathbf{X}} + \mathbf{B}\widetilde{\mathbf{T}}_{\mathbf{m}} = (\mathbf{T} + \mathbf{M})\widetilde{\mathbf{X}} + \mathbf{B}\widetilde{\mathbf{T}}_{\mathbf{m}}. \tag{5.31}$$

It implies that

$$\dot{\widetilde{\mathbf{X}}} = \mathbf{A}\widetilde{\mathbf{X}} + \mathbf{B}\widetilde{\mathbf{U}}. \tag{5.32}$$

5.2. Numerical Stability Studies on the Saturated and the Unsaturated Synchronous Machine Models

By applying the Laplace transform to (5.27), (5.28) can be obtained:

$$(s\mathbf{I}\text{-}\mathbf{A})\widetilde{\mathbf{X}} = \widetilde{\mathbf{X}}(\mathbf{0}) + \mathbf{B}\widetilde{\mathbf{U}}. \tag{5.33}$$

Therefore,

$$\widetilde{\mathbf{X}} = (s\mathbf{I}\text{-}\mathbf{A})^{-1}\left\{\widetilde{\mathbf{X}}(\mathbf{0}) + \mathbf{B}\widetilde{\mathbf{U}}\right\}, \tag{5.34}$$

where

$$(s\mathbf{I}\text{-}\mathbf{A})^{-1} = \frac{\operatorname{adj}(s\mathbf{I}\text{-}\mathbf{A})}{\det(s\mathbf{I}\text{-}\mathbf{A})}. \tag{5.35}$$

It can be seen that the poles of $\tilde{\mathbf{X}}$ are the roots of $(s\mathbf{I}\text{-}\mathbf{A})$. By definition, $(s\mathbf{I}\text{-}\mathbf{A}) = 0$ is known as the characteristic equation and its roots are called the eigenvalues corresponding to the system matrix $\mathbf{A}$.

According to the Lyapunov first law of stability [52], the system will be stable if all the eigenvalues of the state space equation of the system have negative real parts. Therefore, once the state space model of the system is defined, the scalar parameters λ can be calculated as the eigenvalues of the system using the following procedure:

$$\mathbf{A}\mathbf{V_R} = \lambda\mathbf{V_R} \tag{5.36}$$

in which $\mathbf{V_R}$ is called as the right eigenvector of the system. Consequently, the eigenvalues of the system can be obtained by modifying (5.36)

$$(\mathbf{A} - \lambda\mathbf{I})\mathbf{V_R} = 0 \Rightarrow (\mathbf{A} - \lambda\mathbf{I}) = 0. \tag{5.37}$$

$(\mathbf{A} - \lambda\mathbf{I})$ in (5.37) is the characteristic polynomial of the system. For an $n \times n$ matrix $\mathbf{A}$, the characteristic equation is a polynomial of degree n, and the n roots of $\lambda_1, \lambda_2, \ldots, \lambda_n$ are the eigenvalues. The corresponding right eigenvector associated with λ_i in (5.36) can be defined as in (5.38)

$$\mathbf{A}\begin{bmatrix} V_{R1i} \\ V_{R2i} \\ \vdots \\ V_{Rni} \end{bmatrix} = \lambda_i \times \begin{bmatrix} V_{R1i} \\ V_{R2i} \\ \vdots \\ V_{Rni} \end{bmatrix}. \tag{5.38}$$

Accordingly, the left eigenvector $\mathbf{V_L}$ of the system is defined by

$$\mathbf{V_L A} = \lambda \mathbf{V_L}.$$

(5.39)

$$\begin{bmatrix} V_{Li1} & V_{Li2} & \cdots & V_{Lin} \end{bmatrix} \mathbf{A} = \lambda_i \times \begin{bmatrix} V_{Li1} & V_{Li2} & \cdots & V_{Lin} \end{bmatrix}$$

(5.40)

To determine the relationship between the state variables and the system modes, the participation matrix can be established as a combination of left and right eigenvectors as expressed in (5.41)

$$\mathbf{P} = \begin{bmatrix} P_1 & P_2 & \cdots & P_i & \cdots & P_n \end{bmatrix}$$

(5.41)

It yields

$$\mathbf{P} = \begin{bmatrix} V_{R11}V_{L11} & \cdots & V_{R1j}V_{Lj1} & \cdots & V_{R1n}V_{Ln1} \\ \vdots & \ddots & \vdots & \ddots & \vdots \\ V_{Ri1}V_{L1i} & \cdots & V_{Rij}V_{Lji} & \cdots & V_{Rin}V_{Lni} \\ \vdots & \ddots & \vdots & \ddots & \vdots \\ V_{Rn1}V_{L1n} & \cdots & V_{Rnj}V_{Ljn} & \cdots & V_{Rnn}V_{Lnn} \end{bmatrix} \begin{matrix} \tilde{x}_1 \\ \\ \vdots \\ \\ \tilde{x}_i \\ \\ \vdots \\ \\ \tilde{x}_n \end{matrix} .$$

$$\quad\quad \lambda_1 \quad\quad\quad\quad\quad \lambda_i \quad\quad\quad\quad\quad \lambda_n$$

(5.42)

By definition, the entries of $\mathbf{P}$ are called the participation factors. $\mathbf{P_{i,j}}$ measures the level of participation of the ith mode and the kth state variable, $\tilde{x}_i$ with each other.

In Section 5.1.4, this matrix is calculated to determine the state variables and the mode relationship. Numerical investigations are carried out ignoring magnetization

(Model 1), considering magnetization only in the direct axis (Model 2), and considering magnetization both in the direct and quadrature axes (Model 3).

The analyses have been accomplished according to the Lambton synchronous machine which ratings and specifications are listed in Table A.2 and Table A.3, respectively.

5.2.1. *Synchronous Machine Stability Monitoring by Varying Active and Reactive Power*

The numerical investigations are carried on the Lambton synchronous machine supposing that the reactive and active power of the generator are changing from 0 to 1.2 pu. To determine the stability status of the machine according to the particular active and reactive power range, the dominant eigenvalues are monitored for the three models. The results are illustrated in Fig. 5.1. As can be seen in this figure, decreasing the reactive power enhances the machine stability for all the models. In addition, it can be noticed that there is a large discrepancy between the results for the saturated models and those related to the unsaturated model.
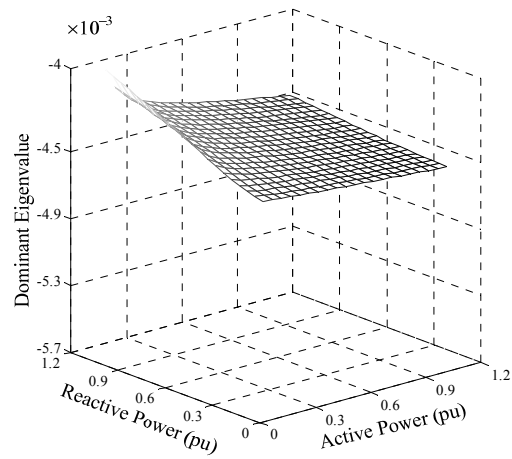
(a)
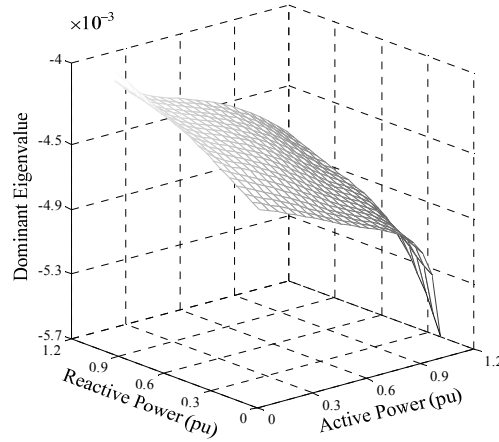
(b)
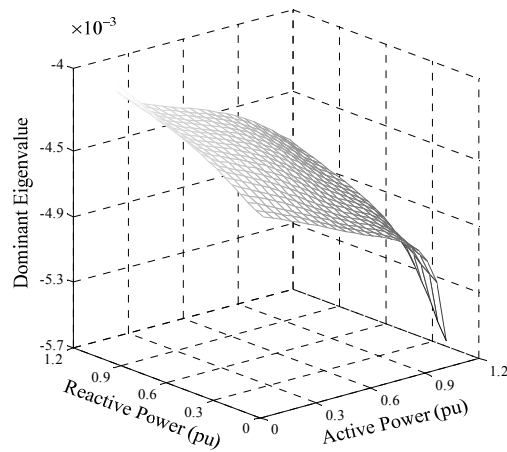
(c)

Fig. 5.1. The dominant eigenvalues for the three magnetization models of the synchronous generator. (a) Model 1. (b) Model 2. (c) Model3.
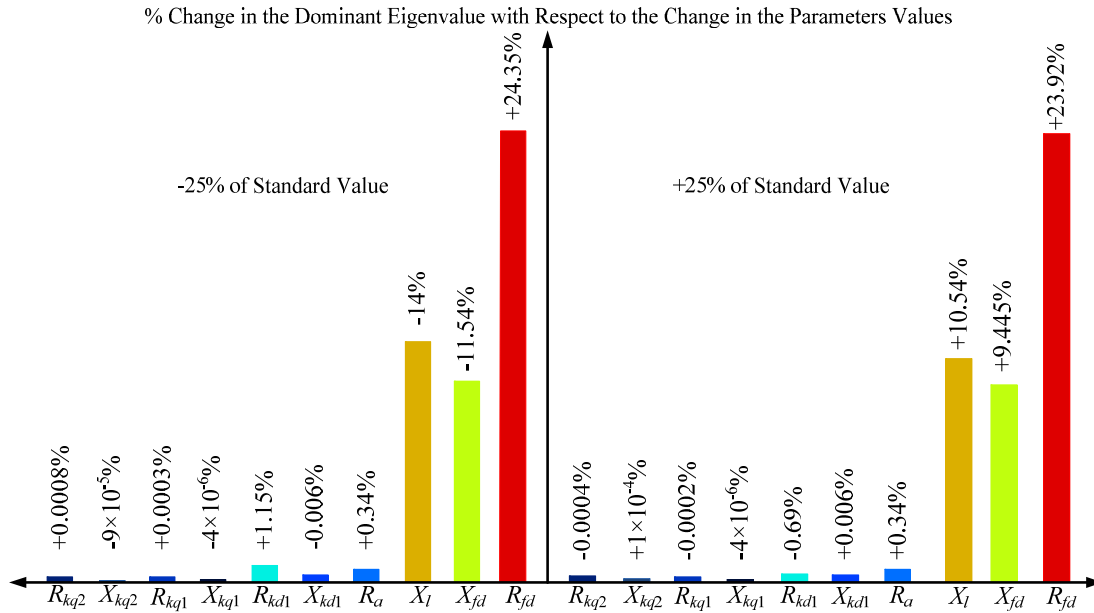
% Change in the Dominant Eigenvalue with Respect to the Change in the Parameters Values

Fig. 5.2. The dominant eigenvalue sensitivity as a function of the variation of the machine parameters calculated by machine model 3.

5.2.2. Synchronous Machine Stability Monitoring Considering the Machine Parameter Sensitivity

Although there are several methods to experimentally measure the parameters of a synchronous generator, it is inevitable to have uncertainty in the process of parameter measurements. Therefore, this error might lead to an unreliable stability analysis. To ascertain the sensitivity of synchronous machine stability to the variation of the machine parameters, the sensitivity analysis has been carried out. To perform this evaluation, all the machine parameters have been subject to a variation from -25% of the standard value to +25% of the standard value and the eigenvalues of the system are calculated.

To explore the worst case of stability, the dominant eigenvalue is monitored and the percentage of the variation corresponding to each machine parameter variation is calcu-

lated. The sensitivity of the dominant eigenvalue with respect to the machine equivalent circuit parameter, $\Re$, is calculated by (5.43). It can be noticed that there is a large discrepancy between the results for the saturated models and those related to the unsaturated model.

$$S_{\Re}^{E}\% = \left(\frac{E_S - E_{\pm 25\%}}{E_S} \right) \times 100 \tag{5.43}$$

where E_S and $E_{\pm 25\%}$ are the dominant eigenvalues calculated for the standard and $\pm 25\%$ of the standard values of each machine parameter respectively. The result of this analysis is illustrated in Fig. 5.2. As can be seen in this figure, the stability reliability is affected significantly by the accuracy of field resistance, the armature leakage reactance, and the field reactance.

5.2.3.   Frequency Analysis on the Synchronous Machine

In this section, the frequency analysis is accomplished using Bode and zero-pole diagrams of the synchronous machine. Considering the mechanical torque as the input for the Lambton synchronous machine, the transfer function of the saturated generator is obtained for the machine speed as the output. The Bode diagram of the system is plotted in Fig. 5.3. As can be seen in this figure the frequency response of the machine speed is very similar to a second order system in the general format of

$$H(s) = \frac{Ks}{s^2 + 2\xi\omega_n s + \omega_n^2} \qquad \text{for } \xi < 0.1 \tag{5.44}$$
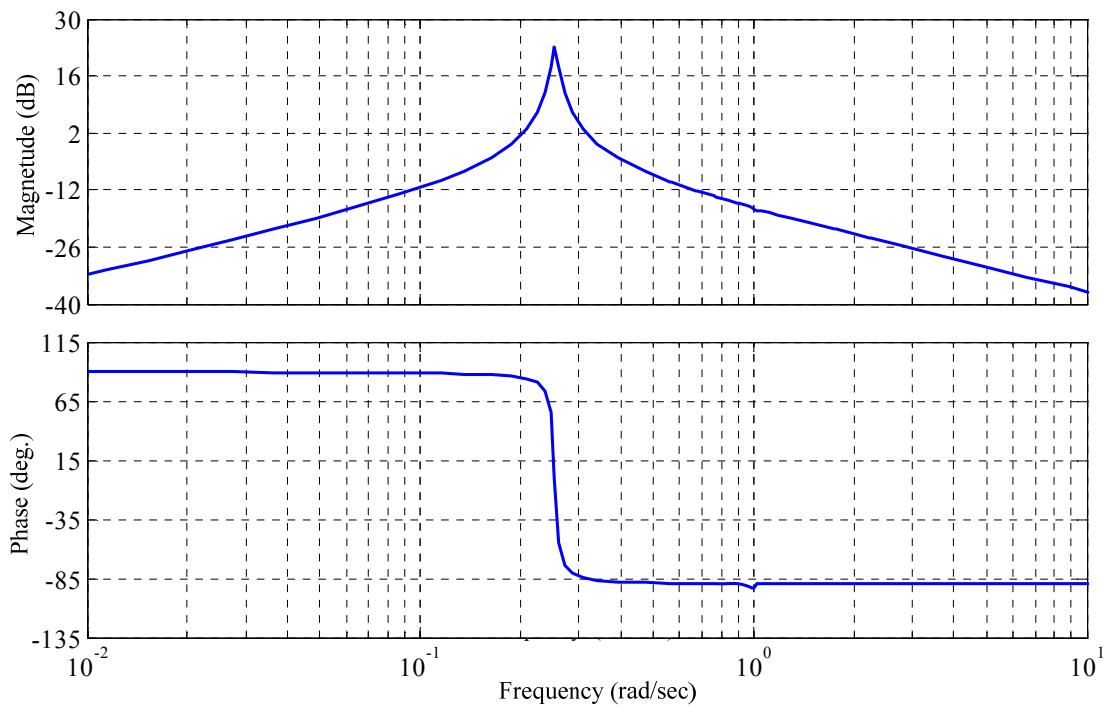
Fig. 5.3. The Bode diagram of the speed of the Lambton synchronous machine calculated using magnetization Model 3.
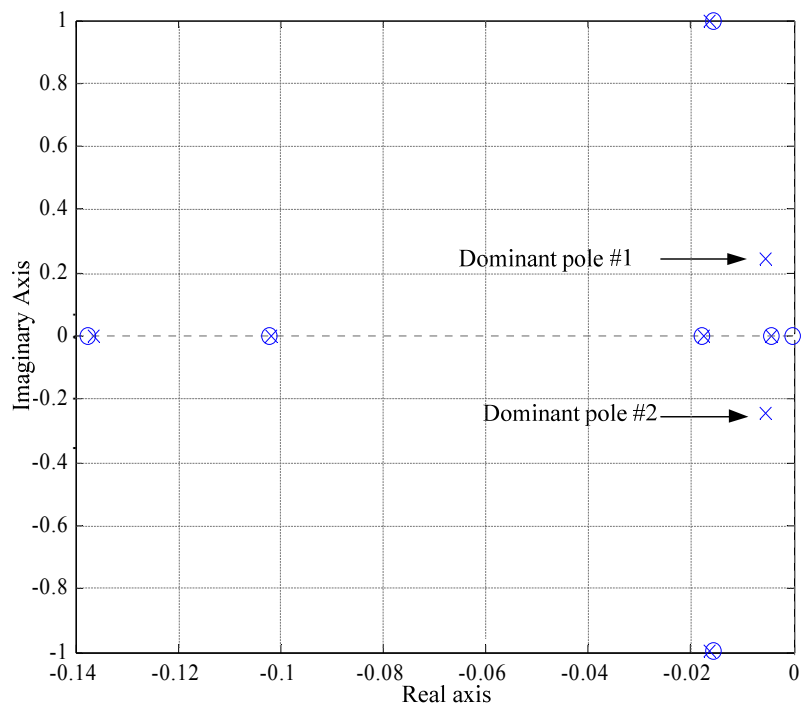

Fig. 5.4. The Zero-Pole diagram of the speed of the Lambton synchronous machine calculated using magnetization Model 3.

in which ξ is the damping ratio and ω_n is the natural frequency of the system. This system has one zero at origin and two complex poles. Considering the zero-pole plot of the synchronous generator in Fig. 5.4, it can be concluded that the dominant zeros and poles of the system are one zero at the origin and one pair of complex poles. Therefore, the steady state frequency response of the generator can be approximated by a second order system such as the system mentioned in (5.44). To determine the state variables, which cause the dominant poles of the system the participation matrix is calculated [1], [53]. For instance, the absolute values for participation matrix entries for the magnetization model 3 is calculated and presented in (5.45).

$$
\mathbf{P} =
\begin{bmatrix}
0.494 & 0.494 & 0.173 & 0.173 & 0.0002 & 0.0002 & 0 & 0 \\
0.0004 & 0.0004 & 0.0008 & 0.008 & 0.97 & 0 & 0.032 & 0 \\
0 & 0 & 0 & 0 & 0.032 & 0 & 0.968 & 0 \\
0.612 & 0.612 & 0.123 & 0.123 & 0 & 0 & 0 & 0 \\
0.0005 & 0.0005 & 0.0005 & 0.0005 & 0 & 0.935 & 0 & 0.065 \\
0 & 0 & 0 & 0 & 0 & 0.0653 & 0 & 0.935 \\
0.132 & 0.132 & 0.639 & 0.639 & 0.0014 & 0.0002 & 0.0001 & 0 \\
0.0029 & 0.0029 & 0.5021 & 0.5021 & 0.0004 & 0.0001 & 0 & 0
\end{bmatrix}
\begin{matrix}
\Psi_d \\
\Psi_{kd1} \\
\Psi_{fd} \\
\Psi_q \\
\Psi_{kq1} \\
\Psi_{kq2} \\
\delta \\
\omega
\end{matrix}
\quad (5.45)
$$

$$
\begin{matrix}
\lambda_1 & \lambda_2 & \lambda_3 & \lambda_4 & \lambda_5 & \lambda_6 & \lambda_7 & \lambda_8
\end{matrix}
$$

Based on this matrix, it can be concluded that the d- and q-axis fluxes are producing the dominant poles of the system. Performing the same analysis on the other magnetization models shows that magnetization does not affect the frequency response of the system significantly.

Next, the frequency analysis is accomplished for different values of active and reactive power. The results demonstrate that active power variation has no effect on the frequency response of the system. However, as illustrated in Fig. 5.5, increasing the reactive power from 0.2 pu to 1.4 pu results in an increase of the natural frequency for the system.
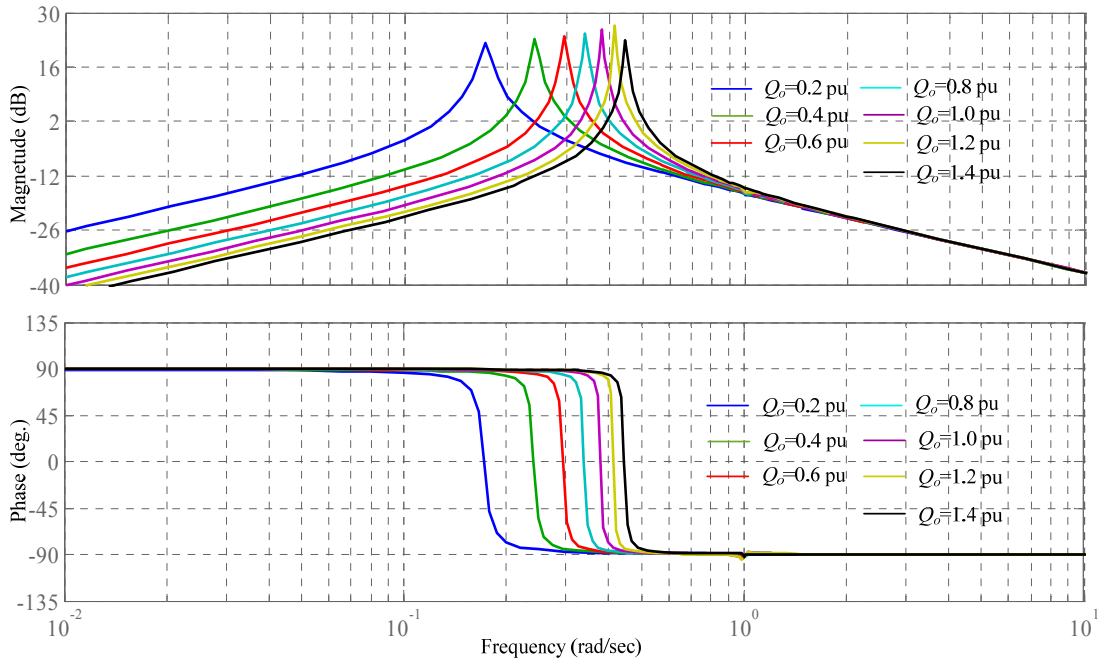

Fig. 5.5. Frequency response of the synchronous machine speed with respect to the reactive power variations for active power P_o=0.9 pu.

5.3. Conclusion

Numerical analysis employing the developed machine model demonstrates that magnetization affects the stability boundaries of the synchronous machine significantly. Moreover, sensitivity analysis on the machine reveals that the machine stability is affected mostly by variations in armature leakage reactance, field reactance, and field resistance. It has been also found that reactive power variation affects the frequency response of the synchronous generator.

The work developed in this chapter has been submitted to IEEE Transactions on Energy Conversion [51].

Chapter 6

Synchronous Machine Transient Performance Analysis under Momentary Interruption Considering Trigonometric Magnetization Model

In this chapter, the effectiveness of the proposed trigonometric magnetization model in Chapter 3 has been demonstrated by incorporating it into a conventional synchronous machine model. Transient stability analysis in time-frequency domain has been performed under a three-phase short-circuit condition. Based on this result, the effect of magnetization on machine performance in the case of an interruption at the machine terminals is investigated. It has been demonstrated that the proposed trigonometric magnetization algorithm provides an accurate synthesis for all the analyses.

6.1. Synchronous Machine Transient Performance Under Momentary Interruption

The proposed magnetization model is applied to a synchronous generator model in order to develop a more accurate machine model considering magnetization [54]. Numerical investigations in this chapter, are carried out ignoring magnetization (Model 1), considering magnetization only in the direct axis (Model 2), and considering magnetization both in the direct and quadrature axes (Model 3).

Referring to the synchronous generator equivalent circuit illustrated in Fig. 2.3 and based on mathematical representation for synchronous machine expressed in Table 2.2 in Chapter 2, the classical equations of synchronous machines in (6.1)-(6.8).

$$\frac{d\Psi_q}{dt} = \omega_B \left[e_q + R_a I_q - \frac{\omega_r}{\omega_B} \Psi_d \right]. \tag{6.1}$$

$$\frac{d\Psi_d}{dt} = \omega_B \left[e_d + R_a I_d + \frac{\omega_r}{\omega_B} \Psi_q \right]. \tag{6.2}$$

$$\frac{d\Psi_{kd1}}{dt} = -\omega_B R_{kd1} I_{kd1}. \tag{6.3}$$

$$\frac{d\Psi_{fd}}{dt} = \omega_B \left[e_{fd} \left(\frac{R_{fd}}{X_{md}} \right) - R_{fd} I_{fd} \right]. \tag{6.4}$$

$$\frac{d\Psi_{kq1}}{dt} = -\omega_B R_{kq1} I_{kq1}. \tag{6.5}$$

$$\frac{d\Psi_{kq2}}{dt} = -\omega_B R_{kq2} I_{kq2}.$$

(6.6)

The synchronous machine mechanical equations can be represented by:

$$\frac{d\delta}{dt} = \omega_r - \omega_B$$

(6.7)

$$\frac{d\omega_r}{dt} = -\frac{\omega_B}{2H}\left[T_e - T_L\right]$$

(6.8)

where δ is the load angle and T_e and T_L are the air-gap and load torque respectively.

The proposed interruption profile presented in Fig. 6.1 is used in the investigations of this chapter and can be expressed by (6.9)

$$V_{t0} = e^{-(t-t_0)/20\ Cycles} \ ; \ V_{t1} = 1 - e^{-(t-t_1)/20\ Cycles}$$

(6.9)

where V_{t0} is the voltage during the fault, whereas V_{t1} is the voltage after the fault is cleared. The calculation has been performed for an active and reactive power output of P=0.9 pu and Q=0.44 pu respectively. Equations (6.1)-(6.8) have been solved using the 4th order Runge-Kutta method.
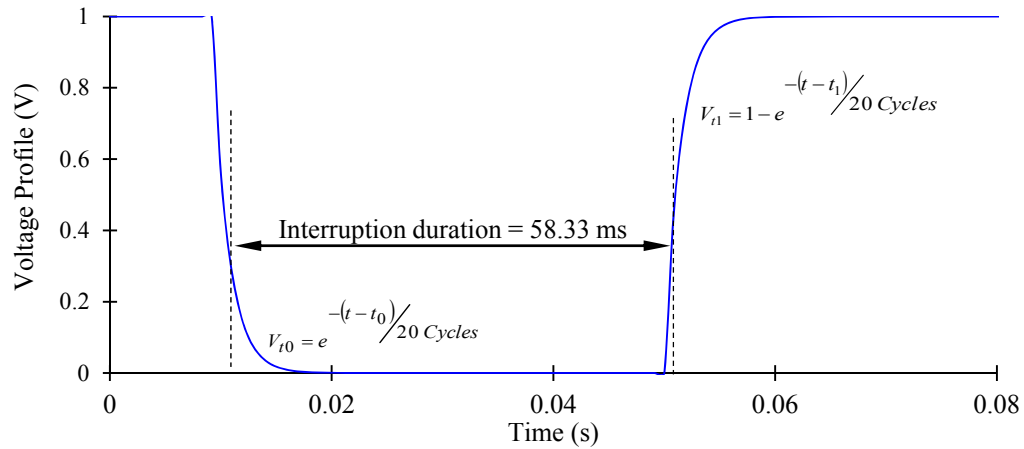
Fig. 6.1. Proposed voltage profile due to a momentary interruption at the machine terminals.

6.2. Synchronous Generator Performance Analysis Employing the Proposed Magnetization Model

In this section, numerical investigations are carried out on the synchronous machine model based on the Lambton synchronous machine parameters described in Appendix A. [38] employing the proposed trigonometric magnetization model.

6.2.1. *Dynamic Performance Analysis of the Saturated Synchronous Generator Considering and Ignoring AVR*

The air-gap torque and load angle calculated by the three models of synchronous machines are shown in Figs. 6.2 and 6.3 respectively. The interruption occurs at t=10 ms, while the machine is in the steady-state mode of operation. The fault is cleared after 58.33 ms (three and half cycles, for 60 Hz supply). As seen in these figures, the machine returns to its pre-disturbance conditions after 2 sec.
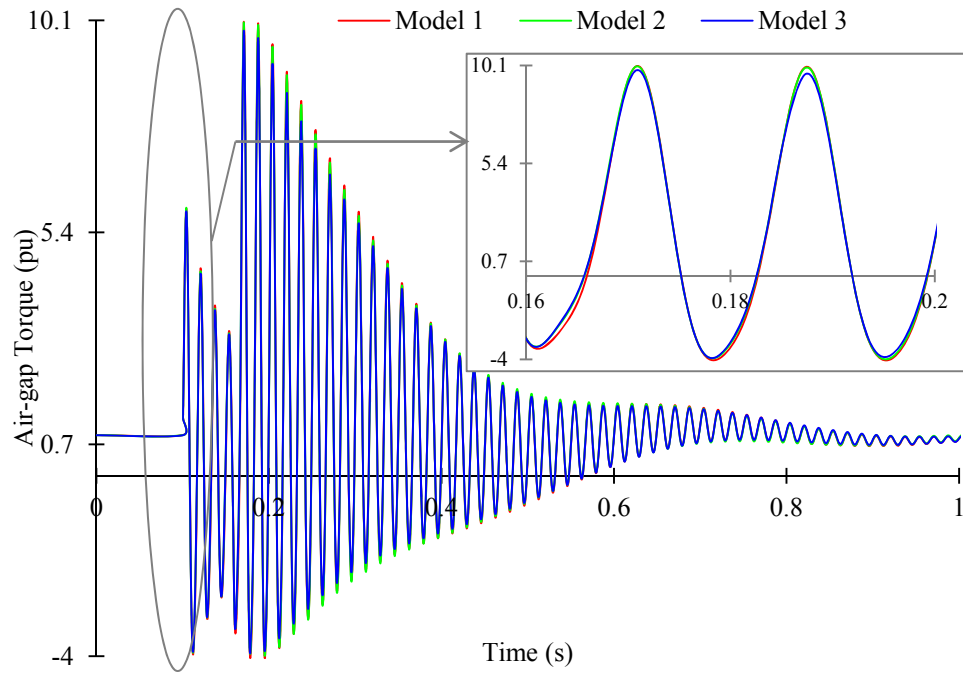
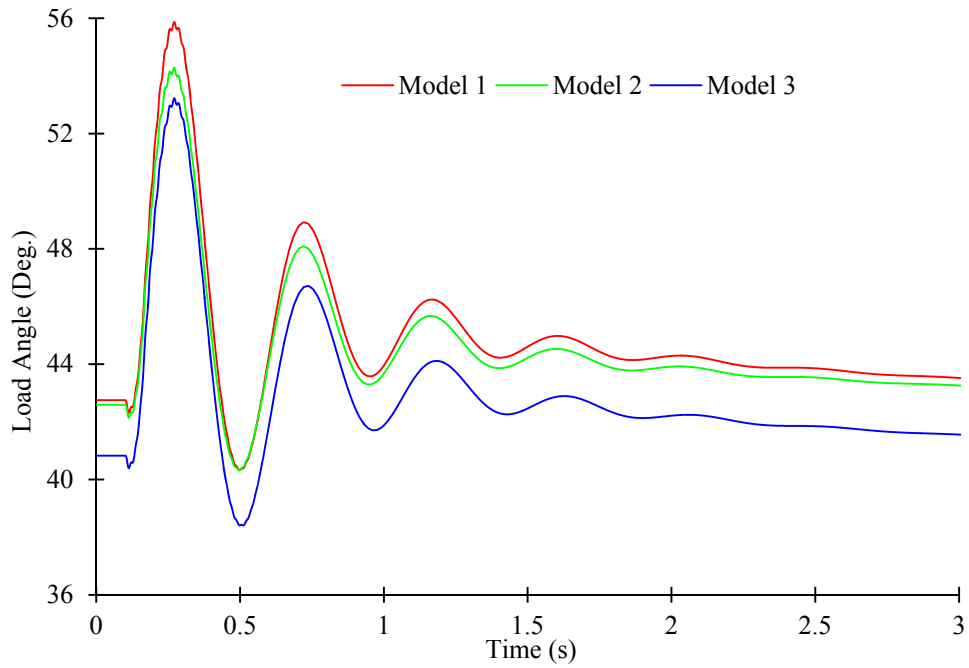Fig. 6.2. Air-gap torque calculated by the three synchronous machine models.

Fig. 6.3. Load angle calculated by the three synchronous machine models.

To compare the results of the influence of the proposed magnetization characteristics in performance analysis of the synchronous machine, the load angle response for marginally stable and unstable cases of the machine is investigated using proposed trigonometric magnetization models and the DFT magnetization model. As seen in Fig. 6.4, incorporation of the magnetization characteristics based on the trigonometric algorithm results in more accurate performance analysis of the machine. All the analysis hereafter in this chapter is conducted on the model incorporating an automatic voltage regulator (AVR). Fig. 6.5 illustrates the block diagram of an AVR. The AVR senses the terminal voltage variations with respect to a reference value.
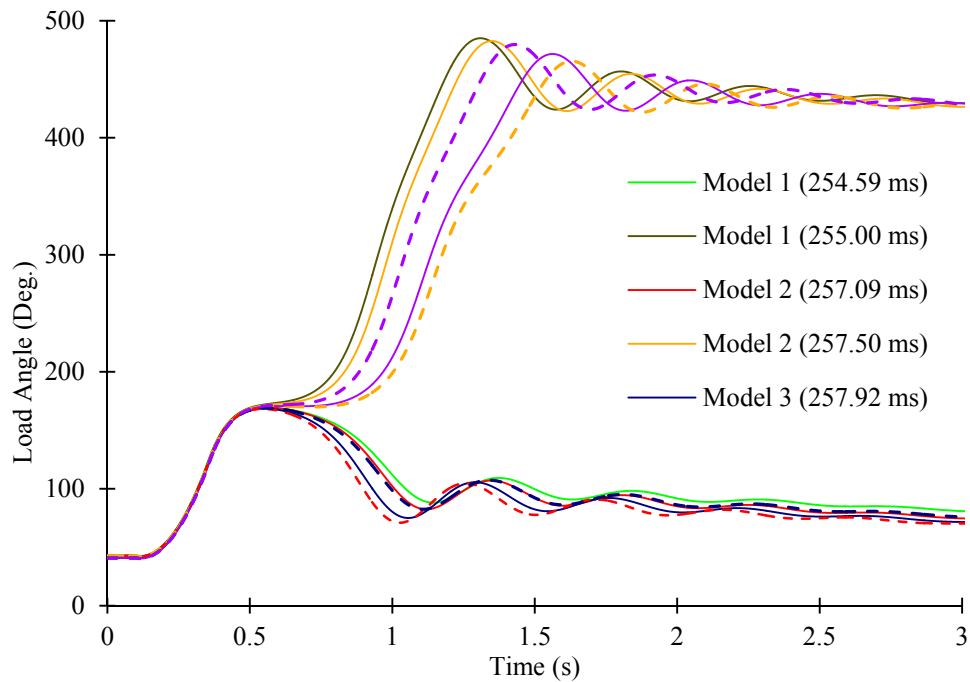

Fig 6.4. Load angle response for marginally stable and unstable cases calculated for the three models using proposed trigonometric and DFT method.
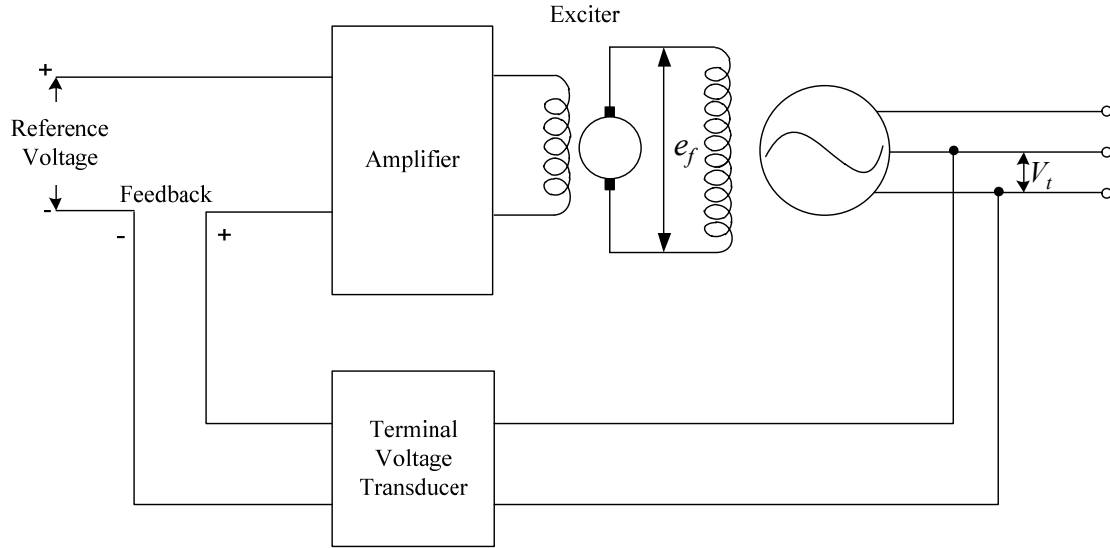
Fig. 6.5. AVR block diagram.

This helps improve system stability by adjusting the excitation in order to maintain a constant terminal voltage [55], [56]. In this study, the AVR parameters have been selected according to the sample data in [57] for the excitation model of ST1A. The rotor speed of the synchronous machine for the three magnetization models is presented in Fig. 6.6. As can be seen in this figure, the speed of the motor recovers to its pre-disturbance value of 1 pu after 2 sec. Fig. 6.7 presents the air-gap torque of the machine. During the disturbance and after the clearing of the fault, the maximum value of the air-gap torque for Model 1 is slightly greater than the values for Models 2 and 3. It is evident that the oscillations maintain the same frequency for all cases.
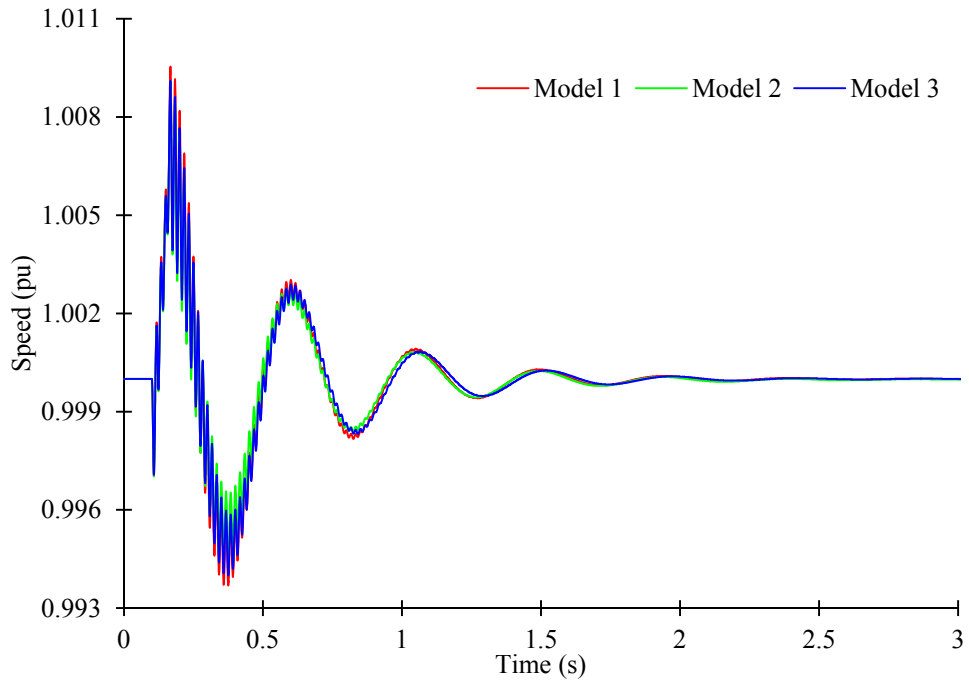
Fig. 6.6. Machine rotor speed calculated by the three models.
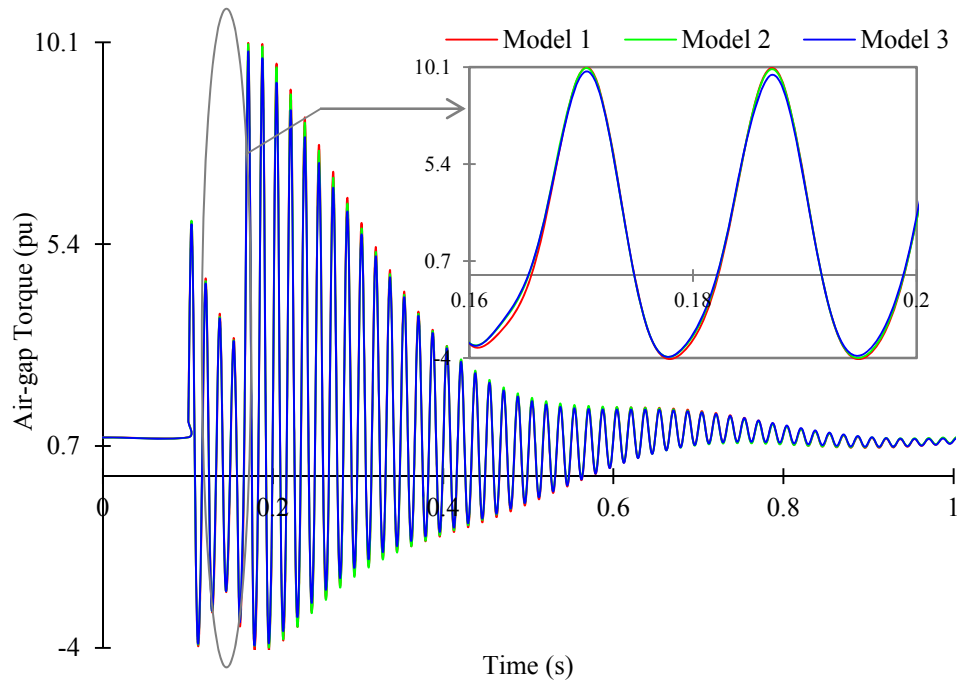
Fig. 6.7. Synchronous machine air-gap torque calculated by the three models.

The load angle graph is presented in Fig. 6.8. Since load angle is closely related to the quadrature axis reactance, there is a discrepancy between the load angle values at the steady-state and transient states as calculated by the different magnetization models. Fig. 6.9 shows the calculated phase 'a', 'b' and 'c' currents for synchronous machines for Model 3. Table 6.1 summarizes the peak-to-peak variations of the load angle, phase 'a' current, and air-gap torque calculated using the three magnetization models.
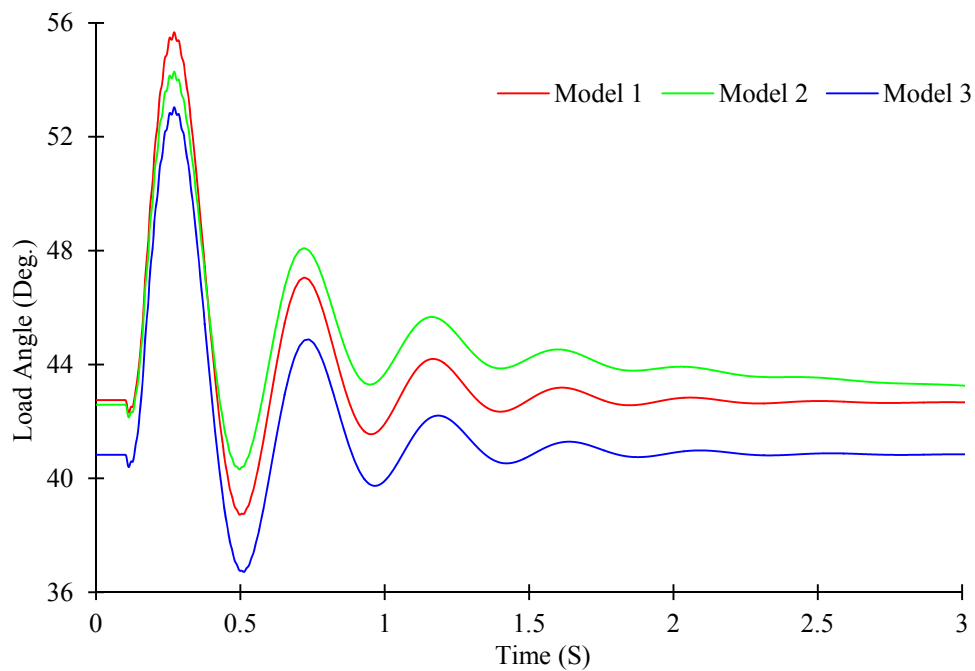
Fig. 6.8. Load angle calculated by the three models.
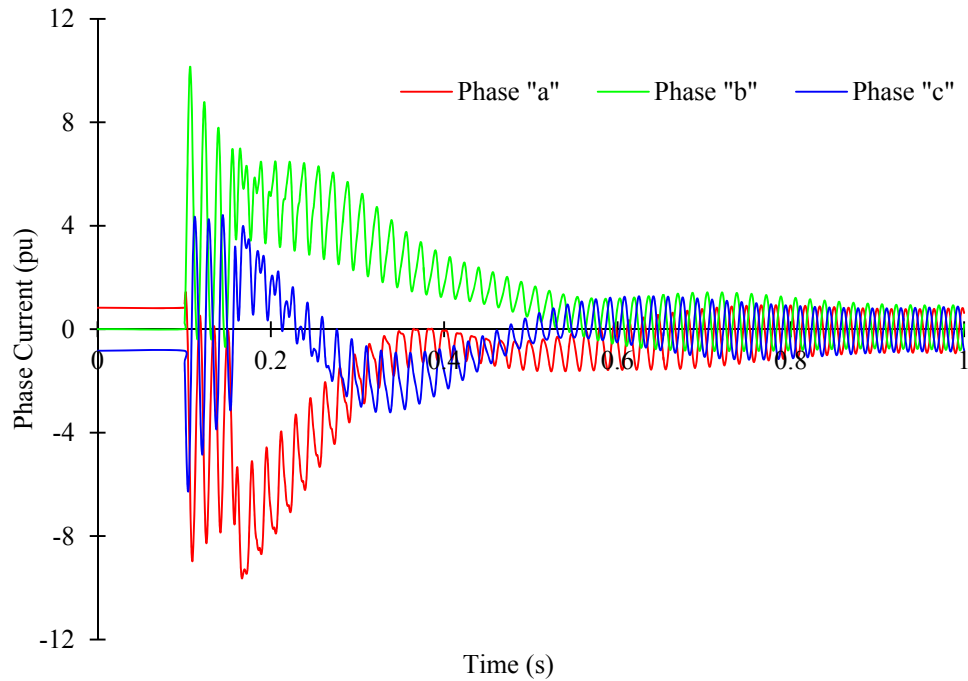
Fig. 6.9. Synchronous machine phase currents calculated using Model 3.

Table 6.1. The First Peak-To-Peak Values of Torque, Load Angle, and Phase Current Calculated by Employing AVR for Model 3.

	Model 1	Model 2	Model 3
Air-gap Torque	14.14 pu	14.05 pu	13.83 pu
Load Angle	16.95^o	14.45^o	18.00^o
Phase 'A' Current	11.10 pu	11.14 pu	11.08 pu

Figure 6.10 demonstrates the load angle response for marginally stable and the unstable cases calculated by the three models. Model 3 demonstrates that inclusion of magnetization increases the value of critical clearing time (CCT). In fact, this correlation between the magnetization and CCT has been proven in [58]. The effect of the synchronous machine magnetization on the machine critical clearing time is presented in Table 6.2 for

the three magnetization models. In the case of a saturated machine subjected to an inter-ruption, it can be seen that the use of AVR improves the critical clearing time. A qualita-tive analysis of the fault duration on the machine first peak air-gap torque is essential, because the machine is subjected to high air-gap torque both during the interruption and after its clearance.

The first peak air-gap torque as a function of the fault duration is presented in Fig. 6.11. It can be seen that for a fault duration of 8.33 ms, the maximum value of the air-gap torque is calculated to be 11.8 pu. Additionally, it can be seen that the frequency of the peak air-gap torque oscillation as a function of the fault duration is 60 Hz.
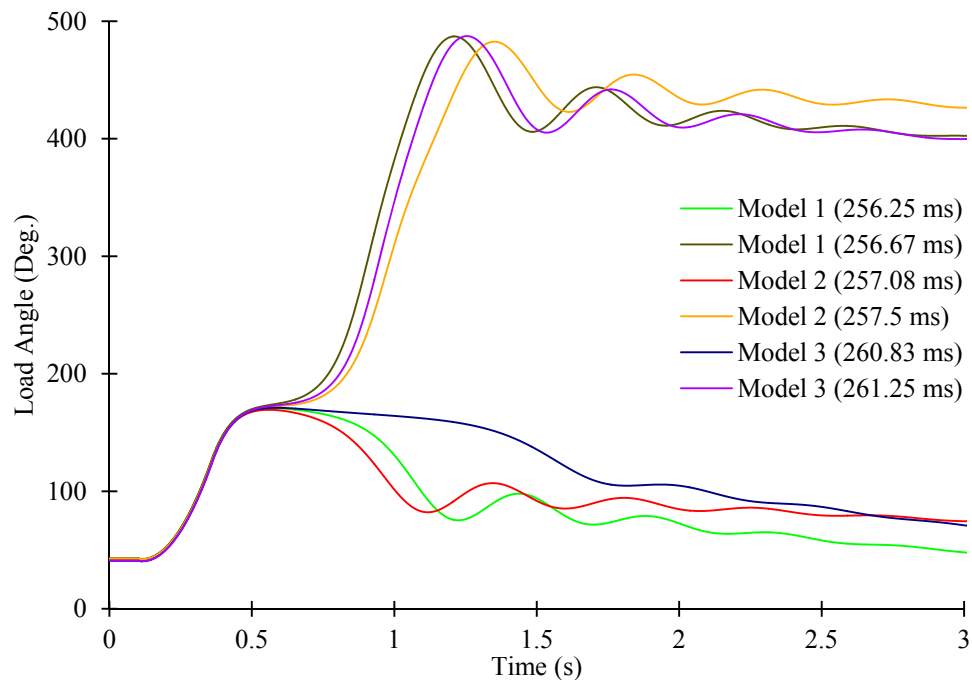
Fig. 6.10. Load angle response for marginally stable and unstable cases calculated by the three models.

Table 6.2. Critical Clearing Time for Different Magnetization Models With and Without AVR.

	Model 1	Model 2	Model 3
CCT (AVR)	256.25 ms	257.08 ms	260.83 ms
CCT (Without AVR)	254.58 ms	256.67 ms	257.92 ms

6.2.2. *Parameter Sensitivity Analysis Employing the Synchronous Generator Models*

The purpose of parameter sensitivity analysis is to ascertain the sensitivity of the synchronous machine stability characteristic when one or more of the machine parameters vary. The dynamic behaviour of the machine is analyzed by performing a series of tests with different parameter values. This method is beneficial to evaluate the robustness of the saturated machine model. It also leads to the construction of a confidence model through uncertainty investigations on the machine parameters. Although there are several

Fig. 6.11. Peak air-gap torque as a function of fault duration calculated by using Model 3.

ways to measure the synchronous machine parameters, it is not always possible to measure them with a high level of accuracy in practical applications. Moreover, the synchronous machines are always subjected to varying operating conditions and aging. The sensitivity analysis is advantageous because it enables the evaluation of the reliability and validity of the machine model and allows for a good estimate of the stability margin of the machine under fault [58]- [60].

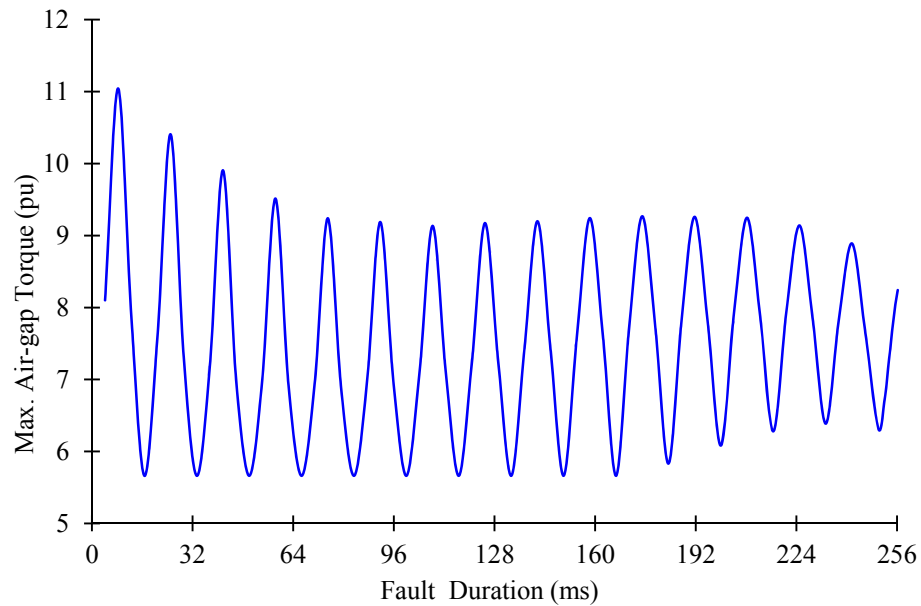The sensitivity of the load angle and air-gap torque oscillations with respect to a machine equivalent circuit parameter, $\aleph$, can be calculated by (6.10)

$$
\left.
\begin{aligned}
S_{\aleph}^{\delta} &= \frac{\partial \delta_{p-p}}{\partial \aleph} \times \left(\frac{\aleph}{\delta_{p-p}} \right) \\
S_{\aleph}^{\tau} &= \frac{\partial \tau_{p-p}}{\partial \aleph} \times \left(\frac{\aleph}{\tau_{p-p}} \right)
\end{aligned}
\right\}
\tag{6.10}
$$

where $\delta_{p\text{-}p}$ and $\tau_{p\text{-}p}$ are the peak-to-peak load angle and air-gap torque functions respectively. The effect of machine parameter variation on the load angle and the air-gap torque responses is investigated for an interruption duration of 58.33 ms. The parameters were varied from 25% to 175% of their standard values. Figs. 6.12 and 6.13 demonstrate the load angle and air-gap torque peak-to-peak sensitivity to all the machine parameters. It can be seen that variation of the armature leakage reactance significantly affects both the load angle and air-gap torque responses. The sensitivities of load angle and air-gap torque with respect to the machine parameters are calculated using (6.10) and listed in Table 6.3. As seen in this table, the machine is most sensitive to the variation of the leakage reactance and armature resistance.
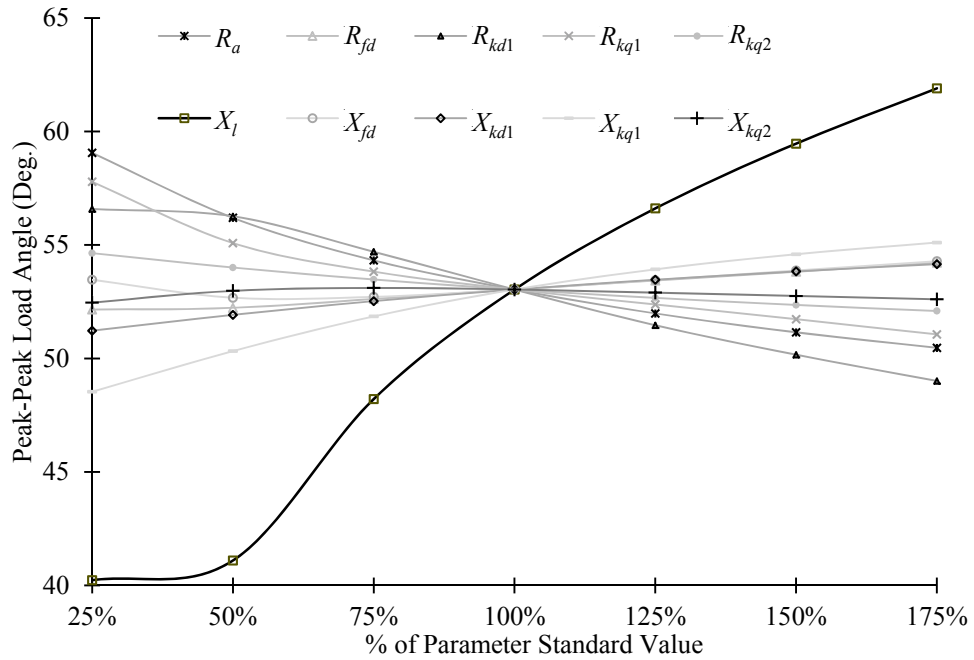
Fig. 6.12. Peak-to-peak load angle sensitivity as functions of different synchronous machine parameters calculated using Model 3.
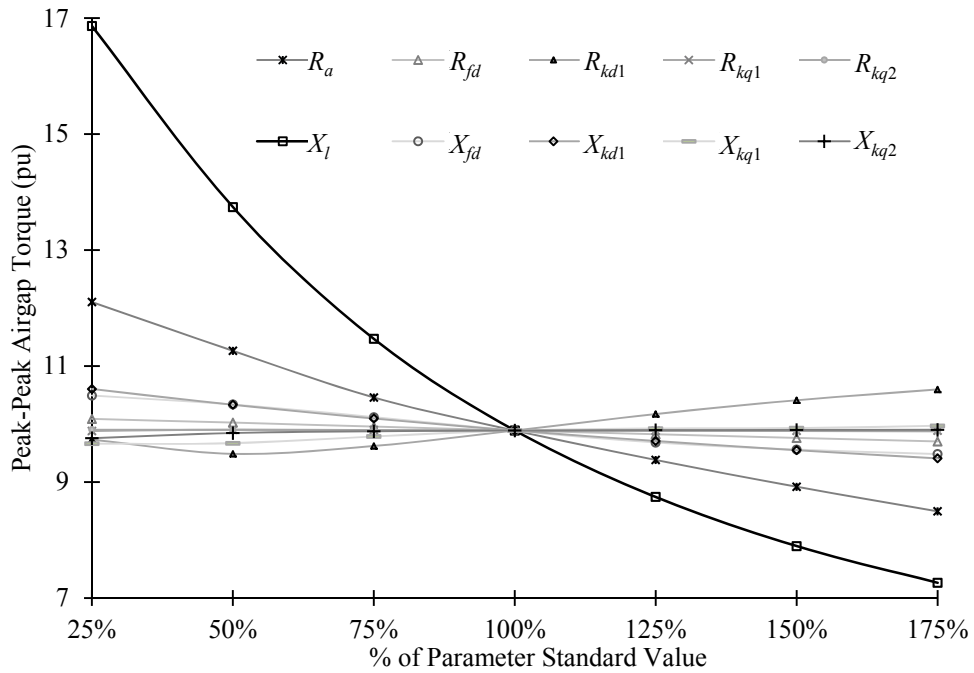
Fig. 6.13. Peak-to-peak air-gap torque sensitivity as functions of different synchronous machine parameters calculated using Model 3.

Table 6.3. Load Angle and Air-gap Torque Sensitivities with Respect
to the Variation in the Machine Parameters.

	S_N^δ	S_N^τ
X_l	0.27	0.65
R_a	0.11	0.24
X_{fd}	0.01	0.07
R_{fd}	0.03	0.01
X_{kd1}	0.04	0.07
R_{kd1}	0.10	0.06
X_{kq1}	0.08	0.03
R_{kq1}	0.08	0.02
X_{kq2}	0.001	0.009
R_{kq2}	0.03	0.01

6.2.3. *Harmonic Analysis on the Produced Air-gap Torque and Phase Current Responses by the Three Models*

As demonstrated in the previous sections, when a machine is subjected to a disturbance, there are impurities in the generator sinusoidal output. Thus, the machine terminal quantities are expected to be periodic and have harmonics. Since the synchronous machine is designed to work at the fundamental frequency of 60 Hz, it is detrimental for the generator to deliver power at the harmonics of its rated fundamental frequency. This may even reduce the life of the machine. Moreover, the harmonics in the machine response can cause the machine to operate inefficiently because they increase internal heating which increases the losses. Since hysteresis losses and eddy losses are function of the

frequency, the higher frequency creates more iron losses in the core. Copper losses also depend on frequency and lead to an increase in the internal temperature of the generator, which reduce its efficiency at the harmonic frequency. As a result, investigation on the harmonic spectrum of the machine during its transient operation is very significant [61]-[66].

To characterize the machine behavior after the occurrence of an interruption, the air-gap torque and phase current spectrums are decomposed using discrete Fourier analysis.

Since the air-gap torque or phase current oscillation is a non-stationary waveform and can only produce finite sequences, the discrete Fourier transform should be applied to obtain the harmonic spectrum. The discrete Fourier transformation for air-gap torque oscillations, τ, can be expressed as follows:

$$\mathcal{F}\{\tau(t)\} = \sum_{n=0}^{N-1} \tau(nT)e^{-j2\pi nk/N} \quad k = 0,..., N-1 \tag{6.11}$$

where N is the number of samples in the range of $[0, 2\pi]$ and T is the sampling interval.

The spectrums of the produced air-gap torque waveform for three machine models are presented in Fig. 6.14 for a fault duration of three and half cycles. It can be seen that the spectrum content of the waveform consists of the fundamental and the second harmonics. In Model 1, an amplitude of 349 dB was observed for the first harmonic, whereas for the second harmonic and DC, the amplitudes were 52 dB and 243 dB, respectively. The results also demonstrate that the magnetization affects the frequency of the air-gap torque oscillation due to the disturbance. The effect of fault duration on the harmonic

spectrum of the air-gap torque waveform is presented in Fig. 6.15. It can be seen that if the fault persists for the full number of cycles (four cycles in this case), the distribution of the harmonics in the harmonic spectrum does not change much in comparison to the ones for three and a half cycles, whereas the amplitude in the spectrum is much smaller. Harmonic spectrums of phase "a" current calculated by the three models are illustrated in Fig. 6.16 for fault duration of three and a half cycles. As seen in this figure, the amplitude at the second harmonic increases if magnetization is considered. Therefore, in the saturated machine subjected to an interruption, additional iron and copper losses are produced, which in turn cause the temperature in the synchronous machine to increase.

(a)

(b)

(c)

Fig. 6.14. Harmonic spectrum for the air-gap torque oscillations of the synchronous machine for fault duration of three and half cycles. (a) Model 1. (b) Model 2. (c) Model 3.

Fig. 6.15. Calculated air-gap torque harmonic spectrum of the synchronous machine by Model 3 for fault duration of four cycles. (a) Model 1. (b) Model 2. (c) Model 3.

(a)
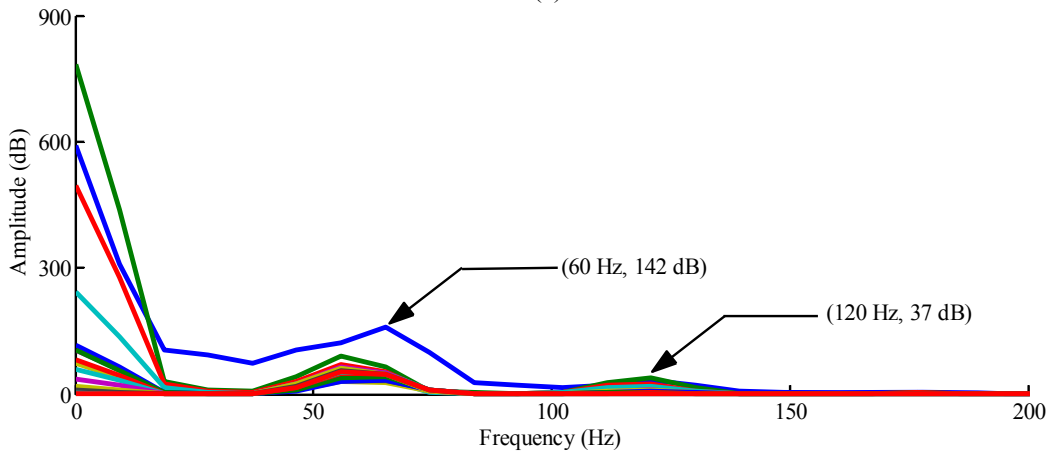
(b)
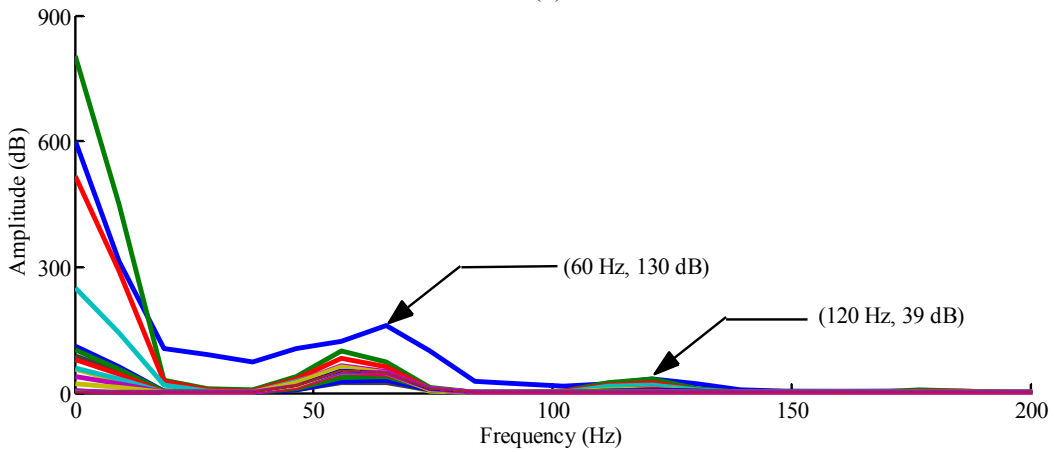
(c)
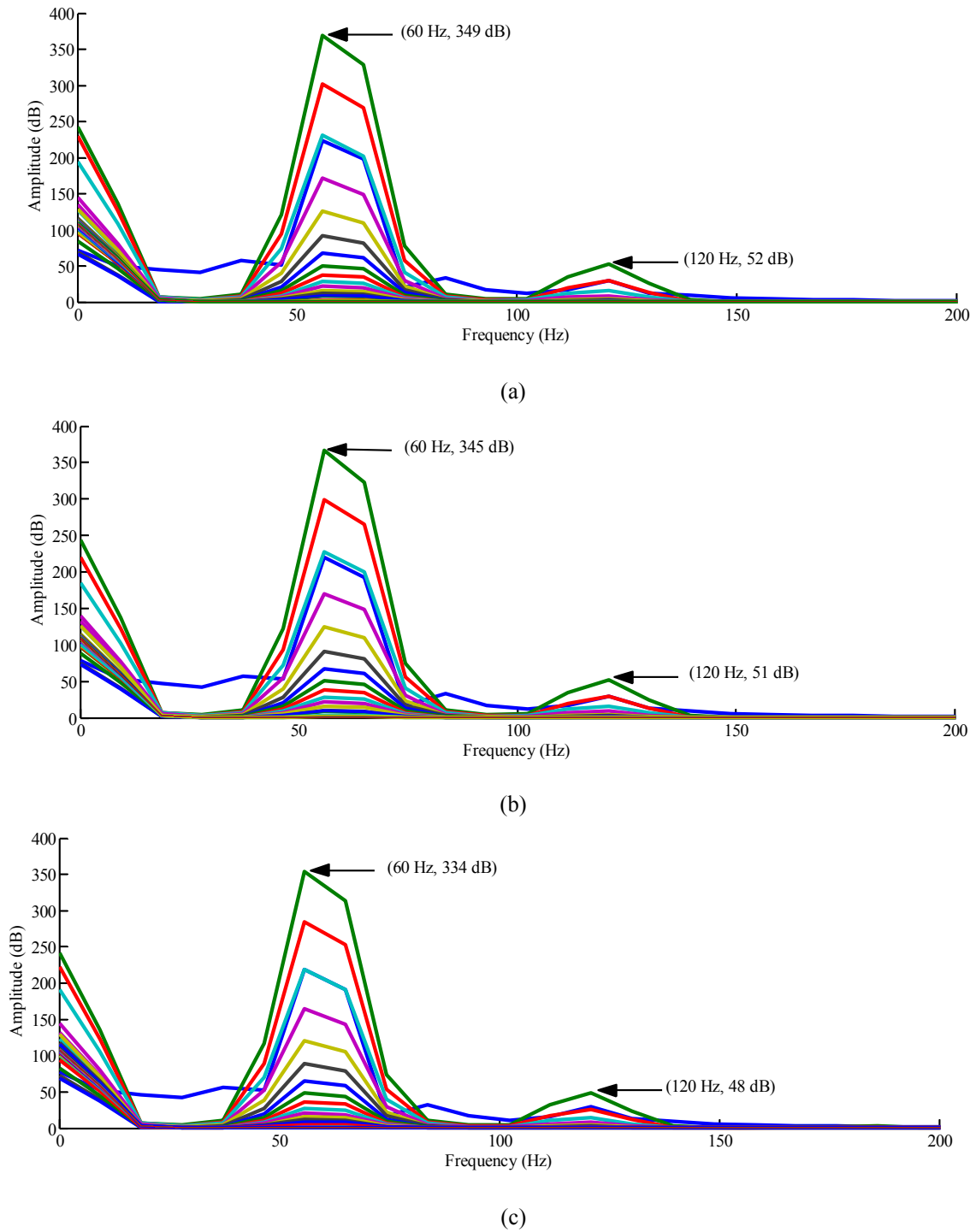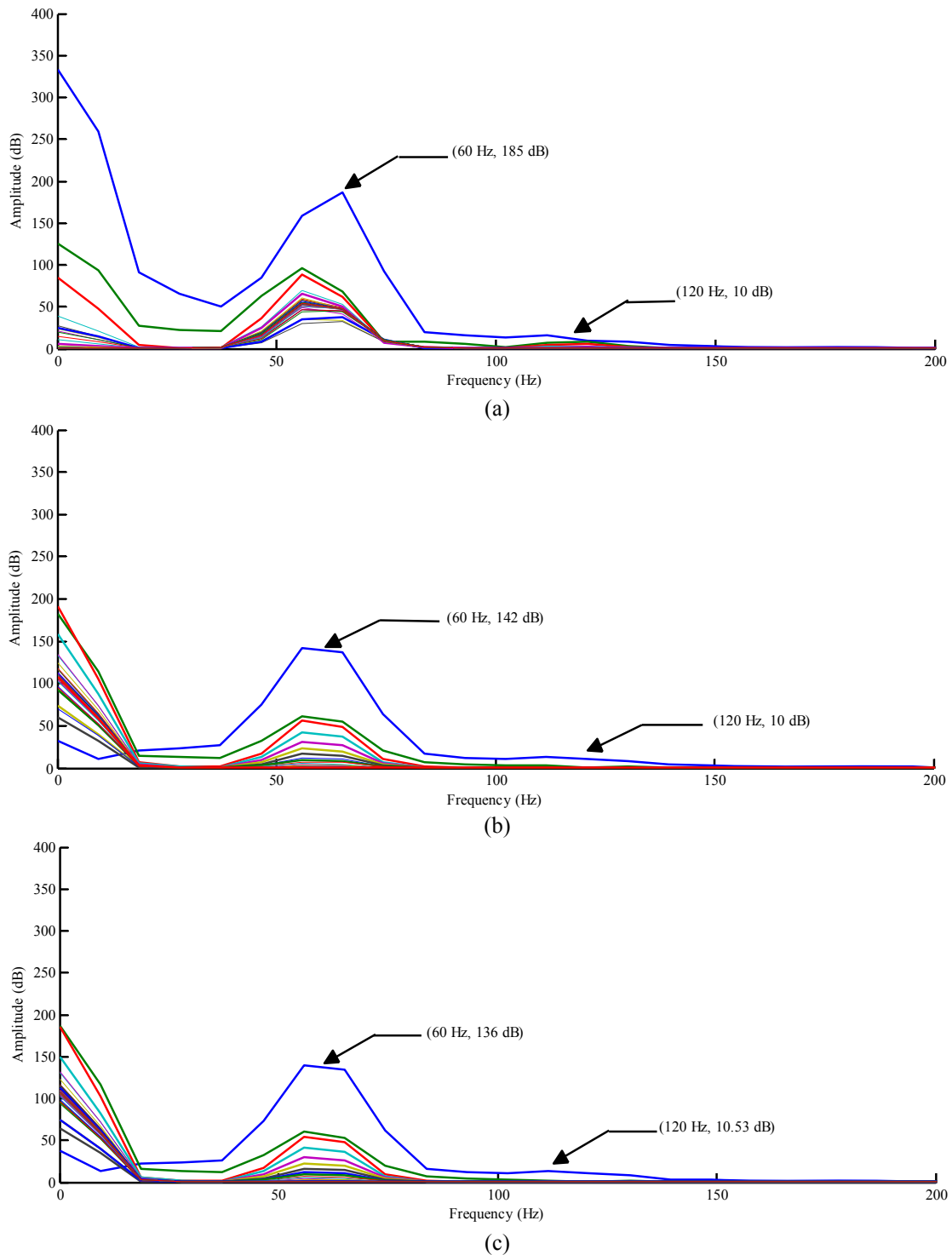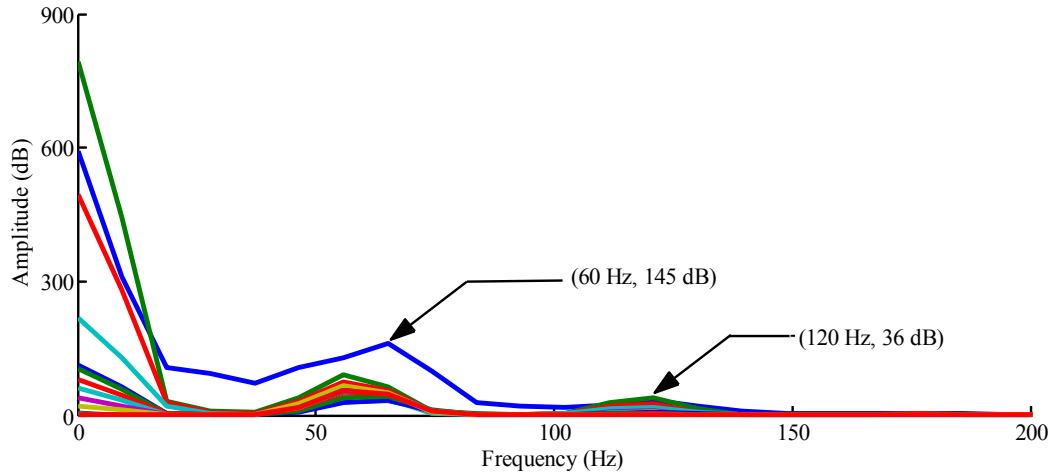
Fig. 6.16. Harmonic spectrum for phase 'a' current of the synchronous machine for fault duration of three and half cycles. (a) Model 1. (b) Model 2. (c) Model 3.

6.2.4. Time-Frequency Analysis of the Produced Air-gap Torque Response by the Three Models

In order to determine the time at which each specific harmonic of the air-gap torque oscillations occurs, time-frequency analysis has been performed in this section. Time-frequency analysis is very useful in time varying processes and can provide the spectrogram representation of the waveform. In this section, the short time Fourier transform (STFT), which is a discrete Fourier-based transform, is used to examine the frequency spectrogram of a produced time varying air-gap torque after the fault. In fact, in the STFT procedure, the air-gap torque information is divided into several frames using a moving window throughout the time, and the discrete Fourier analysis will be computed for each windowed section of the waveform. The STFT of a signal such as the air-gap torque oscillations of the machine, which is the waveform under investigation in this study, can be mathematically represented by (6.12)

$$\mathbf{STFT}\{\tau(n)\} = \mathrm{T}(m,\omega) = \sum_{n=-\infty}^{+\infty} W(n-m)\tau(n)e^{-j\omega n} \qquad (6.12)$$

where $\mathrm{T}(m,\omega)$ is the discrete Fourier transform of the windowed air-gap torque oscillation, W is the window function and m and ω are time and frequency respectively [67], [68].

Since the STFT is just a computation of the discrete Fourier transform on the windowed waveform, the short time Fourier transform of the torque oscillation is significantly affected by the kind and duration of the window. Therefore, there is always trade-off

between time and frequency resolution. In this analysis, the 240-point window used in the STFT implementations is the Hamming window with a 50% overlap between the sections, number of FFT points used to calculate DFT (nfft) is 256, and the sampling rate is 42 ms.

Fig. 6.17 shows the time-frequency spectrogram of the produced air-gap torque of the synchronous machine for the short-circuit duration of 58.33 ms calculated for the three machine models. This figure illustrates that three major harmonics in the oscillating air-gap torque mostly occur during the first 250 ms. Moreover, the discrepancies between the results calculated by three magnetization cases are significant.
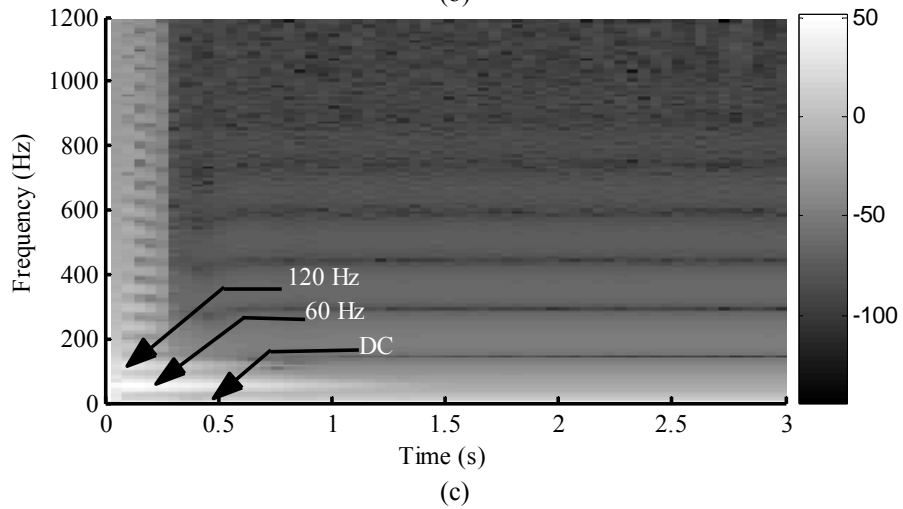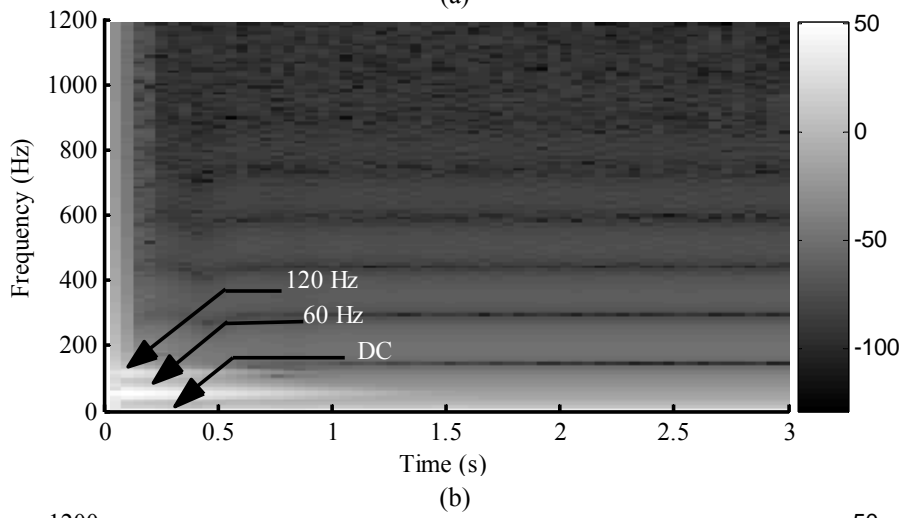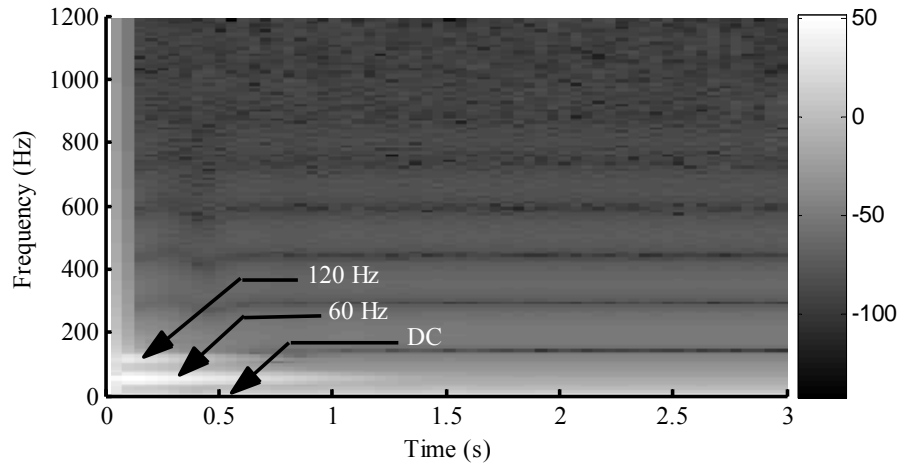
Fig. 6.17. Time-frequency spectrogram of the air-gap torque waveform. (a) Model 1. (b) Model 2. (c) Model 3

6.3. Conclusion

The trigonometric magnetization model developed in chapter 3 has been applied to the conventional synchronous machine model. Extensive transient stability analysis in time-frequency domain has been performed under a three-phase short circuit condition. The numerical analyses results employing the three saturated synchronous machine models demonstrate that magnetization significantly affects the transient performance of synchronous machines.

The work developed in this chapter has been published in IEEE Transactions on Energy Conversion [45].

Chapter 7

Conclusions and Future Work

7.1. Conclusions

In this dissertation, two effective techniques to represent magnetization phenomenon in electrical machines have been proposed.

The first method developed in this research was based on a trigonometric algorithm. The implemented magnetization models for particular electric machines are examined by conducting several numerical investigations. Based on these results, it was concluded that this model is privileged for magnetization modeling of electrical machines for its accuracy and reliability. Therefore, this model was integrated into a synchronous machine model. Transient analysis of synchronous machines in case of short circuit faults was per-

formed using the Lambton synchronous generator parameters. Then, the impact of the d-and q-axis magnetization on the machine performance was studied.

It was demonstrated that the second method proposed in this research is very accurate and modifiable. Inasmuch as the algorithm is not developed reliantly on a particular expression, researchers can adjust it according to many different possible functional expressions provided that they satisfy some basic rules. The accuracy of this method has also been verified by performing numerical analyses on magnetization characteristics of a synchronous machine and a permanent magnet synchronous machine for different configurations.

To realize the effect of magnetization in steady-state performance of synchronous machines, the LM model has been incorporated into a state space synchronous machine. Furthermore, the model was used in steady-state performance analyses on the Lambton synchronous machine.

7.2. Suggestions for Future Work

Inclusion of magnetization in performance analysis of synchronous machines has a significant effect on the accuracy of the results obtained in through the numerical investigations. Therefore, as the next step for this research, universal synchronous machine software incorporated with the proposed magnetization models can be implemented. This model can be utilized for both transient and steady-state analyses of synchronous machines.

Additionally, more investigations can be carried out by doing some experimental procedures to re-examine the efficiency of the model.

Finally, the magnetization models proposed in this research can be applied to represent magnetization phenomenon for other kinds of electrical machines as well. Therefore, comprehensive electrical machine models including magnetization can be obtained.

References

[1]   P. Kundur, *Power System Stability and Control*. New York: McGraw-Hill, 1994.

[2]   N. C. Kar and A. M. El-Serafi, "Effect of voltage sag on the transient performance of saturated synchronous motors," in *Proc. Canadian Conference on Electrical and Computer Engineering, 2006. CCECE '06.*, 2006, pp. 1246-1251.

[3]   A. M. El-Serafi and N. C. Kar, "Effect of voltage sag duration on the air-gap magnetic flux patterns and peak electromagnetic torques in saturated synchronous motors," in *Proc. 18th International Conference on Electrical Machines, 2008. ICEM 2008.* 2008, pp. 1-6.

[4]   R. G. Harley*, et al.*, "Comparative study of saturation methods in synchronous machine models," *IEE Proceedings on Electric Power Applications,* vol. 127, pp. 1-7, 1980.

[5]   S. Guha and N. C. Kar, "Saturation modeling and stability analysis of synchronous reluctance generator," *IEEE Transactions on Energy Conversion,* vol. 23, pp. 814-823, 2008.

[6]   D. C. Aliprantis*, et al.*, "Experimental characterization procedure for a synchronous machine model with saturation and arbitrary rotor network representation," *IEEE Transactions on Energy Conversion,* vol. 20, pp. 595-603, 2005.

[7]   S. H. Minnich*, et al.*, "Saturation functions for synchronous generators from finite elements," *IEEE Transactions on Energy Conversion,* vol. EC-2, pp. 680-692, 1987.

[8]   F. P. de Mello and L. N. Hannett, "Representation of saturation in synchronous machines," *Power Engineering Review, IEEE,* vol. PER-6, pp. 24-25, 1986.

[9]   T. Xiaoping, *et al.*, "Transient modeling of squirrel-cage induction machine considering air-gap flux saturation harmonics," *IEEE Trans. on Industrial Electronics,* vol. 55, pp. 2798-2809, 2008.

[10]   I. Iglesias*, et al.*, "A d-q model for the self-commutated synchronous machine considering the effects of magnetic saturation," *IEEE Trans. on Energy Conversion,* vol. 7, pp. 768-776, 1992.

[11]   M. R. Smith, "Regression , differentiation, data smoothing, and least squares fit to data with decreased computational overhead," *IEEE Transactions on Industrial Electronics,* vol. IE-32, pp. 135-141, 1985.

[12]   L. Kaiyuan and E. Ritchie, "Torque analysis with saturation effects for non-salient single-phase permanent-magnet machines," *IEEE Transactions on Magnetics,* vol. 47, pp. 1732-1738, 2011.

[13]   J. Rivas*, et al.*, "Simple approximation for magnetization curves and hysteresis loops," *IEEE Transactions on Magnetics,* vol. 17, pp. 1498-1502, 1981.

[14]   D. C. Aliprantis*, et al.*, "A synchronous machine model with saturation and arbitrary rotor network representation," *IEEE Transactions on Energy Conversion,* vol. 20, pp. 584-594, 2005.

[15]   M. O. Mahmoud and R. W. Whitehead, "Piecewise fitting function for magnetisation characteristics," *Power Engineering Review, IEEE,* vol. PER-5, pp. 48-49, 1985.

[16]   E. Levi, "A unified approach to main flux saturation modelling in D-Q axis models of induction machines," *IEEE Transactions on Energy Conversion,* vol. 10, pp. 455-461, 1995.

[17]   A. Barili*, et al.*, "A simulation model for the saturable reactor," *IEEE Transactions on Industrial Electronics,* vol. 35, pp. 301-306, 1988.

[18]   K. A. Corzine*, et al.*, "An improved method for incorporating magnetic saturation in the q-d

synchronous machine model," *IEEE Trans. on Energy Conversion,* vol. 13, pp. 270-275, 1998.

[19]   C. Perez-Rojas, "Fitting saturation and hysteresis via arctangent functions," *IEEE Power Engineering Review,* vol. 20, pp. 55-57, 2000.

[20]   F. Wang, "A nonlinear saturation model for salient-pole synchronous machines in high performance drive applications," in *Proc. Annual Meeting. Conference Record of the Industry Applications Conference, 2003. 38th IAS*, 2003, pp. 906-910 vol.2.

[21]   B. Kawkabani*, et al.*, "Combined analytical-numerical approach for the modeling and analysis of three-phase transformers," in *Proc. 32nd Annual Conference on IEEE Industrial Electronics, IECON 2006 -*, 2006, pp. 1521-1526.

[22]   B. Kawkabani and J.-J. Simond, "Improved modeling of three-phase transformer analysis based on non-linear B-H curve and taking into account zero-sequence flux," in *Proc. Spring Monograph on Recent Development of Elec. Drives-ICEM'04*, 2006, pp. 451-469.

[23]   L. Guanghao and X. Xiao-Bang, "Improved modeling of the nonlinear B-H curve and its application in power cable analysis," *IEEE Trans. on Magnetics,* vol. 38, pp. 1759-1763, 2002.

[24]   S. Kansal and G. Cook, "Use of a sinusoidal series for modeling discrete windowed data as an alternative to regression ," *IEEE Trans. on Industrial Electronics,* vol. 51, pp. 903-909, 2004.

[25]   S. A. Tahan and I. Kamwa, "A two-factor saturation model for synchronous machines with multiple rotor circuits," *IEEE Transactions on Energy Conversion,* vol. 10, pp. 609-616, 1995.

[26]   O. Rodriguez and A. Medina, "Fast periodic steady state solution of a synchronous machine model in phase coordinates incorporating the effects of magnetic saturation and hysteresis," in *Power*

Engineering Society Winter Meeting, 2001. IEEE, 2001, pp. 1431-1436 vol.3.

[27] A. B. Dehkordi*, et al.*, "Development and validation of a comprehensive synchronous machine model for a real-time environment," *IEEE Trans. on Energy Conversion,* vol. 25, pp. 34-48, 2010.

[28] R. H. Park, "Two-reaction theory of synchronous machines generalized method of analysis-part I," *Transactions of the American Institute of Electrical Engineers,* vol. 48, pp. 716-727, 1929.

[29] P. M. Anderson and A. A. Fouad, *Power System Control and Stability*, 2nd ed. New York: John Wiley and Sons, 2003.

[30] N. D. Tleis, *Power Systems Modelling and Fault Analysis*: Elsevier Ltd., 2008.

[31] J. Das, *Power system analysis: short-circuit load flow and harmonics* vol. 16: CRC, 2002.

[32] W. H. Press, *Numerical Recipes in FORTRAN: The Art of Scientific Computing* vol. 1: Cambridge Univ Pr, 1992.

[33] B. P. Flannery*, et al.*, *Numerical recipes in C*, Press Syndicate of the University of Cambridge, New York, 1992.

[34] D. Rossiter, "Introduction to the R project for statistical computing for use at ITC," *International Institute for Geo-information Science & Earth Observation (ITC), Enschede (NL),* vol. 2, 2010.

[35] D. Rossiter, "Technical Note: Fitting rational functions to time series in R," ed: Enschede (NL): International Institute for Geo-information Science & Earth Observation (ITC) URL http://www. itc. nl/personal/rossiter/teach/R/R_rat. pdf, 2005.

[36] C. Collomb, "A tutorial on trigonometric curve fitting," [online]

Available:http://ccollomb.free.fr/technotes/A.tutorial on trigonometriv curve fitting, 2007.

[37]   B. J. Millard, *Channels & Cycles: A Tribute to J.M. Hurst* vol. 1. USA: Traders Press Inc, 1999.

[38]   P. L. Dandeno*, et al.*, "Validation of turbogenerator stability models by comparisons with power system tests," *Power Engineering Review, IEEE,* vol. PER-1, pp. 36-36, 1981.

[39]   "Determination of Synchronous machine Stability Study Constants," Ontario Hydro Toronto, ON, Canada1989.

[40]   H. Jabr, "Doubly-fed induction generator used in wind power," Ph.D. dissertation, Dept. of Electrical Engineering, University of Windsor, Windsor, ON, 2008.

[41]   A. M. El-Serafi and N. C. Kar, "Methods for determining the q-axis saturation characteristics of salient-pole synchronous machines from the measured d-axis characteristics," *Power Engineering Review, IEEE,* vol. 22, pp. 57-57, 2002.

[42]   N. C. Kar and A. M. El-Serafi, "Measurement of the saturation characteristics in the quadrature axis of synchronous machines," *IEEE Trans. on Energy Conversion,* vol. 21, pp. 690-698, 2006.

[43]   A. M. El-Serafi and N. C. Kar, "Methods for determining the intermediate-axis saturation characteristics of salient-pole synchronous machines from the measured d-axis characteristics," *IEEE Transactions on Energy Conversion,* vol. 20, pp. 88-97, 2005.

[44]   S. Hamidifar and N. C. Kar, "A trigonometric technique for characterizing magnetic saturation in electrical machines," in *Proc. 2010 XIX International Conference on Electrical Machines (ICEM),* 2010, pp. 1-6.

[45]   S. Hamidifar and N. C. Kar, "A novel approach to saturation characteristics modeling and its

impact on synchronous machine transient stability analysis," *IEEE Transactions on Energy Conversion,* vol. 27, pp. 139-150, 2012.

[46]   C. T. Kelley, *Iterative Methods for Optimization*. SIAM: Philadelphia, 1999.

[47]   S. S. Rao and S. Rao, *Engineering Optimization: Theory and Practice*: Wiley, 2009.

[48]   G. V. Reklaitis*, et al.*, *Engineering Optimization- Methods and Applications*. New York: John Wiley and Sons, 1983.

[49]   G. A. Korn and T. M. Korn, *Mathematical Handbook for Scientists and Engineers: Definitions, Theorems, and Formulas for Reference and Review*: Dover Pubns, 2000.

[50]   S. Hamidifar*, et al.*, "A novel method to represent the saturation characteristics of PMSM using Levenberg-Marquardt algorithm," in *2011 IEEE Vehicle Power and Propulsion Conference (VPPC),* 2011, pp. 1-6.

[51]   S. Hamidifar and N. C. Kar, "A state space synchronous machine model with multifunctional characterization of saturation using levenberg-marquardt optimization algorithm,"Submitted to *IEEE Transactions on Energy Conversion,* 2012.

[52]   W. L. Rugh, *Linear System Theory*, 2nd ed.: Prentice-Hall, Inc., 1996.

[53]   J. A. Hollman and J. R. marti, "step-by-step eigenvalue analysis with EMTP discrete-time solutions," *IEEE Transactions on Power Systems,* vol. 25, pp. 1220-1231, 2010.

[54]   "IEEE Guide for Synchronous Generator Modeling Practices and Applications in Power System Stability Analyses," *IEEE Std 1110-2002 (Revision of IEEE Std 1110-1991),* pp. 0_1-72, 2003.

[55] P. S. R. Murty, *Operation and Control in Power Systems*, 2nd ed.: CRC Press, 2011.

[56] J. B. X. Devotta, "A dynamic model of the synchronous generator excitation control system," *IEEE Transactions on Industrial Electronics,* vol. IE-34, pp. 429-432, 1987.

[57] "IEEE Recommended Practice for Excitation System Models for Power System Stability Studies," *IEEE Std 421.5-2005 (Revision of IEEE Std 421.5-1992),* pp. 0_1-85, 2006.

[58] N. C. Kar*, et al.*, "A new method to evaluate the q-axis saturation characteristics of cylindrical-rotor synchronous generator," *IEEE Trans. on Energy Conversion,* vol. 15, pp. 269-276, 2000.

[59] Z. Dong*, et al.*, "Power system sensitivity analysis considering induction motor loads," in *Proc. 8th International Conference on Advances in Power System Control, Operation and Management (APSCOM 2009),* 2009, pp. 1-6.

[60] J. Chureemart and P. Churueang, "Sensitivity analysis and its applications in power system improvements," in *Proc. 5th International Conf. on Electrical Engineering/Electronics, Computer, Telecommunications and Information Technology, 2008. ECTI-CON 2008.,* 2008, pp. 945-948.

[61] Z. Gmyrek*, et al.*, "Iron loss prediction with pwm supply using low- and high-frequency measurements: analysis and results comparison," *IEEE Transactions on Industrial Electronics,* vol. 55, pp. 1722-1728, 2008.

[62] Z. Gmyrek*, et al.*, "Estimation of iron losses in induction motors: calculation method, results, and analysis," *IEEE Transactions on Industrial Electronics,* vol. 57, pp. 161-171, 2010.

[63] T. H. Ortmeyer*, et al.*, "The effects of power system harmonics on power system equipment and loads," *Power Engineering Review, IEEE,* vol. PER-5, pp. 54-54, 1985.

[64]   "IEEE Recommended Practices and Requirements for Harmonic Control in Electrical Power Systems," *IEEE Std 519-1992,* p. 0_1, 1993.

[65]   Z. Leonowicz*, et al.*, "Advanced spectrum estimation methods for signal analysis in power electronics," *IEEE Transactions on Industrial Electronics,* vol. 50, pp. 514-519, 2003.

[66]   G. W. Chang*, et al.*, "A Two-Stage ADALINE for Harmonics and Interharmonics Measurement," *IEEE Transactions on Industrial Electronics,* vol. 56, pp. 2220-2228, 2009.

[67]   L. Coppola*, et al.*, "Wavelet transform as an alternative to the short-time fourier transform for the study of conducted noise in power electronics," *IEEE Transactions on Industrial Electronics, IEEE* vol. 55, pp. 880-887, 2008.

[68]   E. G. Strangas*, et al.*, "Time-frequency analysis for efficient fault diagnosis and failure prognosis for interior permanent-magnet AC motors," *IEEE Transactions on Industrial Electronics,* vol. 55, pp. 4191-4199, 2008.

Appendix A

Electrical Machines Ratings and Specifications

The Specifications and ratings for the different electrical machines used in the investigations in this research are presented here.

A.1. Nanticoke Synchronous Generator

The Nanticoke synchronous generator is a two pole 588 MVA non-salient pole synchronous machine on the Ontario Hydro System. The ratings are listed in Table A.1.

Table A.1. The Nanticoke Synchronous Machine Ratings

Machine Rating	
Rated Power	588 MVA
Rated Voltage	22 kV
Rated Frequency	60 Hz
Rated Power Factor	0.85
Rated Speed	3,600 rpm

A.2. Lambton Synchronous Generator

The Lambton synchronous generator is a two pole 555 MVA non-salient pole synchronous machine the Ontario Hydro system. The rating and parameter specification used in the investigations are presented in Table A.2 and Table A.3, respectively.

Table A.2. The Lambton Synchronous Machine Ratings

Machine Rating	
Rated Power	555 MVA
Rated Voltage	22.8 kV
Rated Frequency	60 Hz
Rated Power Factor	0.90
Rated Speed	3,600 rpm

Table A.3. The Lambton Synchronous Machine Parameters

Machine Parameters	
$X_{md} = 1.97$pu	$R_a = 0.003$ pu
$X_{mq} = 1.867$ pu	$X_l = 0.160$ pu
$R_{fd} = 0.0012$ pu	$R_{kd1} = 0.0109$ pu
$X_{fd} = 0.1171$ pu	$X_{kd1} = 0.0174$ pu
$R_{kq1} = 0.0164$ pu	$R_{kq2} = 0.0099$ pu
$X_{kq1} = 0.0638$ pu	$X_{kq2} = 0.3833$ pu

A.3. Doubly Fed Induction Generator

The machine ratings for a laboratory doubly fed induction generator are shown in Table A.4.

Table A.4. The DFIG Ratings

Machine Rating	
Rated Power	2.78 kVA
Rated Voltage	208 V
Rated Frequency	60 Hz
Rated Power Factor	0.72
Rated Speed	1,720 rpm

A.4. Permanent Synchronous Machine

The rating information for the laboratory surface mounted Permanent Magnet Synchronous Machine (PMSM) of Siemens is listed in Table A.5.

Table A.5. The PMSM Ratings

Machine Rating	
Rated Power	21 hp
Rated Motor Voltage	297V
Rated Motor Current	35 A
Rated Motor Speed	3000 r/min
Number of Pole	8
Moment of Inertia	0.0168 kgm²
Maximum Motor Current	155 A

Appendix B

IEEE Permission Grant on Reusing the Published Papers

Copyright Clearance Center

RightsLink®

Home | Create Account | Help

IEEE
Requesting permission to reuse content from an IEEE publication

Title: A Novel Approach to Saturation Characteristics Modeling and Its Impact on Synchronous Machine Transient Stability Analysis
Author: Hamidifar, S.; Kar, N.C.
Publication: Energy Conversion, IEEE Transactions on
Publisher: IEEE
Date: March 2012
Copyright © 2012, IEEE

User ID

Password

☐ Enable Auto Login

LOGIN

Forgot Password/User ID?

If you're a copyright.com user, you can login to RightsLink using your copyright.com credentials. Already a **RightsLink user** or want to learn more?

Thesis / Dissertation Reuse

The IEEE does not require individuals working on a thesis to obtain a formal reuse license, however, you may print out this statement to be used as a permission grant:

Requirements to be followed when using any portion (e.g., figure, graph, table, or textual material) of an IEEE copyrighted paper in a thesis:

1) In the case of textual material (e.g., using short quotes or referring to the work within these papers) users must give full credit to the original source (author, paper, publication) followed by the IEEE copyright line © 2011 IEEE.
2) In the case of illustrations or tabular material, we require that the copyright line © [Year of original publication] IEEE appear prominently with each reprinted figure and/or table.
3) If a substantial portion of the original paper is to be used, and if you are not the senior author, also obtain the senior author's approval.

Requirements to be followed when using an entire IEEE copyrighted paper in a thesis:

1) The following IEEE copyright/ credit notice should be placed prominently in the references: © [year of original publication] IEEE. Reprinted, with permission, from [author names, paper title, IEEE publication title, and month/year of publication]
2) Only the accepted version of an IEEE copyrighted paper can be used when posting the paper or your thesis on-line.
3) In placing the thesis on the author's university website, please display the following message in a prominent place on the website: In reference to IEEE copyrighted material which is used with permission in this thesis, the IEEE does not endorse any of [university/educational entity's name goes here]'s products or services. Internal or personal use of this material is permitted. If interested in reprinting/republishing IEEE copyrighted material for advertising or promotional purposes or for creating new collective works for resale or redistribution, please go to http://www.ieee.org/publications_standards/publications/rights/rights_link.html to learn how to obtain a License from RightsLink.

If applicable, University Microfilms and/or ProQuest Library, or the Archives of Canada may supply single copies of the dissertation.

BACK | CLOSE WINDOW

Copyright Clearance Center

RightsLink®

Home | Create Account | Help

IEEE Requesting permission to reuse content from an IEEE publication

Title: A trigonometric technique for characterizing magnetic saturation in electrical machines

Conference Proceedings: Electrical Machines (ICEM), 2010 XIX International Conference on

Author: Hamidifar, S.; Kar, N.C.

Publisher: IEEE

Date: 6-8 Sept. 2010

Copyright © 2010, IEEE

User ID

Password

☐ Enable Auto Login

LOGIN

Forgot Password/User ID?

If you're a copyright.com user, you can login to RightsLink using your copyright.com credentials. Already **a RightsLink user** or want to learn more?

Thesis / Dissertation Reuse

The IEEE does not require individuals working on a thesis to obtain a formal reuse license, however, you may print out this statement to be used as a permission grant:

Requirements to be followed when using any portion (e.g., figure, graph, table, or textual material) of an IEEE copyrighted paper in a thesis:

1) In the case of textual material (e.g., using short quotes or referring to the work within these papers) users must give full credit to the original source (author, paper, publication) followed by the IEEE copyright line © 2011 IEEE.
2) In the case of illustrations or tabular material, we require that the copyright line © [Year of original publication] IEEE appear prominently with each reprinted figure and/or table.
3) If a substantial portion of the original paper is to be used, and if you are not the senior author, also obtain the senior author's approval.

Requirements to be followed when using an entire IEEE copyrighted paper in a thesis:

1) The following IEEE copyright/ credit notice should be placed prominently in the references: © [year of original publication] IEEE. Reprinted, with permission, from [author names, paper title, IEEE publication title, and month/year of publication]
2) Only the accepted version of an IEEE copyrighted paper can be used when posting the paper or your thesis on-line.
3) In placing the thesis on the author's university website, please display the following message in a prominent place on the website: In reference to IEEE copyrighted material which is used with permission in this thesis, the IEEE does not endorse any of [university/educational entity's name goes here]'s products or services. Internal or personal use of this material is permitted. If interested in reprinting/republishing IEEE copyrighted material for advertising or promotional purposes or for creating new collective works for resale or redistribution, please go to http://www.ieee.org/publications_standards/publications/rights/rights_link.html to learn how to obtain a License from RightsLink.

If applicable, University Microfilms and/or ProQuest Library, or the Archives of Canada may supply single copies of the dissertation.

BACK | CLOSE WINDOW

Copyright Clearance Center

RightsLink®

Home | Create Account | Help

IEEE
Requesting permission to reuse content from an IEEE publication

Title: A novel method to represent the saturation characteristics of PMSM using Levenberg-Marquardt algorithm

Conference Proceedings: Vehicle Power and Propulsion Conference (VPPC), 2011 IEEE

Author: Hamidifar, S.; Kazerooni, M.; Kar, N.C.

Publisher: IEEE

Date: 6-9 Sept. 2011

Copyright © 2011, IEEE

User ID
_____

Password
_____

☐ Enable Auto Login

LOGIN

Forgot Password/User ID?

If you're a copyright.com user, you can login to RightsLink using your copyright.com credentials. Already **a RightsLink user** or want to learn more?

Thesis / Dissertation Reuse

The IEEE does not require individuals working on a thesis to obtain a formal reuse license, however, you may print out this statement to be used as a permission grant:

Requirements to be followed when using any portion (e.g., figure, graph, table, or textual material) of an IEEE copyrighted paper in a thesis:

1) In the case of textual material (e.g., using short quotes or referring to the work within these papers) users must give full credit to the original source (author, paper, publication) followed by the IEEE copyright line © 2011 IEEE.
2) In the case of illustrations or tabular material, we require that the copyright line © [Year of original publication] IEEE appear prominently with each reprinted figure and/or table.
3) If a substantial portion of the original paper is to be used, and if you are not the senior author, also obtain the senior author's approval.

Requirements to be followed when using an entire IEEE copyrighted paper in a thesis:

1) The following IEEE copyright/ credit notice should be placed prominently in the references: © [year of original publication] IEEE. Reprinted, with permission, from [author names, paper title, IEEE publication title, and month/year of publication]
2) Only the accepted version of an IEEE copyrighted paper can be used when posting the paper or your thesis on-line.
3) In placing the thesis on the author's university website, please display the following message in a prominent place on the website: In reference to IEEE copyrighted material which is used with permission in this thesis, the IEEE does not endorse any of [university/educational entity's name goes here]'s products or services. Internal or personal use of this material is permitted. If interested in reprinting/republishing IEEE copyrighted material for advertising or promotional purposes or for creating new collective works for resale or redistribution, please go to http://www.ieee.org/publications_standards/publications/rights/rights_link.html to learn how to obtain a License from RightsLink.

If applicable, University Microfilms and/or ProQuest Library, or the Archives of Canada may supply single copies of the dissertation.

BACK | CLOSE WINDOW

Vita Auctoris

Saeedeh Hamidifar was born in Ghazvin, Iran in 1979. She obtained her B.A.Sc. degree in electrical engineering from the Amirkabir University, Tehran, Iran in 2002, and the M.A.Sc. degree from the Iran University of Science and Technology, Tehran, Iran, in 2006. She is currently pursuing the Ph.D. degree in the department of electrical and computer engineering at University of Windsor, Windsor, Canada. Her research interests include synchronous machine steady state and transient performance analysis.

List of Publications

[1]   S. Hamidifar and N. C. Kar, "A Novel Approach to Saturation Characteristics Modeling and Its Impact on Synchronous Machine Transient Stability Analysis," *IEEE Transactions on Energy Conversion,* vol. 27, pp. 139-150, 2012.

[2]   M. Kazerooni, S. Hamidifar, and N. C. Kar, "Analytical Modeling and Parametric Sensitivity Analysis for the PMSM Steady-State Performance Prediction," revised and resubmitted for second stage of reviews to *the IET Electric Power Applications*, 2011.

[3]   S. Hamidifar and N. C. Kar, "A State Space Synchronous Machine Model with Multifunctional Characterization of Saturation Using Levenberg-Marquardt Optimization Algorithm," Being Revised and to be submitted in *IEEE Transactions on Energy Conversion,* 2012.

[4]   S. Hamidifar, M. Kazerooni, and N. C. Kar, "A novel method to represent the saturation characteristics of PMSM using Levenberg-Marquardt algorithm," in *Vehicle Power and Propulsion Conference (VPPC), 2011 IEEE*, 2011, pp. 1-6.

[5]   S. Hamidifar and N. C. Kar, "A trigonometric technique for characterizing magnetic saturation in electrical machines," in *2010 XIX International Conference on Electrical Machines (ICEM),* 2010, pp. 1-6.

[6]   S. Hamidifar and N. C. Kar, "Energy based graphical user interface modeling for PHEV energy management system," in *Proc. 2009 IEEE Electrical Power & Energy Conf. (EPEC),* 2009, pp. 1-6.